AN INVESTIGATION OF FLOW-INDUCED VIBRATIONS OF A STEAM-GENERATOR TUBE

by

Marc-Gabriel Yana

Thesis submitted to the Faculty of the

Virginia Polytechnic Institute and State University

in partial fulfillment of the requirements for the degree of

Master of Science

in

Engineering Mechanics

APPROVED:

Ali H. Nayfeh, Chairman

Eric R. Johnson

Dean T. Mook

January 1993

Blacksburg, Virginia

AN INVESTIGATION OF FLOW-INDUCED VIBRATIONS

OF A STEAM-GENERATOR TUBE

by

Marc-Gabriel Yana

Ali H. Nayfeh, Chairman

Engineering Mechanics

(ABSTRACT)

A typical failure in a heat exchanger is the breakdown of a tube due to impact-sliding wear. We investigate the dynamic behavior of a tube subjected to cross flow and study the stability of periodic solutions, bifurcations, and the route to chaos. The fluid-stiffness-controlled mechanism is chosen to represent the fluid forces and the impact forces are modeled by a piece-wise-linear spring. A two-point boundary-value algorithm is used to calculate periodic solutions and Floquet theory is used to study their stability. Poincaré sections and bifurcation diagrams are used to study non-periodic solutions. Furthermore, for this autonomous system, the method of harmonic balance appears to be less suited than the two-point boundary-value algorithm for calculating periodic motions. For the case of a single-mode approximation, the results show that the tube undergoes relaxation oscillations and hence no bifurcations occur for fluid velocities ranging from $1.1V_c$ to $3.0\ V_c$, where V_c is the critical fluid velocity. For the cases of two- and three-mode approximations, the results show that periodic solutions undergo bifurcations leading to chaos. Consequently, we conclude that chaos is the result of modal interactions. Observing the details of impacts, we also conclude that chaos appears when a second impact occurs on the same stopper. We also found intermittent chaos alternating with transient periodic motions. Lastly, we estimate the mean impact forces and mean impact-sliding wear work rates and compare them with previous results.

Acknowledgements

I would like to express my gratitude to my advisor, Dr. Ali H. Nayfeh, who provided me with the theoretical and practical backgrounds required to accomplish the present work and for his valuable teaching and advice. I also thank Drs. Dean T. Mook and Eric R. Johnson for accepting to be members of my commitee. I am grateful to Sally Shrader for her expert eyes in checking the corrections. I appreciate the companionship of my colleagues from the Nonlinear Mechanics Group, especially Drs. Balakumar Balachandran, Marwan Bikdash, and Frank Pai for their guidance and advice as the work was in progress. I thank VPI for providing me with a tuition waiver. I acknowledge Framatome Inc. that provided the financial support, solved the administrative issues, and gave matter to this work. I am indebted to my fiancée Arielle Levy who took the plane as often as she could and shared with me this American experience.

I dedicate this work to my father and to the memory of my mother, no words are deep enough to express my gratitude and love.

Table of Contents

1. INTRODUCTION

1.1 History and Topic

In nuclear power plants as illustrated in Figure 1, a first loop of fluid carries out the heat from the reactor and exchanges it in a steam generator to a secondary loop of water that produces the electrical power through a turbo alternator. The steam generator contains an array of several thousand tubes that are excited by the water, which flows inside and outside them, at high pressure, temperature, and speed, making the heat exchanger a very sensitive device of the plant.

It is known that two types of excitation coexist in the array of tubes. The first is random-type produced by turbulent flow due to vortex shedding and turbulent buffeting taking place, especially, on the top of the array where the flow is strongly two-phase. The second is a fluid-elastic coupling produced by variations in the pressure around the tubes. We will focus our study on the fluid-elastic coupling, which is by far the most dangerous. This mechanism leads to fluid-elastic instabilities that induce large-amplitude motions in the tubes and cause their breakdown, as has been shown by some experimental studies [1-3]. Hence, to prevent

such high-amplitude motions, stoppers of different kind (baffle plates, anti-vibration bars) are placed along the tubes. These stoppers give rise to impact-sliding wear that also damage the tubes on a long time scale. Our main goal is to investigate the behavior of a tube excited by fluid-elastic forces and constrained by stoppers.

From a theoretical point of view, the flow around the tubes needs to be solved by using the Navier-Stokes equations but, so far, such an approach have not been implemented due to the complexity of the flow. Therefore, some assumptions have been used to produce simplified models. Although the flow has axial as well as cross-flow components [4-5], Paidoussis [5] showed that the effect of the cross flow on the vibration of the tubes is more significant than that of the axial flow. Therefore, we neglect the effect of the axial flow and account for the effect of the cross flow.

In many theoretical models, the fluid is assumed to be inviscid and incompressible inspite of the fact that the real flow is far from being ideal. Actually, the viscous and compressibility effects of the flow are not responsible for the appearance of the instability but they are more involved in the limitation of the amplitude of the ensuing tube motion.

The theoretical work done on the flow induced instability uses essentially three different flow theories. The first is a quasi-static flow theory in which the fluid forces acting on a tube depend only on its instantaneous position. The second is also a quasi-steady flow theory but the fluid forces acting on a tube depend on its actual velocity as well as its instantaneous position. The third is an unsteady flow theory in which the fluid forces acting on a tube depend on its instantaneous position, velocity, and acceleration. According to the third theory, the most general model of the fluid forces (f_i, g_i) applied on any tube i, in a Cartesian frame, can be formulated as follows:

$$f_i = \sum_{j=1}^{N} (\alpha''_{ij}\ddot{x}_j + \alpha'_{ij}\dot{x}_j + \alpha_{ij}x_j) + (\beta''_{ij}\ddot{y}_j + \beta'_{ij}\dot{y}_j + \beta_{ij}y_j)$$
$$g_i = \sum_{j=1}^{N} (\gamma''_{ij}\ddot{x}_j + \gamma'_{ij}\dot{x}_j + \gamma_{ij}x_j) + (\delta''_{ij}\ddot{y}_j + \delta'_{ij}\dot{y}_j + \delta_{ij}y_j) \tag{1.1}$$

where the x_j and y_j are the tube displacements in the x and y directions, respectively, N is the number of tubes, the α'', β'', γ'', and δ'' are the mass-added coefficients, the α', β', γ', and δ' are the fluid-damping coefficients, and the α, β, γ, and δ are the fluid-stiffness coefficients. In real flows, the fluid coefficients depend on the displacements, velocities, and accelerations of the tubes; in other words, the fluid forces are nonlinear.

Using the standard quasi-steady theory and following the approach introduced by Paidoussis [6, 7], Price and Valerio [8] kept the higher-order terms in the Taylor series expansion of the relative flow velocity seen by a tube. Hence, they obtained a nonlinear fluid-force model. They solved the resulting equations by using the so-called Krylov and Bogoliubov technique [9]. It appears from their results that the effect of the nonlinear fluid forces becomes significant when the reduced mass parameter $\frac{m}{\rho D^2}$ exceeds approximately 30, where ρ is the fluid density, m is the mass per unit length of the tube, and D is the diameter of the tube. They also found that, even for large values of the reduced mass parameter, the nonlinear effects are negligible if the dimensionless vibration amplitude is below approximately 0.01. Hence, because in the problem considered, the motion is constrained by stoppers (baffle plates, anti-vibration-bars), the displacements are small and hence the fluid forces can be linearized. Consequently, the only nonlinear terms considered in our study are due to impact forces.

Different investigators [10-22] performed experiments on flow-induced vibrations of tubes. For different characteristics of the tube array, such as the transversal or longitudinal pitch ratios, they estimated the fluid-stiffness, fluid-damping, and mass-added coefficients using either a quasi-steady or an unsteady flow theory. Chen [23] discussed and classified the different

experiments used to estimate these coefficients. He also summarized the available models and compared them with the general theory of unsteady flow.

Two coexisting mechanisms have been shown to be responsible for the instability and have been quite extensively discussed by Paidoussis et al. [24, 25] and Weaver et al. [26-28]. The first is called fluid negative-damping controlled mechanism. In this mechanism, the fluid forces produce a negative damping, and hence the instability can develop in a single-degree-of-freedom system. From a physical point of view, the tubes can be considered to be fixed except one. The second is called fluid-stiffness controlled mechanism. It is similar to the wake flutter mechanism. The fluid forces acting on one tube are due to its displacement as well as the displacements of its neighboring tubes. Hence, this instability requires at least two degrees of freedom.

To investigate these mechanisms, two main types of experiments have been conducted in liquid, two-phase, or gas flows. In the first type, the mechanism of instability due to negative damping is studied. Hence, only one flexible tube is considered in an array of fixed tubes. The second investigates both mechanisms of instability; that is, the stiffness-controlled as well as the fluid-negative-damping mechanism. Thus, an array of flexible cylinders surrounded or not surrounded by an array of fixed tubes is considered.

Weaver et al. [26, 27] showed that, in both types of experiments conducted in air as well as in water, the critical flow velocity at which a tube becomes unstable is approximately the same, implying that the stiffness-controlled mechanism is not involved in the development of the instability. Using this observation, he developed a model based on quasi-steady theory, considering a single flexible tube surrounded by fixed tubes. The motion of the flexible tube is assumed to be harmonic and essentially normal to the streamlines. He derived the fluid forces acting on the tube from the fluctuation of the resultant of the pressure acting normal to the flow. This fluctuation is due to the tube harmonic motion, which produces a transient

behavior in the dividing streamlines of the flow channel; that is, the flow redistribution resulting from fluid inertia.

Connors [1] developed a model in which the instability is controlled by a fluid-stiffness mechanism. Using experimental observations of a flexible single row of tubes and assuming the tube motion to be periodic, he approximated the instability boundary by

$$\frac{V_c}{fD} = K\left(\frac{m\delta}{\rho D^2}\right)^{1/2}$$

where V_c is the critical velocity above which the tube motion becomes unstable, f is the frequency of the tube, D is the tube diameter, $\frac{m\delta}{\rho D^2}$ is the mass-damping parameter, and δ the cylinder logarithmic decrement.

Later, Chen [23] indicated that the coefficient K depends on the geometric characteristics of the array of tubes and that the exponent of the mass-damping parameter depends on the characteristics of the fluid. As a matter of fact, in their set of experiments, Weaver and El-Kashlan [29] obtained an exponent of 0.21 for a varying damping parameter and an exponent of 0.29 for a varying mass parameter. Furthermore, the constant K is 9.9 according to the Connors experiments. However, K depends on the pattern of the array. Soper [30] showed that, for different pitch ratios, the results do not correlate with the Connors coefficient. Also, Pettigrew [31] suggested from his set of experiments a value of 3.3 for K.

Later, the relation between the nondimensional critical velocity $\frac{V_c}{fD}$ and the mass-damping parameter has been generalized. Both the negative-damping and stiffness-controlled mechanisms have been investigated. Hence, a more complete and accurate picture of the instability boundary has been obtained. Paidoussis et al. [24] used a semi-empirical fluid-force model for a double row of flexible cylinders based on quasi-static theory. They determined the forces acting on a cylinder located downstream of two adjacent cylinders. They accounted for the rotation induced in the wake centerlines and the resultant flow velocity of the upstream cylinders on the downstream tube. Moreover, they accounted for the time lag

due to the time it takes the wake flow to cross the gap between the upstream and downstream cylinders. Furthermore, they added a retardation effect due to the slow down of the flow near the leading edge of a cylinder. Then, they used experimental results to estimate the linearized fluid-force coefficients and hence obtained a semi-empirical linearized model for the forces acting on the downstream cylinder. We note that no assumption on the viscosity or compressibility is required because the model uses experimental results to estimate the fluid-force coefficients.

Paidoussis et al. [24] repeated the procedure for an upstream cylinder, the basic difference being that the infinite flow is the gap flow velocity for the former derivation and the actual upstream flow for the later derivation with the gap flow depending on the pattern of the array. Using this model, they investigated the instability boundary of a double row of flexible circular cylinders. Then, they inserted this double row between two fixed rows of downstream tubes and one fixed row of upstream tubes. Their results quantify the boundary between the two mechanisms leading to instability. For values of $\frac{m\delta}{\rho D^2}$ below approximately 300, the instability is due to the negative-damping mechanism, whereas for values of $\frac{m\delta}{\rho D^2}$ above 300, the instability is due to the fluid-stiffness mechanism. Therefore, for high fluid velocities as well as large mass-damping parameters, the exponent is close to the Connors exponent of 0.5 (his set of experiments was conducted in air), whereas for low fluid velocities and small mass-damping parameters, the exponent is close to 1.0.

For mass-damping parameters $\frac{m\delta}{\rho D^2}$ below approximately 15, several authors [25-28] found, using different models, that the instability regions alternate with stable regions. Furthermore, the coefficient for each unstable boundary is 0, meaning that the mass-damping parameter has no influence on the critical velocity. Yet, Paidoussis and Weaver showed that the damping parameter affects the instability region in that the stable region decreases as the damping parameter is increased. These results have not been born by the experiments; the reason being that, once the tube becomes unstable, a large-amplitude motion ensues and the fluid forces can no longer be considered linear. Based on motion amplitudes at the instability

threshold, Weaver [28] experimentally corroborated the theoretical results of Price et al. [8] that the ratio of the motion amplitude to the tube diameter should be less than approximately 0.01 for the fluid forces to be linearized.

So far, we tried to sum up the numerous investigations of the fluid elastic instability, highlighting the main experimental and theoretical results obtained with different models. In most of the work, attention has been given to the phenomena and mechanisms involved in the appearance of the instability, but a few studies [32, 33, 34] have dealt with the post-instability fluid-force models and behavior. In fact it is well known that, in power plants, the steam-generator tubes undergo post-instability motions according to failures reported by safety commissions. Therefore, the fluid-elastic instability phenomenon is taken into account in the design of steam generators by adding stoppers. Consequently, in the present work, we are interested in the dynamic behavior of tubes in post-instability regimes; that is, the flow velocity is higher than the critical velocity. Because of the stoppers, the displacements will be small and hence the fluid forces will be assumed to be linear.

At the steam-generator operating conditions, the flow velocity is much higher than the critical velocity and a great majority of the tubes are subjected to small but non-negligible motions. Consequently, the approach that considers one flexible tube in the midst of fixed tubes is no longer valid. Furthermore, considering the high flow velocity and the fact that neighboring tubes are moving, one can reasonably assume that the instability is mainly due to the fluid-stiffness mechanism.

1.2 Scope

Using the Connors-Blevins stiffness-controlled model with a three-linear impacting force model, Axisa et al. [32] showed theoretically that three types of motion (periodic, quasi-periodic, and chaotic) are likely to occur. The impact stiffness κ is approximated by the formula [35]

$$\kappa = 1.9 \frac{Ee^2}{D} \sqrt{\frac{e}{D}}$$

where E is the elastic modulus, e is the thickness, and D is the diameter of the tube. Later, Paidoussis et al. [33] confirmed these results with a negative-damping model involving a delay between the tube motion and the forces induced by the wake. Three linear springs as well as cubic springs were used for the impact model, the latter allowed the authors to use a Lyapunov exponent technique to show that chaos occurs for some range of fluid velocity.

In our study, the motion of the tubes is investigated using a fluid-stiffness-controlled mechanism instead of the negative-damping-controlled mechanism. This choice is reasonable because we are interested in the case of high fluid velocity where the fluid-stiffness-controlled mechanism is likely to be more preponderant. Also, the structure investigated is a pinned-pinned straight tube with only one stopper, whereas the actual tubes in a steam generator are bent and have at least four nonlinear supports on its bent part. The simple structure is chosen to simplify the analysis and to reduce the computational effort. In addition, the nonlinear impact forces are modeled by a three-linear-spring model which is more realistic than the cubic model although it involves computational difficulties as we will discuss later. The dynamics of the tube is computed through two methods: a direct forward integration of the equations and a two-point boundary-value algorithm. We use Floquet theory to investigate the stability of the obtained periodic solutions. Since we use three linear

springs in the impact model, the derivatives of the impact forces are discontinuous and we cannot apply a Lyapunov technique to show the existence of chaotic motions. Instead, for non-periodic motions we use Poincaré sections as well as bifurcation diagrams to investigate the qualitative changes in behavior.

1.3 Contribution

Our main objective is not to provide a code for computing the motion of a tube in an array, which already exists and is extensively used to design steam generators in nuclear power plants, but to present methods for studying the nature of the motion and its instability and to provide an understanding of the change in the dynamic behavior leading to chaos.

We note that our model is simpler than that used in the design of power plant steam generators, although it preserves the essentials of the dynamics. Furthermore, we introduce friction forces using the Coulomb model. We investigate bifurcations in the motion of a tube subjected to a fluid-stiffness-controlled mechanism, as described by Connors and Blevins. To this end, we develop different methods to compute stable as well as unstable periodic motions. Hadj-Sadok and De Langre [34] investigated this model and found that chaotic motions are likely to occur for high enough fluid velocities. Here, beside confirming these results, we seek an understanding of this chaotic motion. From a study of the behavior of an isolated mode of the tube (i.e., the tube is modeled as a concentrated mass system under the same fluid-elastic model), we show that periodic motions do not undergo any bifurcations for fluid velocities V ranging from 1.1 V_c to 3.0 V_c. To understand these results, we compare our system to a Rayleigh oscillator.

Next, we consider two and three participating modes and find that periodic solutions undergo bifurcations. Consequently, we conclude that the bifurcations are the result of interactions and exchanges of energy between low-frequency and high-frequency modes due to nonlinear terms.

2. MATHEMATICAL MODEL AND MECHANICAL STRUCTURE

2.1 Mathematical Model

According to the Connors-Blevins quasi-static model [1,2], if we consider two neighboring tubes subjected to a cross flow in the x direction, then the hydrodynamic force acting on each of these tubes is proportional and orthogonal to the displacement of the other tube; that is,

$$F_{x1} = C_{f2}\rho V^2 y_2$$
$$F_{x2} = -C_{f2}\rho V^2 y_1$$
$$F_{y1} = C_{f1}\rho V^2 x_2$$
$$F_{y2} = -C_{f1}\rho V^2 x_1$$

where the subscripts 1 and 2 stand, respectively, for tubes 1 and 2; the F_{xi} and F_{yi} are the fluid forces acting on the ith tube in the x and y directions, respectively; the C_{fi} fluid-force coefficients depend on the geometry of the tubes as well as the pattern of the array; ρ is the fluid density; V is the fluid velocity; and the x_i and y_i are the displacements of the ith tube in the

x and y directions, respectively. Hence, the equations of motion of a free pair of vibrating tubes can be described by the following linear system:

$$
\begin{aligned}
m_1 \frac{\partial^2 x_1}{\partial t^2} + c_1 \frac{\partial x_1}{\partial t} + E_1 I_1 \frac{\partial^4 x_1}{\partial s^4} &= C_{f2} \rho V^2 y_2 \\
m_2 \frac{\partial^2 x_2}{\partial t^2} + c_2 \frac{\partial x_2}{\partial t} + E_2 I_2 \frac{\partial^4 x_2}{\partial s^4} &= - C_{f1} \rho V^2 y_1 \\
m_1 \frac{\partial^2 y_1}{\partial t^2} + c_1 \frac{\partial y_1}{\partial t} + E_1 I_1 \frac{\partial^4 y_1}{\partial s^4} &= C_{f1} \rho V^2 x_2 \\
m_2 \frac{\partial^2 y_2}{\partial t^2} + c_2 \frac{\partial y_2}{\partial t} + E_2 I_2 \frac{\partial^4 y_2}{\partial s^4} &= - C_{f2} \rho V^2 x_1
\end{aligned}
\tag{2.1}
$$

where m_i is the mass per unit length of tube i, c_i is the damping coefficient of the tube i, s is the tube curvilinear abscissa, and EI is the tube flexural rigidity.

Assuming that the tubes are identical and that the flow is not uniform, we reduce equations (2.1) to the following set of modal linear equations:

$$
\begin{aligned}
\ddot{x}_n + 2\xi_n \omega_n \dot{x}_n + \omega_n^2 x_n &= \frac{C_f \overline{\rho} \overline{V}^2}{m_n} \sum_{m=1}^{\infty} y_m \int_0^L r(s) u^2(s) \phi_n(s) \phi_m(s)\, ds \\
\ddot{y}_n + 2\xi_n \omega_n \dot{y}_n + \omega_n^2 y_n &= - \frac{C_f \overline{\rho} \overline{V}^2}{m_n} \sum_{m=1}^{\infty} x_m \int_0^L r(s) u^2(s) \phi_n(s) \phi_m(s)\, ds
\end{aligned}
\tag{2.2}
$$

where x_n and y_n are the modal displacements in the x and y directions, respectively; ξ_n is the modal damping ratio; ω_n is the modal radian frequency; m_n is the modal mass; ϕ_n is the mode shape; and L is the tube length. The functions r(s) and u(s) are related to the fluid density ρ and velocity V as follows:

$$\rho = r(s)\overline{\rho}$$

$$V(s) = u(s)\overline{V}$$

where $\overline{\rho}$ and $\overline{V}$ are the mean fluid density and velocity, respectively.

Next, we introduce three linear springs to represent the impact force F as

$$F = -\kappa f(x_g)$$

where x_g is the displacement of the tube in the x direction at the position of the gap,

$$f(x) = x - \frac{1}{2}(|x+g| - |x-g|)$$

and g is the gap width between the tube and the stopper. Adding this impact force to equations (2.2), we obtain

$$\begin{aligned} \ddot{x}_n + 2\xi_n\omega_n\dot{x}_n + \omega_n^2 x &= \sum_{m=1}^{\infty} \alpha_{nm} y_m + \frac{F_n}{m_n} \\ \ddot{y}_n + 2\xi_n\omega_n\dot{y}_n + \omega_n^2 y &= -\sum_{m=1}^{\infty} \alpha_{nm} x_m + \frac{\dot{y}}{|\dot{y}|}\mu\frac{F_n}{m_n} \end{aligned} \tag{2.3}$$

where μ is the friction coefficient, F_n is the impact force projected on mode n, and

$$\alpha_{nm} = \frac{C_f\bar{\rho}\bar{V}^2}{m_n}\int_0^L r(s)u^2(s)\phi_n(s)\phi_m(s)\,ds \tag{2.4}$$

We note from equations (2.3) and (2.4) that sticking was not used to simplify the model.

As it has been shown by De Langre et al. [34], the cross terms α_{nm} ($n \neq m$) are negligible compared to the diagonal terms α_{nn}, and hence the cross terms can be dropped from equation (2.3). The result is

$$\begin{aligned} \ddot{x}_n + 2\xi_n\omega_n\dot{x}_n + \omega_n^2 x_n &= \alpha_{nn} y_n - \Omega_n^2 f(x_g)\phi_n(s_g) \\ \ddot{y}_n + 2\xi_n\omega_n\dot{y}_n + \omega_n^2 y_n &= -\alpha_{nn} x_n - \frac{\dot{y}}{|\dot{y}|}\mu\Omega_n^2 f(x_g)\phi_n(s_g) \end{aligned} \tag{2.5}$$

where $\Omega_n^2 = \frac{\kappa}{m_n}$ and s_g is the curvilinear abscissa of the gap.

As already mentioned, the coefficient C_f depends on the geometry of the tube and the pattern of the array. Although we keep the analysis general, we chose $C_f = 1$, which is the order of the stiffness-fluid-force coefficients found in the experiments [17]. Furthermore, since the profiles of the fluid velocity and density are not responsible for the appearance of bifurcations,

we consider a uniform flow. This choice does not affect the qualitative aspects of the dynamic behavior. Hence, α_{nn} becomes

$$\alpha_{nn} = \frac{\rho V^2 L_n}{m_n}$$

where

$$L_n = \int_0^L \phi_n^2 \, ds$$

Consequently, the model of the dynamics of the two tubes becomes

$$\begin{aligned} \ddot{x}_n + 2\xi_n \omega_n \dot{x}_n + \omega_n^2 x_n &= \beta^2 \frac{\rho V_c^2 L_n}{m_n} y_n - \Omega_n f(x_g) \phi_n(s_g) \\ \ddot{y}_n + 2\xi_n \omega_n \dot{y}_n + \omega_n^2 y_n &= -\beta^2 \frac{\rho V_c^2 L_n}{m_n} x_n - \frac{\dot{y}}{|\dot{y}|} \mu \Omega_n f(x_g) \phi_n(s_g) \end{aligned} \tag{2.6}$$

where $\beta = \frac{V}{V_c}$ is called the instability ratio, which we will use as the control parameter. In addition, we divide (2.6) by g and we set $\bar{x}_n = \frac{x_n}{g}$ and $\bar{y}_n = \frac{y_n}{g}$

Dropping the bar in the notation, we obtain the same set of equations as (2.6) but with dimensionless gap and dimensionless displacements. Hence, $f(x)$ becomes

$$f(x) = x - \frac{1}{2}(|x+1| - |x-1|)$$

We also need a criterion to select the number of modes taken in the Galérkin expansion. This is done by neglecting the effects of the modes whose stiffnesses are higher than the stiffnesses of the stoppers.

According to De Langre et al. [34], the neglected stiffness is

$$\frac{1}{K_n} = \frac{1}{K_s} - \sum_{i=1}^{N} \frac{\phi_i^2(s_g)}{K_i}$$

where K_s is the static stiffness and N is the number of modes taken in the expansion. Hence, N is chosen such that

$$\frac{1}{K_n} < \frac{1}{K_c}$$

2.2 First Hopf Bifurcation

It is well known that because of damping, the rest position is the only stable equilibrium of the tubes for values of the fluid velocity below a critical velocity V_c. Then according to [32, 33], at V_c, both instability mechanisms (i.e., the negative-damping-controlled and fluid-stiffness-controlled mechanisms) give rise to a first Hopf bifurcation. At this bifurcation point, the motion of the tubes is a neutrally stable periodic motion. The energy dissipated by damping balances the energy gained from the fluid by the instability mechanism. The critical velocity can be obtained from the linearized equations of motion (the impact nonlinearities are not involved). For the stiffness-controlled mechanism, looking for a solution of the linearized equations (2.6) in the form

$$x_n = x_{0n} \exp(i\omega t)$$
$$y_n = y_{0n} \exp(i\omega t)$$

we obtain the characteristic equation

$$(\omega_n^2 - \omega^2 + 2i\xi_n\omega_n\omega)^2 + \left(\frac{\bar{\rho}V^2L_n}{m_n}\right)^2 = 0 \tag{2.7}$$

which, upon rearranging, yields

$$\omega_n^2 - \omega^2 + 2i\xi_n\omega_n\omega \pm iK = 0 \tag{2.8}$$

where

$$K = \frac{\bar{\rho}V^2L_n}{m_n}$$

Finally, to the first approximation in ξ_n the solution of (2.8) is

$$\omega = \omega_n + i\omega_n(\xi_n \pm \frac{K}{2\omega_n^2}) \tag{2.9}$$

Hence, the tubes are unstable when the imaginary part of (2.9) is negative. The limit is then given by $K = 2\xi_n\omega_n^2$, which yields the critical velocity V_c as

$$V_c = \left(\frac{2\xi_n\omega_n^2 m_n}{\bar{\rho} L_n} \right)^{\frac{1}{2}} \tag{2.10}$$

2.3 Mechanical Structure and Flow Characteristics

The structure considered consists of two simply-supported straight tubes whose characteristics are taken from [32] and repeated here:

length $L = 2.259m$

mass per unit of length $m = 0.8853kgm^{-1}$

external diameter $D = 22.2210^{-3}m$

thickness $= 1.2710^{-3}m$

cross-section area $S = 8.35910^{-5}m^2$

elastic modulus $E = 2.0310^{11}Nm^{-2}$

moment of inertia $I = 4.60310^{-9}m^4$

modal damping $\xi = 1$

The modal frequencies are given here:

1st mode: $f_1 = 10Hz$

2nd mode: $f_2 = 40Hz$

3rd mode: $f_3 = 90Hz$

4th mode: $f_4 = 160Hz$

5th mode: $f_5 = 250Hz$

6th mode: $f_6 = 360Hz$

The mode shapes are described by the modal functions

$$\phi_n(s) = \sin(n\pi s/L).$$

The gap is located at midspan and the mass of the tube is the sum of the actual mass and the added mass due to the flow at the steam-generator working condition.

The cross flow is assumed to have uniform velocity and density profiles along the tubes. As already mentioned, we assume the fluid to be inviscid and incompressible. The mean value of the density is $\overline{\rho} = 170\,kg/m^3$ and the control parameter is the instability ratio $\beta = \frac{V}{V_{c1}}$, where V_{c1} is the critical velocity of the first mode.

3. METHODS OF ANALYSIS

3.1 Two-Point Boundary-Value Algorithm

The two-point boundary-value algorithm (shooting method) [36] is used to find periodic solutions and to test their stabilities. Its main advantages are: the transient motion characterizing a direct integration is discarded and a stability criterion of the solutions is provided based on Floquet theory [37].

The system (2.6) can be rewritten in the first-order differential form as

$$
\begin{aligned}
\dot{u}_{1n} &= \beta \frac{\rho V_{c1}^2 L_n}{m_n} u_{4n} - 2\xi_n \omega_n u_{1n} - \omega_n^2 u_{2n} - \Omega_n f(x_g) \\
\dot{u}_{2n} &= u_{1n} \\
\dot{u}_{3n} &= -\beta \frac{\rho V_{c1}^2 L_n}{m_n} u_{2n} - 2\xi_n \omega_n u_{3n} - \omega_n^2 u_{4n} - \frac{\dot{y}}{|\dot{y}|} \mu \Omega_n f(x_g) \\
\dot{u}_{4n} &= u_{3n}
\end{aligned}
\tag{3.1}
$$

where $u_n = [u_{1n}\ u_{2n}\ u_{3n}\ u_{4n}]^T$ is the state vector, that is, $u_n = [\dot{x}_n\ x_n\ \dot{y}_n\ y_n]^T$; and the superscript T refers to the transposed matrix operator. Hence, we have four independent variables for each mode.

Equations (3.1) can be rewritten in vector form as

$$\dot{u} = G(u) \tag{3.2}$$

where u = $[\, u_1^T,\ u_2^T,\ \ldots,\ u_{4N}^T \,]$.

We look for periodic solutions of the autonomous equation (3.2). Hence, we need to determine the period T and the initial state vector η such that they satisfy the two-point-boundary-value problem

$$u(\eta, T) = u(\eta, 0) = \eta \tag{3.3}$$

For an estimated initial condition $\eta = \eta_0$ and an estimated period $T = T_0$, equation (3.3) is not satisfied in general. Hence, we add corrections $\delta\eta$ and δT and obtain $\eta = \eta_0 + \delta\eta$ and $T = T_0 + \delta T$. Substituting these new variables into equations (3.3) yields

$$\begin{aligned} u(\eta_0 + \delta\eta, T_0 + \delta T) &= u(\eta_0, T_0) + \delta\eta \\ &= \eta_0 + \delta\eta \end{aligned} \tag{3.4}$$

Expanding the left-hand side of (3.4) in a Taylor series for small $\delta\eta$ and δT , we obtain

$$[\nabla u(\eta_0, T_0) - I]\delta\eta + \frac{\partial u}{\partial T}(\eta_0, T_0)\delta T = \eta_0 - u(\eta_0, T_0), \tag{3.5}$$

where $\nabla u = \dfrac{\partial u_i}{\partial \eta_j}$ is a $4N \times 4N$ matrix.

It follows from (3.2) that

$$\frac{\partial u}{\partial T}(\eta_0, T_0) = \dot{x}(\eta_0, T_0) = G(\eta_0, T_0)$$

Furthermore,

$$\nabla \dot{u} = \nabla G(u)$$

Inverting the order of differentiation, we obtain

$$\frac{d}{dt}(\nabla u) = \nabla G(u), \tag{3.6}$$

so that the monodromy matrix $\nabla u(T_0)$ is computed by integrating equation (3.6) from t=0 to $t = T_0$, starting from the initial condition $\nabla u(0) = \underline{I}$ where $\underline{I}$ is the identity matrix.

Upon examining equation (3.5), we have $4N$ equations for $4N+1$ unknowns. Hence, we need another equation to close the system. This new equation is obtained by making the correction vector $\delta\eta$ orthogonal to the time derivative of u evaluated at $t = T_0$; that is,

$$\delta\eta^T \,.\, G(u(\eta_0, T_0)) = 0$$

Next, we deduce the stability of the solutions using Floquet theory as follows:

1. if the eigenvalues of the monodromy matrix (also called Floquet multipliers) are inside the unit circle, the periodic solution is stable (one of the eigenvalues is always unity);

2. if a real eigenvalue leaves the unit circle through $+1$, the solution loses its stability through a saddle-node or pitchfork bifurcation;

3. if a real eigenvalue leaves the unit circle through -1, the solution loses its stability through a bifurcation called period-doubling bifurcation;

4. if a pair of conjugate eigenvalues leaves the unit circle away from the real axis, the solution loses its stability through a bifurcation called Hopf bifurcation.

Moreover, in general, after a period-doubling bifurcation, the system response bifurcates into a higher-periodic stable motion, and a Hopf bifurcation produces a quasi-periodic motion.

However, we must point out some difficulties that arise when we applied the shooting method to our system. As mentioned earlier, the nonlinear impact forces are modeled by three linear springs. As a result, the impact-force derivatives are discontinuous. Consequently, the right-hand side of (3.6) is discontinuous and we were unable to calculate ∇u from (3.6). Therefore, we had to resort to a finite-difference approximation to calculate ∇u. To accomplish this, we perturbed one component of the state vector at a time. Each column i of the monodromy matrix is computed as

$$\frac{\partial u}{\partial \eta_0}(\eta_0, T_0) = \frac{u(\eta_0 + \varepsilon_i e_i, T_0) - u(\eta_0, T_0)}{(1 + \varepsilon_i)\eta_0(i)},$$

where ε_i is the perturbation value applied to the element i of the initial condition vector and e_i is a vector whose elements are all zero except the ith element, which is one; that is,

$$\begin{aligned} e_i(j) &= 0, \quad for\ j \neq i \\ &= 1, \quad for\ j = i \end{aligned}$$

Using this scheme, we were able to find periodic solutions for our system and to predict their stabilities.

Beyond the bifurcation points, this scheme encounters numerical instabilities due to the finite-difference approximation of the monodromy matrix coefficients. Indeed, if the perturbation ε_i is too large, the perturbed solution diverges significantly from the periodic orbit because the solution is unstable. Consequently, the finite-difference approximation is not accurate enough. On the other hand, if ε_i is too small, the effect of the perturbation is lost in the round-off error of the integration algorithm. Hence, the perturbation has to be greater than the error tolerance, but not too large, to provide an accurate approximation of the monodromy matrix.

Another numerical instability arises from the fact that the period of integration T changes at each iteration. To avoid this drawback, we used a dimensionless time variable defined as

$$t = \tau T \tag{3.7}$$

Then,

$$\begin{aligned} \frac{d}{dt} &= \frac{d}{d\tau}\frac{d\tau}{dt} \\ &= \frac{1}{T}\frac{d}{d\tau} \end{aligned} \tag{3.8}$$

Thus, (3.2) becomes

$$\frac{du}{d\tau} = TG(u), \tag{3.9}$$

and (3.5) becomes

$$[\nabla u(\eta_0, 1) - I]\delta\eta + \frac{\partial u}{\partial T}(\eta_0, 1)\delta T = \eta_0 - u(\eta_0, 1) \tag{3.10}$$

In addition, it follows from (3.2) that

$$u(t) = u_0 + \int_0^T G(u(t))\, dt \tag{3.11}$$

Using (3.7), (3.8), and (3.9), we rewrite equation (3.11) as

$$u(\tau) = u_0 + \int_0^1 G(u(\tau, T))\, d\tau,$$

so that

$$\frac{\partial u}{\partial T}(\eta_0, T) = G(\eta_0, T) = G(\eta_0, 1) \tag{3.12}$$

3.2 The Method of Harmonic Balance

The method of harmonic balance is presented in [37] and used to find periodic solutions for a Jeffcott rotor [38]. Although we have not been able to implement this method on our system successfully, we will present some of the difficulties that we faced in applying this method.

We want to solve equations (2.6) in the frequency domain. The presentation is done for a single mode to simplify the analysis, but the method has been generalized in reference [39]. We expand the x and y displacements in Fourier series as

$$x = a_{x0} + \sum_{n=0}^{N}\left[a_{xn}\cos(\frac{2\pi n}{T}t) - b_{xn}\sin(\frac{2\pi n}{T}t)\right]$$

$$y = a_{y0} + \sum_{n=0}^{N}\left[a_{yn}\cos(\frac{2\pi n}{T}t) - b_{yn}\sin(\frac{2\pi n}{T}t)\right]$$

where T is the motion period; the a_{xn} and b_{xn} are the coefficients of the Fourier-series expansion of the x displacement; similarly, the a_{yn} and b_{yn} are the coefficients of the Fourier-series expansion of the y displacement; and N is the number of harmonics taken in the expansions. Furthermore, because the impact forces are implicit functions of the Fourier-series coefficients, we also expand the impact forces in a Fourier series as

$$F = c_{x0} + \sum_{0}^{N}\left[c_n\cos(\frac{2\pi n}{T}t) - d_n\sin(\frac{2\pi n}{T}t)\right],$$

where the c_n and d_n are the coefficients of the Fourier-series expansion of the impact forces. Substituting these expansions into equations (2.6) and equating coefficients of the same harmonic on both sides, we obtain for the jth mode

$$H(1) = \omega_0 a_{x0} + \alpha_1 c_0 - k a_{y0} = 0$$
$$H(2) = \omega_0 a_{y0} + \alpha_2 c_0 + k a_{x0} = 0$$

$$\begin{aligned}
H(4n-1) &= -\left(\frac{2\pi n}{T}\right)^2 a_{xn} - 2\xi\omega_0\left(\frac{2\pi n}{T}\right)b_{xn} + \omega_0^2 a_{xn} + \alpha_1 c_n - k a_{yn} = 0\\
H(4n) &= \left(\frac{2\pi n}{T}\right)^2 b_{xn} + 2\xi\omega_0\left(\frac{2\pi n}{T}\right)a_{xn} - \omega_0^2 b_{xn} - \alpha_1 d_n + k b_{yn} = 0\\
H(4n+1) &= -\left(\frac{2\pi n}{T}\right)^2 a_{yn} - 2\xi\omega_0\left(\frac{2\pi n}{T}\right)b_{yn} + \omega_0^2 a_{yn} + \alpha_2 c_n + k a_{xn} = 0\\
H(4n+2) &= \left(\frac{2\pi n}{T}\right)^2 b_{yn} + 2\xi\omega_0\left(\frac{2\pi n}{T}\right)a_{yn} - \omega_0^2 b_{yn} - \alpha_2 d_n - k b_{xn} = 0
\end{aligned} \tag{3.13}$$

where $\alpha_1 = \Omega_j^2$, $\alpha_2 = -\mu\Omega_j^2$, $\omega_0 = \omega_j$, and $k = \frac{\rho V^2 L_j}{m_j}$

For an approximate solution of the displacement vector

$$P = [\, a_{x0}, a_{y0}, a_{x1}, b_{x1}, a_{y1}, b_{y1}, \ldots, a_{xN}, b_{xN}, a_{yN}, b_{yN} \,]^T,$$

we seek to minimize the error vector H using an iterative Newton-Raphson method [40]. Because the system is autonomous, we need to solve for the displacement vector P as well as the period T. Hence, the error vector H depends on P and T; that is,

$$H = H(P, T) \tag{3.14}$$

Considering the increments ΔP and ΔT to the displacement vector and period, respectively, we are looking for

$$H(P + \Delta P, T + \Delta T) = 0 \tag{3.15}$$

Expanding (3.15) in a Taylor series to first order, we obtain

$$H(P, T) + \frac{\partial G_i}{\partial P} \Delta P_j + \frac{\partial G_i}{\partial T} \Delta T = 0 \tag{3.16}$$

Furthermore, we use an alternative frequency time method [39] to obtain the impact forces. Hence, for a displacement vector P, we use the discret Fourier transform [39] to obtain the displacement in the time domain. Then, we compute the impact forces in the time domain and take the inverse discret Fourier transform [39] to obtain the Fourier-series coefficients of the impact forces. We note that equations (3.13) represent a system of $4N + 2$ equations in $4N + 3$ unknowns. Therefore, we need to eliminate one equation. This is done by setting the ΔP_i that corresponds to the maximum absolute value of H_i equal to zero for every iteration.

However, one difficulty that remains is the computation of the derivatives $\frac{\partial H_i}{\partial P_j}$ and $\frac{\partial H_i}{\partial T}$. To compute the coefficients of the matrix $\frac{\partial H_i}{\partial P_j}$, we use the fact that H can be written as

$$H = AP + Q,$$

where

$$Q = [\, c_{x0}, c_1, d_1, -\mu c_1, -\mu d_1, \ldots, c_N, d_N, -\mu c_N, -\mu d_N]^T$$

The matrix A is the linear part extracted from system (3.13). Then, the matrix $\frac{\partial H_i}{\partial P_j}$ is computed from the matrix $\frac{\partial Q_i}{\partial P_j}$ as presented in [39]. Hence, given the period T obtained from the shooting method, we are able to compute the periodic solution. However, due to the stiffness

of the stoppers, to represent the impact forces, we need to take approximately 20 harmonics and a sampling of 500 points for one period, which results in a loss of computational efficiency. Moreover, the method does not possess a large radius of convergence. We also tried to implement the computation of the matrix $\frac{\partial H_i}{\partial T}$ using the Broyden scheme, but without success. One reason for the failure is that the Fourier-series coefficients are sensitive to changes in the period T, and hence numerical instabilities appear. Consequently, for the bifurcation analysis of the tubes, we only use the shooting method to obtain the periodic motions.

3.3 Numerical Integration

Besides being easy to implement, the direct numerical integration of equations (3.1) has the advantage of possessing a radius of convergence that is larger than that of the shooting method, which solves a linearized system. Furthermore, to converge, the shooting method requires a good approximation of the state vector and the period. This can be obtained by integrating the system for a long time. Also, when a periodic solution loses stability, a long-time numerical integration is a convenient way to get the new attractor (for instance in the case of a jump).

But two main drawbacks appear with this method. The first is that it takes a long time before the transient motion disappears, especially, when the damping ratio and the nonlinear effects are small. The second drawback is that the long-time integration method is unable to provide unstable limit cycles because it simulates the actual behavior of the motion. We will show later that the analysis of unstable limit cycles provides an understanding of the real motion.

Concerning the integration algorithm, we chose the implicit Gear algorithm from the IMSL mathematical library with a round-off error tolerance of order 10^{-6}. This implicit scheme takes

into account the system large stiffness due to the impact-force discontinuous derivatives and to the fact that the stoppers are approximately 300 times stiffer than the tubes. For an instability ratio above 2.0 and a tolerance of 10^{-6}, during the impact period the Gear algorithm needs a maximum of 10^{9} iterations to integrate over a time interval equal to 10^{-4} second. Other algorithms, such as the explicit Runge-Kutta and implicit Adams schemes, have been tested but none of them has been able to reduce the number of iterations required for a tolerance of 10^{-6} .

3.4 Poincaré Sections

A definition of Poincaré sections for non-autonomous and autonomous systems is given in Parker and Chua [41]. Poincaré sections are constructed by replacing an nth -order continuous-time system with an $(n-1)^{th}$ -order discrete-time system. This transformation preserves the limit set properties of continuous flows. For a non-autonomous system, it is usually the time variable that is reduced in the mapping. The sections are formed by taking all the points of the continuous flow every T seconds after the steady-state is reached. For instance, if the system is subjected to a forced excitation, the period T is the period of the forcing function. This map can be seen as a stroboscopic picture of the continuous flow at the first harmonic. For an autonomous system, no particular period is defined; hence the process of selection is done in the spatial variables. The map is constructed of points crossing a chosen $(n-1)^{th}$ -order hyperplane, such as $x = 0$.

We may now describe how limit sets of the continuous-time system are represented in the Poincaré map. Periodic solutions are pictured as a set of isolated points. The number of points depends on the choice of the hyperplane. We will show later that the choice of the

hyperplane is important to an understanding of the phenomena underlying the motion. Further, a quasi-periodic motion appears in the Poincaré section as a number of embedded closed curves, with the number of closed curves also depending on the choice of the $(n-1)^{th}$ -order hyperplane. Finally, all pictures that do not have one of the simple geometrical forms previously described indicate a chaotic motion. However, it should be mentioned that a particular kind of chaos exposes the so-called Cantor sets [41], which are recognizable because of their fine structures. But for our system, no Cantor set has been found, and as we will see later, the points forming the Poincaré section of chaotic motion are significantly spread.

We note that in the case of autonomous systems, a map constructed using a T-periodic time sampling can lead to a misinterpretation of the motion. For a K-orbit periodic solution, when the period T is unknown, a period-locking error can give a picture of a motion that looks like a quasi-periodic motion. Therefore, we will choose a spatial hyperplane to obtain the Poincaré sections. Furthermore, to understand the dynamics of our system, an interesting section choice is the hyperplane defined by $\dot{x}=0$. This section contains the impact states where the penetration of the tubes in the stoppers is maximum.

Finally, we must emphasize the main drawback of these mapping methods. A Poincaré section usually requires approximately 1,000 points to be trustworthy. As already mentioned, we use a time step of 10^{-4} seconds in the integration algorithm. Considering that a 1-orbit solution crosses a hyperplane once every revolution, a trustworthy Poincaré section will require around 1,000 periods. In our system, the 1-orbit solution has a period of approximately 0.1 second. Hence, an integration of 100 seconds is needed.

3.5 Bifurcation Diagrams

The system of equations (3.2) can be written as follows:

$$\dot{u} = G(u, \beta)$$

where β is the control parameter. In the present study, we are interested in qualitative changes in behavior as we increase the control parameter. The purpose of bifurcation diagrams is to provide the values of the control parameter at which these qualitative changes occur. In fact, the diagrams are constructed by projecting a Poincaré section on one of the $n^{th} - 1$ components of the hyperplane for each incremental value of the control parameter. Hence, the isolated points representing periodic motions in the Poincaré section are projected into points in the bifurcation diagrams. The embedded closed curves representing quasi-periodic motions in the Poincaré section become embedded segments in the bifurcation diagrams. Finally, chaotic motions are projected into embedded segments, but the points are more spread out than for quasi-periodic motions. We note that it is difficult from bifurcation diagrams to show the difference between quasi-periodic and chaotic motions, both of which display smears of points more or less spread out. Hence, the Poincaré sections or the shooting method, if the motion is periodic before the bifurcation occurs, is required to characterize these types of motion.

Also, to obtain an accurate bifurcation diagram, the increment in the control parameter should be small enough; otherwise, one can miss some bifurcations, such as period doublings, periodic windows [41], or a transition from a quasi-periodic to a chaotic motion. In our study we chose an increment of 10^{-2} and decreased it to 0.1×10^{-2} in the vicinity of a bifurcation. In addition, for each value of the control parameter, we integrated equations (3.1) for 200 seconds; that is, 20 periods of the first harmonic of the tubes. Hence, the drawback of bifurcation diagrams also appears to lie in the computational effort. To obtain a diagram in a range of 1 to 3 times the critical velocity requires an integration for approximately 6000

seconds. However, to accelerate the algorithm, we can use the shooting method to locate and follow the periodic branches.

4. RESULTS AND DISCUSSION

4.1 Approach Chosen

Before presenting the results, we present the approach chosen to understand the phenomena involved in the bifurcation. Initially, we focus on the dynamics of the post first Hopf bifurcation. Hence, in the bifurcation diagrams, the trivial solution and the first Hopf bifurcation do not appear. Furthermore, to describe the actual tube motion, we use a modal superposition. We are considering a continuous system under impact forces whose frequency is 17 times higher than the main frequency of the tube motion. Hence, according to the truncation criterion described in Section 2.1, we must take at least ten (five in-plane and five out-of-plane) modes in the Galérkin expansion.

If we take any isolated pair of modes (in-plane and out-of-plane), the corresponding set of equations (2.6) contains odd nonlinear terms due to impact and friction forces. We analyze the behavior of this isolated system and see if it undergoes bifurcations and chaotic motion due to the presence of nonlinear terms. Because the main frequency of the tube motion is close to the first harmonic of the tube, the isolated set of equations at first investigated will

be the first-mode coupled equations. Once the behavior of the first two modes has been identified, we investigate how four participating modes (two in-plane and two out-of-plane modes) interact with one another and with the fluid forces. Finally, we present a more complete description by taking six modes (three in-plane and three out-of-plane modes) in the expansion.

4.2 First Harmonic Behavior

In Figures 2-5, we show the effect of an increase in the ratio of instability from 1.1 to 4.5 on the two-dimensional projections of the phase portraits on the $\dot{x}$-x, $\dot{y}$-y, $\dot{x}$-y, and y-x planes. For each ratio of instability, the corresponding Floquet multipliers were found to be inside the unit circle. Hence, at least for these values of the control parameter, no bifurcation occurs and the solutions are periodic. To understand these results, we go back to the set of equations (2.6) and substitute a cubic impact model for the three-linear-spring model. Hence, equations (2.6) take the general form

$$\begin{aligned} \ddot{x} + 2\hat{\xi}\omega_0\dot{x} + \omega_0^2 x + \alpha_1 x^3 &= \hat{k}y \\ \ddot{y} + 2\hat{\xi}\omega_0\dot{y} + \omega_0^2 y + \alpha_2 x^3 &= -\hat{k}x \end{aligned} \tag{4.1}$$

where the α_i are constants and $\hat{k} = \dfrac{\rho V^2 L_1}{m_1} = \beta^2 \dfrac{\rho V_c^2 L_1}{m_1}$.

We seek a solution for the case of weak perturbations; that is for values of $\hat{k}$ just above the first Hopf bifurcation. We order the perturbation such that the effects of the fluid forces balance the effects of the impact forces. Hence, we set the control parameter $\hat{k} = \varepsilon k$, where ε is a small dimensionless parameter of the order of the nonlinear terms. Similarly, because the damping ratio is also small, we put $\hat{\xi} = \varepsilon\xi$.

Hence, we rewrite (4.1) as

$$\ddot{x} + \varepsilon 2\xi\omega_0\dot{x} + \omega_0^2 x = -\alpha_1 x^3 + \varepsilon k y$$
$$\ddot{y} + \varepsilon 2\xi\omega_0\dot{y} + \omega_0^2 y = \alpha_2 x^3 - \varepsilon k x \tag{4.2}$$

where $\alpha_2 > 0$.

Further, using the method of multiple scale [9], we seek solutions of the form

$$x = \varepsilon x_1(T_0, T_1) + \varepsilon^2 x_2(T_0, T_1) + \ldots$$
$$y = \varepsilon y_1(T_0, T_1) + \varepsilon^2 y_2(T_0, T_1) + \ldots \tag{4.3}$$

where $T_n = \varepsilon^n t$ and t is time. In terms of T_0 and T_1, the derivatives become

$$\frac{d}{dt} = D_0 + \varepsilon^2 D_1 + \ldots$$
$$\frac{d^2}{dt^2} = D_0^2 + 2\varepsilon^2 D_0 D_1 + \ldots \tag{4.4}$$

where $D_0 = \frac{\partial}{\partial T_0}$ and $D_1 = \frac{\partial}{\partial T_1}$.

We substitute equations (4.3) and (4.4) into equations (4.2) and equate coefficients of like powers of ε. The first-order problem is

$$D_0^2 x_1 + \omega_0^2 x_1 = 0$$
$$D_0^2 y_1 + \omega_0^2 y_1 = 0 \tag{4.5}$$

The general solutions of (4.5) are

$$x_1 = A_1(T_2) e^{i\omega_0 T_0} + cc$$
$$y_1 = A_2(T_2) e^{i\omega_0 T_0} + cc \tag{4.6}$$

where cc represents the complex conjugate of the preceding terms.

The third-order problem is

$$D_0^2 x_2 + \omega_0^2 x_2 = -2D_0(D_1 x_1 + \xi\omega_0 x_1) + k y_1 - \alpha_1 x_1^3$$
$$D_0^2 y_2 + \omega_0^2 y_2 = -2D_0(D_1 y_1 + \xi\omega_0 y_1) - k x_1 + \alpha_2 x_1^3 \tag{4.7}$$

Substituting the solutions of the first-order problem into (4.7), we obtain

$$
\begin{aligned}
D_0^2 x_2 + \omega_0^2 x_2 &= -2i\omega_0(A'_1 + \xi\omega_0 A_1)e^{i\omega_0 T_0} + kA_2 e^{i\omega_0 T_0} - \alpha_1(A_1^3 e^{3i\omega_0 T_0} + 3A_1^2\bar{A}_1 e^{i\omega_0 T_0}) + cc \\
D_0^2 y_2 + \omega_0^2 y_2 &= -2i\omega_0(A'_2 + \xi\omega_0 A_2)e^{i\omega_0 T_0} - kA_1 e^{i\omega_0 T_0} + \alpha_2(A_1^3 e^{3i\omega_0 T_0} + 3A_1^2\bar{A}_1 e^{i\omega_0 T_0}) + cc
\end{aligned}
\tag{4.8}
$$

where the prime stands for the derivative with respect to the slow scale T_1. The coefficients of $\exp(i\omega_0 T_0)$ will produce secular terms in x_2 and y_2. To obtain uniform expansions, we eliminate these terms and obtain

$$
\begin{aligned}
-2i\omega_0(A'_1 + \xi\omega_0 A_1) + kA_2 - 3\alpha_1\bar{A}_1 A_1^2 &= 0 \\
-2i\omega_0(A'_2 + \xi\omega_0 A_2) - kA_1 + 3\alpha_2\bar{A}_1 A_1^2 &= 0
\end{aligned}
\tag{4.9}
$$

Next, we write A_1 and A_2 in the polar form

$$
\begin{aligned}
A_1 &= \frac{1}{2} a_1 e^{i\theta_1} \\
A_2 &= \frac{1}{2} a_2 e^{i\theta_2}
\end{aligned}
\tag{4.10}
$$

where the functions θ_i and a_i depend on the slow scale T_1. Substituting these polar forms into equations (4.9) and separating real and imaginary parts, we obtain

$$
\begin{aligned}
&\omega_0 a_1 \theta'_1 + \frac{1}{2} k a_2 \cos(\gamma) - \frac{3}{8}\alpha_1 a_1^3 = 0 \\
&\omega_0 a_2 \theta'_2 - \frac{1}{2} k a_1 \cos(\gamma) + \frac{3}{8}\alpha_2 a_1^3 \cos(\gamma) = 0 \\
&-\omega_0(a'_1 + \xi\omega_0 a_1) + \frac{1}{2} k a_2 \sin(\gamma) = 0 \\
&-\omega_0(a'_2 + \xi\omega_0 a_2) + \frac{1}{2} k a_1 \sin(\gamma) - \frac{3}{8}\alpha_2 a_1^3 \sin(\gamma) = 0
\end{aligned}
\tag{4.11}
$$

where $\gamma = \theta_2 - \theta_1$. We note that, because the system is autonomous, there is no zero-phase defined, and hence we can solve the governing equations (4.11) by considering the relative phase γ instead of the actual phases θ_1 and θ_2. Consequently, equations (4.11) become

$$
\gamma' = \frac{1}{2}\frac{k}{\omega_0}\left(\frac{a_1}{a_2} + \frac{a_2}{a_1}\right)\cos(\gamma) - \frac{3}{8}\frac{a_1^2}{\omega_0}\left(\alpha_1 + \alpha_2\frac{a_1}{a_2}\cos(\gamma)\right) \tag{4.12}
$$

$$
a'_1 = \frac{1}{2}\frac{k a_2}{\omega_0}\sin(\gamma) - \xi\omega_0 a_1 \tag{4.13}
$$

$$
a'_2 = \frac{1}{2}\frac{k a_1}{\omega_0}\sin(\gamma) - \xi\omega_0 a_2 - \frac{3}{8}\frac{\alpha_2 a_1^3}{\omega_0}\sin(\gamma) \tag{4.14}
$$

Equations (4.12)-(4.14) govern the amplitudes and relative phase.

We can solve the linear part of equations (4.9) ($\alpha_1 = \alpha_2 = 0$) by assuming the following general form for the solution:

$$\begin{aligned} A_1 &= \hat{A}_1 e^{\lambda T_1} + cc \\ A_2 &= \hat{A}_2 e^{\lambda T_1} + cc \end{aligned} \tag{4.15}$$

Substituting equations (4.13) into equations (4.9), we have

$$\begin{aligned} -2i\omega_0(\lambda + \xi\omega_0)\hat{A}_1 + k\hat{A}_2 &= 0 \\ -k\hat{A}_1 - 2i\omega_0(\lambda + \xi\omega_0)\hat{A}_2 &= 0 \end{aligned} \tag{4.16}$$

For a nontrivial solution, the determinant of the coefficient matrix in (4.14) must be equal to zero. Hence, we obtain the characteristic equation

$$4\omega_0^2(\lambda + \xi\omega_0)^2 + k^2 = 0 \tag{4.17}$$

or

$$\lambda = -\xi\omega_0 \pm \frac{k}{2\omega_0}$$

Therefore, the solution of the linear problem can be expressed as

$$\begin{aligned} A_1 &= c_1 e^{(\frac{k}{2\omega_0} - \xi\omega_0)T_1} + c_2 e^{-(\frac{k}{2\omega_0} + \xi\omega_0)T_1} \\ A_2 &= i\left[c_1 e^{(\frac{k}{2\omega_0} - \xi\omega_0)T_1} - c_2 e^{-(\frac{k}{2\omega_0} + \xi\omega_0)T_1}\right] \end{aligned}$$

where c_1 and c_2 are arbitrary constants that can be determined from the initial conditions. As expected, we find the same instability criterion, as in Section 2.2. When $k > 2\xi\omega_0^2$, A_1 and A_2 grow exponentially with time and the tubes are unstable. The energy dissipated by damping is less than the energy transferred from the flow to the tubes. When $k < 2\xi\omega_0^2$, A_1 and A_2 decay exponentially with time. When $k = k_c = 2\xi\omega_0^2$, A_1 and A_2 tend to constant values and the tubes are marginally stable. The tube motion is periodic having an amplitude that depends on the initial conditions. In Figure 6, we show two such periodic motions in the y-x plane for two different initial conditions. Furthermore, x and y are 90° out of phase, as evident from the time variations of A_1 and A_2.

Periodic motions are obtained by setting $a'_1 = a'_2 = \gamma' = 0$; that is,

$$\frac{1}{2}\frac{k}{\omega_0}\left(\frac{a_1}{a_2}+\frac{a_2}{a_1}\right)\cos(\gamma)-\frac{3}{8}\frac{a_1^2}{\omega_0}\left(\alpha_1+\alpha_2\frac{a_1}{a_2}\cos(\gamma)\right)=0 \tag{4.18}$$

$$\frac{1}{2}k\frac{a_2}{\omega_0}\sin(\gamma)-\xi\omega_0 a_1=0 \tag{4.19}$$

$$\frac{1}{2}k\frac{a_1}{\omega_0}\sin(\gamma)-\xi\omega_0 a_2-\frac{3}{8}\frac{\alpha_2 a_1^3}{\omega_0}\sin(\gamma)=0 \tag{4.20}$$

Next, we investigate the effect of the cubic nonlinearities on the relative phase and amplitudes. We note that the impact of the tubes against the supports modifies both the phase and the amplitudes, a characteristic of cubic nonlinearities.

It follows from equation (4.19) that

$$a_2=\frac{1}{\beta^2\sin(\gamma)}a_1=\frac{k_c}{k\sin(\gamma)}a_1 \tag{4.21}$$

where $\beta=\frac{V}{V_c}=\sqrt{\frac{k}{2\xi\omega_0^2}}$. Substituting equation (4.21) into (4.20), we obtain

$$a_1=\sqrt{\frac{4k}{3\alpha_2}}\left[1-\left(\frac{k_c}{k}\right)^2\frac{1}{\sin^2(\gamma)}\right]^{\frac{1}{2}} \tag{4.22}$$

We note that a_1 varies inversly with the square root of the stiffness nonlinear parameter $\alpha_2=\mu\alpha_1$. For real solutions, equation (4.22) demands that

$$1-\left(\frac{k_c}{k}\right)^2\frac{1}{\sin^2(\gamma)}>0 \tag{4.23}$$

From equation (4.21), we deduce that $a_2<a_1$, which is born out by the numerical simulations. Substituting equations (4.21) and (4.22) into (4.18) yields

$$\begin{aligned}-\frac{3}{8\omega_0}\frac{4k}{3\alpha_2}\left[1-\left(\frac{k_c}{k}\right)^2\frac{1}{\sin^2(\gamma)}\right]\left(\alpha_1+\alpha_2\frac{k}{k_c}\sin(\gamma)\cos(\gamma)\right)\\+\frac{1}{2}\frac{k}{\omega_0}\left(k\frac{\sin(\gamma)}{k_c}+\frac{k_c}{k\sin(\gamma)}\right)\cos(\gamma)=0\end{aligned} \tag{4.24}$$

Rearranging (4.24) yields

$$\frac{\alpha_1}{\alpha_2}\left[\left(\frac{k_c}{k}\right)^2-1\right]\tan^2(\gamma)+2\frac{k_c}{k}\tan(\gamma)+\frac{\alpha_1}{\alpha_2}\left(\frac{k_c}{k}\right)^2=0 \tag{4.25}$$

Hence, the phase γ is defined in terms of the prescribed parameter as

$$\tan(\gamma)=\frac{\alpha_2}{\alpha_1}\left(\frac{k}{k_c}-\frac{k_c}{k}\right)^{-1}\left\{1\pm\sqrt{1-\left(\frac{\alpha_1}{\alpha_2}\right)^2\left[\left(\frac{k_c}{k}\right)^2-1\right]}\right\} \tag{4.26}$$

or, in term of $\beta=\frac{V}{V_c}$, as

$$\tan(\gamma)=\frac{\alpha_2}{\alpha_1}\left(\beta^2-\frac{1}{\beta^2}\right)^{-1}\left\{1\pm\sqrt{1-\left(\frac{\alpha_1}{\alpha_2}\right)^2\left[\left(\frac{1}{\beta}\right)^4-1\right]}\right\} \tag{4.27}$$

In Figure 7, for a value of $\beta=1.5$, we plot the analytical periodic solution obtained by the method of multiple scales (dashed line) and the periodic solution obtained by the shooting method (solid line). We note the good agreement between both solutions for this value of the control parameter.

To explain the stability of the periodic solution, we refer to relaxation oscillations of the Rayleigh equation defined by [37]

$$\frac{1}{k}\frac{dx}{dy}=-\frac{x-x^3+y}{x}$$

Hence, when k is very large, $\dot{y}$ is very small compared to $\dot{x}$, and $\frac{dx}{dy}$ is very large if $y\neq x^3-x$. When the point approaches the curve M: $y=x^3-x$, then $\dot{x}$ becomes small and the point moves slowly on the curve M. This curve is called the slow manifold and is sketched in Figure 8.

Similarly, for the system of equations (2.6), we see that when the value of β is very large, $\dot{x}_1$ and $\dot{x}_3$ are very large compared to x_2 and x_4 as long as the tubes are far away from the slow manifold. For a cubic spring, the slow manifold is described by

$$\begin{aligned}\beta u_4-2\xi\omega\dot{u}_2-\omega^2u_2-\alpha_1u_2^3=0\\ -\beta u_2-2\xi\omega\dot{u}_4-\omega^3u_4+\alpha_2u_2^3=0\end{aligned} \tag{4.28}$$

Further, the variables playing the role of y in the Rayleigh equation are coupled. As showed in Figures 2c and 4c, the relaxation acts on the phase portrait of $\dot{x}$-x and $\dot{x}$-y . The tube sticks to one of the stoppers and is ejected to the other stopper; this process keeps repeating. As the flow velocity increases, the transition between both stoppers becomes more instantaneous. We note that the slow manifold corresponds physically to the stoppers. Because the relaxation oscillators give rise to the saturation phenomenon, it is unlikely to observe any bifurcation on concentrated mass systems.

This concludes the investigation of a two-mode motion. We showed that, (a) for small flow velocities an analytical approximation is available and is in good agreement with the numerical results, (b) no bifurcation was found in the range of instability ratio investigated, and (c) the tube undergoes relaxation oscillations that prevents bifurcations and chaotic motions to occur.

4.3 Four-Mode Analysis

In this section, we consider the continuous system described in Section 2.2, with four-mode Galérkin expansions (two in-plane and two out-of-plane in the x and y directions). However, because the stoppers are at midspan, the in-plane and out-of-plane second modes do not contribute to the motion. Hence, we are actually working with only the in-plane and out-of-plane first and third modes. From the previous results, we already know that any bifurcation is the result of modal interactions.

In Figures 9-11, we show projections of the phase portraits on the $\dot{x}$-x, $\dot{y}$-y, and y-x planes for the instability ratios of 1.300, 1.600 and 1.750. We note the appearance of a loop for instability ratios above 1.600 in the projection of the phase portrait on the $\dot{x}$-x plane. This is due to an

increase in the participation of the third-mode response. Indeed, it is clear that the first in-plane and out-of-plane modes drive the global motion of the tubes. As the control parameter increases, the motion becomes more and more complicated and irregular.

To isolate the origin of the loop in the $\dot{x}$-x plane, we look at Figure 12 where we superpose the motion for one-half of a period for the three different instability ratios mentioned above. We see that an increase in the control parameter produces an inflection point after the impact. Hence, the tubes come back to the stopper they just hit. In Figures 13 and 14, we show the time history of each mode for one-half of a period. We note that the first mode remains unchanged as the control parameter increases. However, the third-mode amplitude increases and its phase is shifted downwards. This phase retardation produces the second hump, whereas the increase in the third-mode amplitude produces the growth of the second hump. Consequently, for high flow velocities, as the third mode response becomes more significant, the second hump grows until it finally reaches the stopper, and at this instant, two impacts will occur at each stopper. This mechanism accounts for the exchange of energy between the modes. The energy extracting from the flow is transferred to the third mode through the impact and friction forces. And this causes the change in its phase and amplitude, while the energy of the first mode remains unchanged despite the increase in the global energy transferred from the flow to the tubes.

In Figure 15, we plot the bifurcation diagram obtained by using the shooting method. The Poincaré section is taken to be the hyperplane defined by $\dot{x} = 0$ and $x > 0$. For $\beta < 1.589$ there is only one branch corresponding to the impact states. As β increases, we note that the stoppers penetrate deeper into the tubes. At $\beta = 1.589$, the appearance of the new branch corresponds to the inflection point described earlier. For values of $\beta > 1.589$, the new branch splits into two branches which correspond to the appearance of the loop in the $\dot{x}$-x plane. Moreover, as β increases further, the split branches diverge away from each other. This separation corresponds to the growth of the loop size in Figure 9c and to the increase in the second hump in Figure 12. Until this point, no bifurcation occurs in the system. As the

instability ratio reaches a value of 1.774, a real eigenvalue of the monodromy matrix leaves the unit circle through $+1$, indicating either a saddle-node bifurcation or a symmetry-breaking bifurcation. We note that the bifurcation occurs when the middle branch reaches $x = 1.0$, which corresponds physically to a second impact on the same stopper. Investigating the eigenvalues of the monodromy matrix calculated over one-half of a period, we find a real eigenvalue of -1. This indicates that the periodic motion lost stability through a symmetry-breaking bifurcation. This result is confirmed in Figure 13, where we note that at this point, there is a drastic change in the slopes of the branches. Hence, for $\beta > 1.774$, the one-impact stable periodic solution becomes a two-impact unstable periodic solution. The bifurcation diagram obtained by using the shooting method shows the evolution of both the stable and unstable branches. Furthermore, when the two-impact branches meet at $\beta = 2.159$, the shooting algorithm diverges, suggesting that the solution under investigation is no longer periodic.

Next, we study the actual motion of the tubes. We refer to Figure 16 where we plot the bifurcation diagram obtained by using direct integration. The two diagrams in Figures 15 and 16 are identical until the symmetry-breaking bifurcation occurs. The increment on the control parameter is 10^{-3} for $1.774 \leq \beta \leq 1.914$, otherwise it is 5^{-3}. As expected from the previous bifurcation diagram, it appears that the actual tube behavior becomes non-periodic when the middle branch reaches an amplitude of 1.0. In Figure 17, we enlarge the area near the bifurcation point. As already mentioned in Section 3.5, we need to look at Poincaré sections to analyze non-periodic motions. In Figure 18, we plot the Poincaré section defined by $\dot{x} = 0$, $x > 0$, and $\beta = 1.779$. This figure indicates the chaotic behavior of the motion of the tubes.

In Figure 19, for a the same value of $\beta = 1.779$, we plot the projection of the phase portrait on the $\dot{x}$-x plane. We note that the tube motion looks like a quasi-periodic motion. To understand the motion further, in Figure 20 we plot x-t, where t is the time at which the flow crosses the Poincaré hyperplane. We recorded the motion after 300 seconds so that the transient would have died out. This figure shows that the tube response reached a steady-state motion. The

three piece-wise discontinuous branches indicate the one-impact solution investigated earlier. The upper branch represents the impact states; we note they do not fluctuate. The lower branches represent the fluctuation of the second hump mentioned earlier, which is indicated by a dotted line in Figure 12. The gap between the two lower branches increases, indicating that the second hump amplitude is also increasing. Furthermore, the branches terminate when the middle branch reaches an amplitude of $x = 1$. At this point, the motion is chaotic for a short lapse of time. During this chaotic motion, single and double impacts are likely to occur. The one-impact motion lasts approximately 7 times longer than the chaotic motion. Hence, above the bifurcation point, an intermittent chaotic motion alternates with the transient one-impact motion.

To understand this phenomenon, we refer to Figure 21 where we plot x-t and y-t on an enlarged scale of t. We see that the amplitudes of the two lower branches are shifted downwards after the chaotic motion. This behavior may be due to the fact that the two-impact solution is unstable, as we showed earlier. During the one-impact motion, the second hump amplitude increases due to the excess of energy extracted from the flow by the third mode. Then, when the second impact occurs, some of the energy is dissipated by friction. As a result, the amplitudes of motion in the x and y directions decrease and we go back to the one-impact motion. We also note that during chaotic motions, the stoppers penetrate deeper into the tubes, which may damage them.

We can now explain the Poincaré section in Figure 18. The vertical segment represents the fluctuation of the impact point on the tangential plane; that is, the y direction. It is vertical because the motion is bounded in the x direction. The lowest segment in the Poincaré section corresponds to the middle branch in the bifurcation diagram and the third segment in the Poincaé section corresponds to the lowest branch in the bifurcation diagram. We note that the lowest segment is bounded in the x direction due to the double impact.

For the same value of β, we investigated the effect of the friction forces by putting $\mu = 0$. The solution obtained is a stable one-impact periodic motion.

For values of β above where the shooting algorithm diverges, the transient one-impact behavior described above disappears. In Figure 22, for a value of $\beta = 2.200$, we show two-dimensional projections of the Poincaré section on the $\dot{x}$-x and x-t planes, respectively. We note that the segments and the branches which represent the fluctuation of the one-impact motion disappeared.

To summarize the four-mode investigation, we analyzed the energy transfer between the in-plane and out-of-plane first and third modes due to the nonlinearity. Chaos occurs after the symmetry-breaking bifurcation. Furthermore, we showed that the solution becomes unstable when the tube hits the same stopper twice. Hence, chaos arises from the fact that the two-impact motion is unstable. For a value of $\beta = 1.779$, the tube motion is a transient one-impact motion until a second impact occurs. At this point, some energy is dissipated by friction and results in the tube going back to the one-impact motion. Here, we must emphasize that the piece-wise linear impact model plays an important role because it is acting discontinuously with time, thereby changing the mathematical model. For high instability ratios, according to the shooting algorithm, no stable or unstable periodic motions exist. Instead, the motion is chaotic but without the alternating intermittent chaotic motion and the transient one-impact periodic motion.

4.4 Six-Mode Analysis

We consider six modes in the Galérkin expansion; that is, the first, third, and fifth modes in both the x and y directions, since the stoppers are located at midspan. In Figures 23-25, we

plot $\dot{x}$-x, $\dot{y}$-y, and y-x for $\beta = 1.210$, $\beta = 1.310$, and $\beta = 1.510$, respectively. We note the presence of the loop in the $\dot{x}$-x plane, which indicates the presence of the second hump, as described in Section 4.3. At an instability ratio of 1.516, the one-cycle periodic solution loses stability. A real Floquet multiplier leaves the unit circle through -1, indicating a period-doubling bifurcation. However, not all of the Floquet multipliers of the newly born two-cycle periodic solution are inside the unit circle. Hence, the two-cycle periodic solution is unstable.

In Figure 26, we present the bifurcation diagram obtained by using direct integration. The hyperplane is defined by $\dot{x} > 0$ and $x = 0$. In Figure 27, we plot the Poincaré section for a value of $\beta = 1.526$; the hyperplane is defined by $\dot{x} = 0$ and $x > 0$. The plot indicates the chaotic nature of the motion. Further, we note that the points are less spread than those in Figure 18 obtained in the four-mode investigation. As in the previous section, it is likely that this unstable period doubling arises from the structural change in the mathematical model, when it passes from a one-impact motion to a two-impact motion. The three segments indicate the presence of an intermittent two-impact chaotic motion, alternating with a transient one-impact periodic motion.

As we increase the control parameter, the chaotic motion loses stability, resulting to a two-cycle periodic motion, as shown in Figure 26. Furthermore, investigating the two-cycle periodic motion using the shooting method, we found a critical Hopf bifurcation. Two complex conjugate eigenvalues leave the unit circle away from the real axis when the control parameter decreases to 1.657. In Figure 28, we enlarged the bifurcation diagram near $\beta = 1.516$ and $\beta = 1.657$; the hyperplane is defined by $\dot{x} > 0$ and $x = 0$. In Figure 29, we plot the Poincaré section for a value of $\beta = 1.633$. The hyperplane is defined by $\dot{x} = 0$ and $x > 0$ to reduce the number of crossing points. In the case of one-cycle periodic motions, this hyperplane is crossed once at each cycle instead of three in the case of the hyperplane used earlier because of the loop. The plot illustrates the quasi-periodic nature of the motion.

The power spectra of the x signal are shown in Figure 30 for the instability ratios 1.516 and 1.526, respectively; that is before and after the period doubling. These figures point out the relative smallness of the contribution of the fifth mode to the response compared to the contribution of the first and third modes. Although, the magnitude of the fifth in-plane mode mode appears negligible relative to those of the lower modes, its presence in the expansion changes the bifurcation. Furthermore, it produces a periodic window for values of $\beta > 1.657$. Later, we will see that the periodic window corresponds to a two-impact periodic solution.

At a value of $\beta = 1.772$, the two-cycle periodic solution loses stability again through a Hopf bifurcation. In Figure 31, we plot the Poincaré section for a value of $\beta = 1.773$. Although the closed curves here are not as well defined as in Figure 29, the plot indicates a quasi-periodic motion. To illustrate the details of the bifurcations, we show an enlarged portion of the bifurcation diagram in Figure 32. Figure 33 shows the presence of a high-cycle solution for $\beta = 1.782$.

Next, for $\beta > 1.784$, the motion of the tubes becomes chaotic. Then, a 6-cycle periodic window appears beyond $\beta = 1.813$ through a Hopf bifurcation. In Figure 34, for $\beta = 1.811$, we plot the Poincaré section, it indicates a quasi-periodic motion. According to the shooting algorithm and the enlarged bifurcation diagram in Figure 35, this 6-cycle periodic solution loses stability through a period-doubling bifurcation. The period doubling gives rise to a 12-cycle stable periodic solution, as confirmed by the Poincaré section shown in Figure 36 for $\beta = 1.833$. Once again, the solution becomes unstable, giving way to a chaotic motion before reaching a higher-cycle periodic motion through a Hopf bifurcation. The process of period multiplying keeps repeating for this new periodic window, as we can see in the enlarged bifurcation diagram shown in Figure 37.

Finally, in Figure 38, we plot the Poincaré section for $\beta = 1.869$, $\beta = 1.870$, and $\beta = 1.871$. These plots show the cascade of period-multiplying bifurcations. Figures 38a and 38c show periodic motions, and Figure 38b shows a quasi-periodic motion.

To conclude, in this section we presented the route to chaos for the bidirectional system under consideration. When $\beta = 1.516$ the solution is periodic, which loses stability due to the occurrence of a second impact on the same stopper. Although the bifurcation is a period-doubling bifurcation, no two-cycle periodic solution was found. Instead, the motion of the tube is chaotic. Finally, for high values of β, periodic windows appear through Hopf bifurcations and disappear through period-multiplying bifurcations.

4.5 Impact-Sliding Wear Work Rate

In this section, we are interested in the impact-sliding wear work rates as we increase β. We define the instantaneous dimensionless impact-sliding work rate at maximum penetration as

$$\dot{w}_{is}^{M} = -\mu F|_{\dot{x}=0} \dot{y}|_{\dot{x}=0} \tag{4.29}$$

where $\dot{y}|_{\dot{x}=0}$ is the dimensionless tangential tube velocity at maximum penetration and $F|_{\dot{x}=0}$ is the dimensionless impact force at maximum penetration; that is,

$$F|_{\dot{x}=0} = \Omega[x_0 - \frac{1}{2}(|x_0+1| - |x_0-1|)] \tag{4.30}$$

where $x_0 = x|_{\dot{x}=0}$. In Figures 39a and 39b, we plot $F|_{\dot{x}=0}$ - β and $\dot{w}_{is}^{M}$ - β, respectively. We note the drastic changes in the impact forces and instantaneous impact-sliding work rate as the tube motion behavior changes.

Assuming that the impact-sliding wear work rate function keeps the same shape at every impact, we can relate the mean impact-sliding wear work rate $\bar{\dot{w}}_{is}$ to $\dot{w}_{is}^{M}$ as

$$\begin{aligned} \bar{\dot{w}}_{is} &= \frac{1}{\tau}\int_0^{\tau} \dot{w}_{is}\, dt \\ &= \lambda \dot{w}_{is}^{M} \end{aligned} \tag{4.31}$$

where τ is the impact period. In Figures 40a to 40c, we plot $F|_{\dot{x}=0}$ - t, $F|_{\dot{x}=0}$ - t, and $\dot{w}_{is}^{M}$ - t on an enlarged scale for a value of $\beta = 1.700$, which gives an average value of $\lambda = 0.555$. Furthermore, because the gap is dimensionless, for an actual gap value of g, we need to multiply the impact forces by g and the impact-sliding wear work rate by g^2 to obtain the corresponding actual impact forces and impact-sliding wear work rate. Hence, for a gap value of g, we estimate the mean impact-sliding work rate as

$$\dot{\overline{W}}_{is} = g^2 \frac{1}{T} \int_0^T \dot{w}is \, dt \tag{4.32}$$

where T is a sufficient length of time to ensure a stationary value of $\dot{\overline{W}}_{is}$. Hence, using equation (4.28), we obtain

$$\dot{\overline{W}}_{is} = \frac{1}{T} g^2 \lambda \tau \sum_1^N \dot{w}_{is}^{M} \tag{4.33}$$

where N is the number of impact during T. Similarly, we can compute the mean impact forces as

$$\begin{aligned} \overline{F} &= \frac{1}{T} \int_0^T |F| \, dt \\ &= \frac{1}{T} g \nu \tau \sum_1^N F|_{\dot{x}=0} \end{aligned} \tag{4.34}$$

We found an average value of the shape factor $\nu = 0.580$.

Axisa et al. [32] computed the impact-sliding wear work rate for the same tube using a unidirectional motion model. For this unidirectional model, because no friction is defined, he estimated the impact-sliding wear work rate by

$$\dot{\overline{W}}_{is} = \alpha f_R \overline{F} \sigma_c \tag{4.35}$$

where f_R is the dominant frequency of the tube response, $\bar{F}$ is the mean value of the impact forces, σ_c is the displacement rms, and α is a shape factor, which depends on geometrical considerations such as the tube orbital motion and support. Furthermore, the authors performed also bidirectional calculations and found that α varies between 3 and 7. In Figure 41, we present the mean wear work rates and impact forces obtained by the bidirectional models for a gap value of $g = 0.5\,mm$, as we increase β. The mean impact-sliding wear work rate and the mean impact forces obtained from unidirectional model overestimates [34] the actual values, thereby leading to a tube life expectancy that is short compared with the observations in power plants. Hence, besides being physically more realistic, taking into account friction in the bidirectional model reduces the estimates of the impact forces and impact-sliding wear work rates. However, we have not computed the tube life expectancy using the bidirectional model. This computation is needed to validate the methods and results presented in this work.

5. CONCLUSION AND FUTURE WORK

5.1 Conclusions

Different techniques have been developed to investigate the route to chaos for a constrained tube subjected to cross flow. We have not succeeded in implementing the method of harmonic balance for two principal reasons; the nonlinear term derivatives are discontinuous and hence produce numerical instabilities in the computation of the Jacobi matrix and the motion period is unknown and hence also brings numerical instabilities in the Fourier-series coefficients.

The combination of the shooting method with Poincaré sections and bifurcation diagrams appears to be the right choice to investigate the tube behavior. We introduce a new application of the method of multiple scales for one mode and for a cubic spring. We obtain an analytical solution of the periodic cycle, which is in good agreement with the solution obtained using the shooting method for small control parameter. Also, the numerical results complete and confirm the work done by Axisa et al. [32], Paidoussis et al. [33], and De Langre et al. [34] concerning the existence of chaotic tube motions in steam generators. We extend their work by considering bifurcation of a bidirectional model involving a nonlinear friction

term. Furthermore, we show that a single-mode system (mainly the first harmonic) is not responsible for bifurcation because it undergoes relaxation oscillations. As a result, the qualitative behavior changes and chaos are due to modal interactions. Another, physical observation is that the first bifurcation occurs when a second impact on the same stopper occurs. After the bifurcation, the tube undergoes intermittent chaotic behavior alternating with a transient one-impact motion. The intermittent chaos is explained by the instability of the one-cycle solution when a two-impact motion occurs and the energy dissipated by friction. Furthermore, it seems that each bifurcation is accompanied by chaotic behavior before the motion is stabilized in a periodic window. As in [33], we found that chaotic motions appear through cascades of period multiplying bifurcations and disappear through Hopf bifurcations. Lastly, in Section 4.5, we showed the drastic change in wear work rate, as we pass a bifurcation; it is often characterized by chaos. Using a bidirectional model involving frictional forces, we found values of impact forces and impact-sliding wear work rates lower by a factor of 20 than the results found by Axisa et al. [32], which are known overestimate the actual rates.

5.2 Future Work

In this work, we presented numerical and analytical methods to investigate the dynamics of a tube subjected to a fluid-stiffness controlled mechanism. As already mentioned, we emphasize the theoretical aspects, such as the phenomenon underlying chaotic motions. Therefore, we considered pinned-pinned tubes with one bidirectional impact instead of the actual bent tubes that are multi-supported. Hence, from the design point of view, these methods should be applied on a more realistic mechanical system.

We presented an application of the method of multiple scales to a single-mode system with cubic spring. For small values of β, the good agreement between the analytical results and

the numerical simulation is encouraging to pursue of the application of the method of multiple scales to several modes with three linear springs.

Finally, experimental studies appear essential to validate the methods and the results and the effect of friction on the impact forces and impact-sliding wear work rates should be investigated further.

REFERENCES

1. H.J. Connors 1970 Symposium on Flow-Induced Vibration in Heat Exchangers, ASME, 42-56. "Fluid-elastic vibration of tube arrays excited by cross-flow".

2. R.D. Blevins 1974 Journal of Pressure Vessel Technology 96, 263-267. "Fluid-elastic whirling of a tube row".

3. R.D. Blevins 1977 Journal of Fluid Engineering 99, 457-461. "Fluid elastic whirling of tube rows and tube arrays".

4. Y.N. Chen and M. Weber 1970 Symposium on Flow-Induced Vibration in Heat Exchangers, ASME, 57-77. "Flow-induced vibration in tube bundle heat exchangers with cross and parallel flow".

5. M.P. Paidoussis 1965-66 Proceedings Instrumentation Mechanical Engineering 180, 268-279. "Vibration of flexible cylinders with supported ends, induced by axial flow".

6. M.P. Paidoussis and S.J. Price 1984 Journal of Fluid Engineering 108, 193-199. "A single-flexible-cylinder analysis for the fluid-elastic instability of an array of flexible cylinder in cross-flow".

7. M.P. Paidoussis and S.J. Price 1988 Journal of Fluid Mechanics 187, 45-59. "The mechanism underlying flow induced instability of cylinder arrays in cross-flow".

8. S.J. Price and N. Valerio 1989 Flow-Induced Vibration 154, 1-9. "A non-linear investigation of single-degree-of freedom instability in cylinders arrays in cross-flow".

9. A.H. Nayfeh 1981, Introduction to Perturbation Techniques, Wiley, NY.

10. S.S. Chen 1977 Proceedings Third International Conference on Pressure Vessel Technology, Tokyo, Part I, 415-426. "A mathematical model for cross-flow induced vibration of tube rows".

11. S.J. Price and M.P. Paidoussis 1983 Journal of Vibration, Acoustics, Stress and Reliability in Design 105, 59-66. "Fluid-elastic instability of an infinite double row of circular cylinders subject to a uniform crossflow".

12. A. Bokaian and F. Geoola 1984 Journal of Fluid Mechanics 146, 383-415. "Wake-induced galloping of two interfering circular cylinders".

13. A. Bokaian and F. Geoola 1984 Journal of Fluid Mechanics 146, 417- 449. "Proximity-induced galloping of two interfering circular cylinders".

14. S.J. Price and M.P. Paidoussis 1983 Journal of Wind Engineering and Industrial Aerodynamics 17, 329-347. " The aerodynamics forces acting on groups of two and three circular cylinders when subject to a cross-flow".

15. P.M. Moretti and R.L. Lowery 1976 Journal of Pressure Vessel Technology 98, 190-193. "Hydrodynamic inertia for a tube surrounded by rigid tubes".

16. B.T. Lubin, K.H. Haslinger, A. Puri, and J. Goldberg 1977 Journal of Fluid Engineering 99, 416-418. "Frequency response of a tube bundle in water".

17. S.S. Chen, J.A. Jendrzejczyk, and M.W. Wambsganss 1977 Fluid Structure Interaction Phenomena in Pressure Vessel in Piping Systems PVP-PB-026, 19-36. "An experimental and theoretical investigation of coupled vibration of tube banks".

18. S.S. Chen and J.A. Jendrzejczyk 1981 Journal of Pressure Vessel Technology 103, 130-135. "Flow velocity dependence of damping in tube arrays subjected to liquid crossflow".

19. H. Tanaka and S.Takahara 1981 Journal of Sound and Vibration 77, 19-37. "Fluid-elastic vibration of tube array in cross flow".

20. H. Tanaka, S.Takahara, and K. Hota 1982 Journal of Pressure Technology 104, 168-176. "Flow-induced vibration of tube arrays with various pitch-to-diameter ratio".

21. H.G.D. Goyder and C.E. Teh 1984 Proceedings ASME Symposium on Flow-Induced Vibrations 2, 151-163. "Measurement of the destabilizing forces on vibrating tube in a fluid cross flow".

22. S.S. Chen 1983 Journal of Vibration, Acoustics, Stress and Reliability in Design 105, 253-260. "Instability mechanism and stability criteria of a group of circular cylinders subjected to crossflow".

23. S.S. Chen 1987 Journal of Fluids and Structures 1, 35-53. "A general theory for dynamic instability of tube arrays in crossflow".

24. M.P. Paidoussis and S.J. Price 1984 Journal of Sound and Vibration 97, 615-640. "An improved mathematical model for the stability of cylinder rows subject to cross-flow."

25. M.P. Paidoussis and S.J. Price 1986 Journal of Sound and Vibration 105, 121-142. "A constrained-mode analysis of the fluid-elastic instability of a double row of flexible circular cylinders subject to cross-flow".

26. D.S. Weaver and D. Koroyannakis 1982 Journal of Pressure Vessel Technology 104, 139-146. "The cross-flow response of a tube array in water - A comparison with the same array in air". bundle in air and water".

27. J.H. Lever and D.S. Weaver 1982 Journal of Pressure Vessels Technology 104, 147-158. "A theoretical model for fluid-elastic-instability-in heat exchanger tube bundles".

28. J.H. Lever and D.S. Weaver 1986 Journal of Sound and Vibration 107, 393-410. "On the stability of heat exchanger tube bundles. Part II: Numerical results and comparisons with experiments".

29. D.S. Weaver and M. El-Kashlan 1981 Journal of Sound and Vibration 76, 283-294. "The effect of damping and mass ratio on the stability of a tube bank."

30. B.M.H. Soper 1980 Symposium on Flow Induced Heat Exchanger Tube Vibration ASME 9, 1- 9. "The effect of layout on the fluid-elastic instability of tube bundles in cross-flow."

31. M.J. Pettigrew, Y. Sylvestre, and A.O. Campagna 1978 Nuclear Engineering and Design 48, 97-115. "Vibration analysis of heat exchanger and steam generator designs."

32. F.Axisa, J. Antunes, and B. Villard 1988 Journal of Pressure Vessel Technology 110, 6-14. "Overview of numerical methods for predicting flow-induced vibration".

33. M.P. Paidoussis and G.X. Li 1992 Journal of Sound and Vibration 152, 305-326. "Cross-flow-induced chaotic vibrations of heat-exchanger tubes impacting on loose supports".

34. C.Hadj-Sadok and E. de Langre 1991 Rapport DMT/91.420, CEA Saclay "Reponse non-linear a l'instabilite fluide-elastique: modele de couplage anti-symetrique de raideur".

35. S. Lukasewicj 1979 Local Loads in Plates and Shells, Nooordhoff The Netherlands International Publishers.

36. A.H. Nayfeh and B. Balachandran 1993, Nonlinear Dynamics: Concept and Application, Wiley, NY.

37. A.H. Nayfeh and D.T. Mook 1979, Nonlinear Oscillations, Wiley, NY.

38. Y.B. Kim and S.T. Noah 1990, Nonlinear Dynamics 1, 221-241. "Bifurcation analysis for a modified Jeffcott rotor with bearing clearances".

39. Y.B. Kim and S.T. Noah 1991, Nonlinear Dynamics 2, 215-234. "Response and bifurcation analysis of a MDOF rotor system with a strong nonlinearity".

40. J. Stoer and R. Bulirsch 1980, Introduction to Numerical Analysis, Springer-Verlag, NY.

41. T.S. Parker and L.O. Chua 1989 Practical Numerical Algorithms for Chaotic System, Springer-Verlag, NY.

Figure Captions

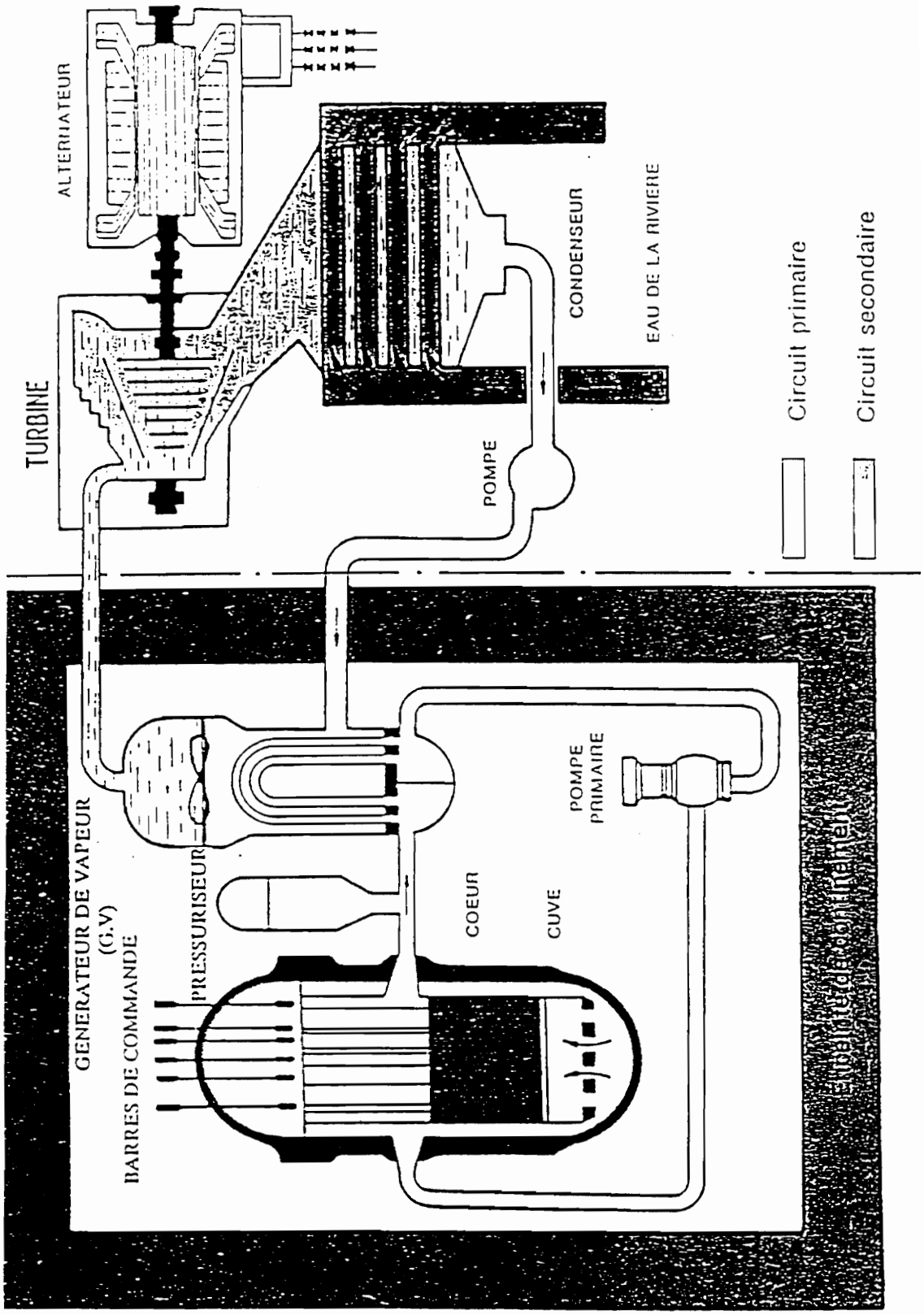

Figure 1 Schematic of a nuclear power plane from [34].

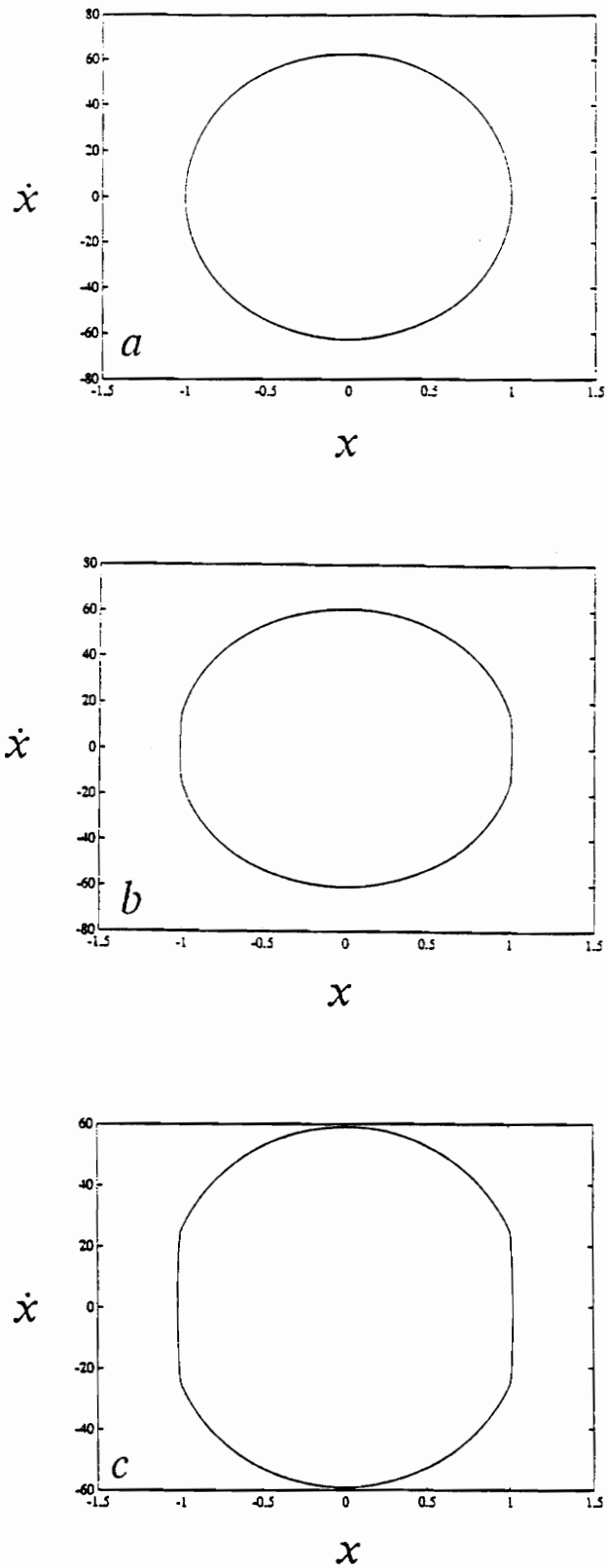

Figure 2 A two-dimensional projection of the phase portrait on the $\dot{x}$-x plane for (a) $\beta = 1.200$; (b) $\beta = 3.000$; and (c) $\beta = 4.500$.

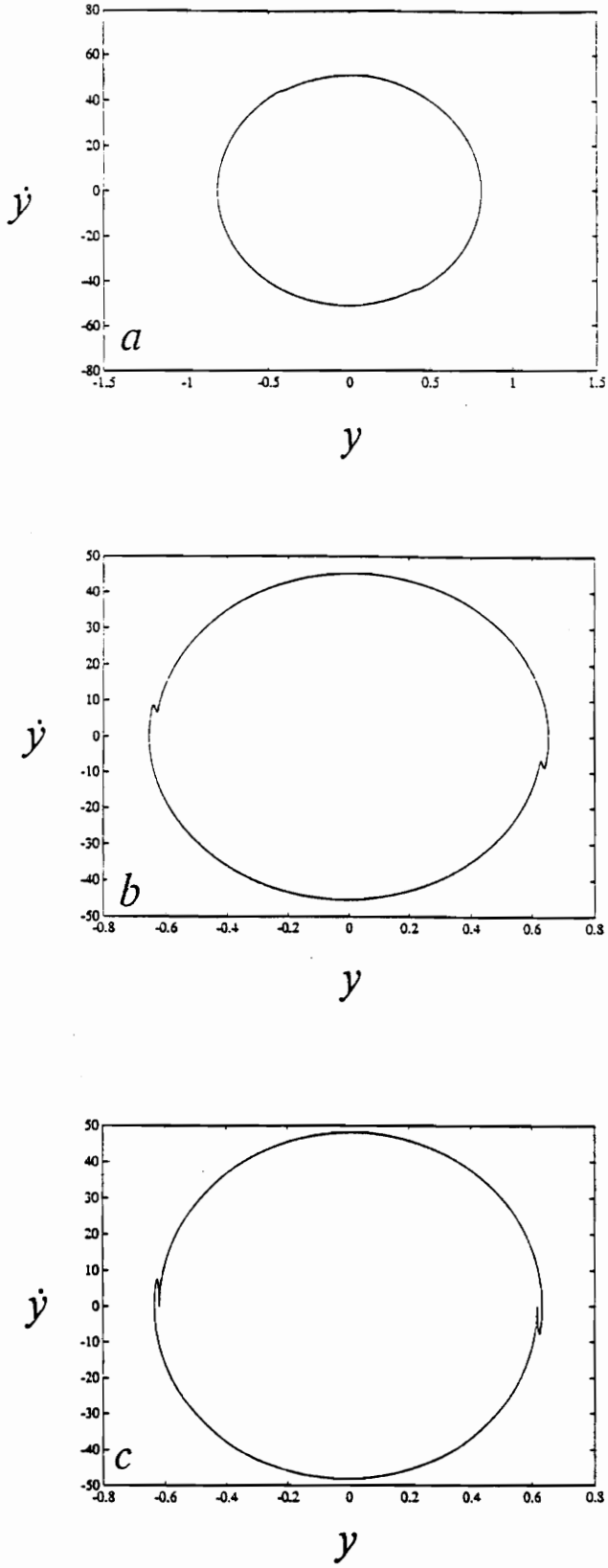

Figure 3 A two-dimensional projection of the phase portrait on the $\dot{y}$-y plane for (a) $\beta = 1.200$; (b) $\beta = 3.000$; and (c) $\beta = 4.500$.

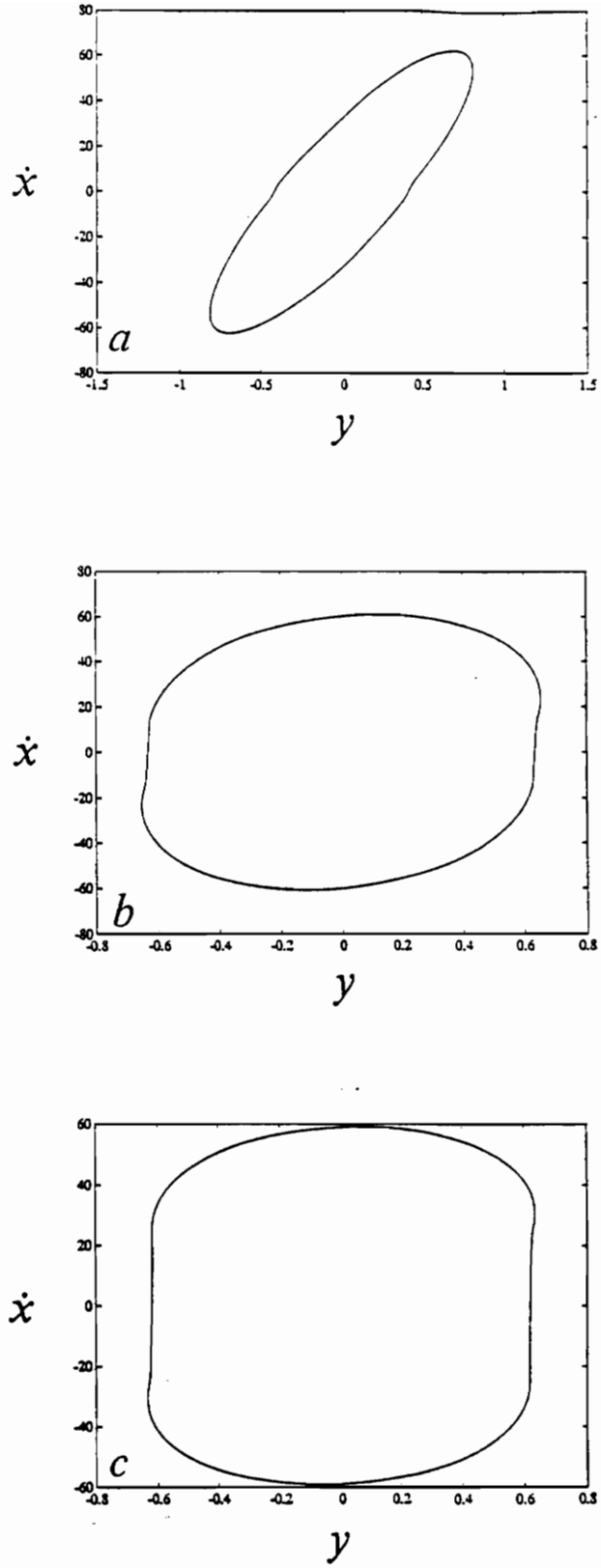

Figure 4 A two-dimensional projection of the phase portrait on the $\dot{x}$-y plane for (a) $\beta = 1.200$; (b) $\beta = 3.000$; and (c) $\beta = 4.500$.

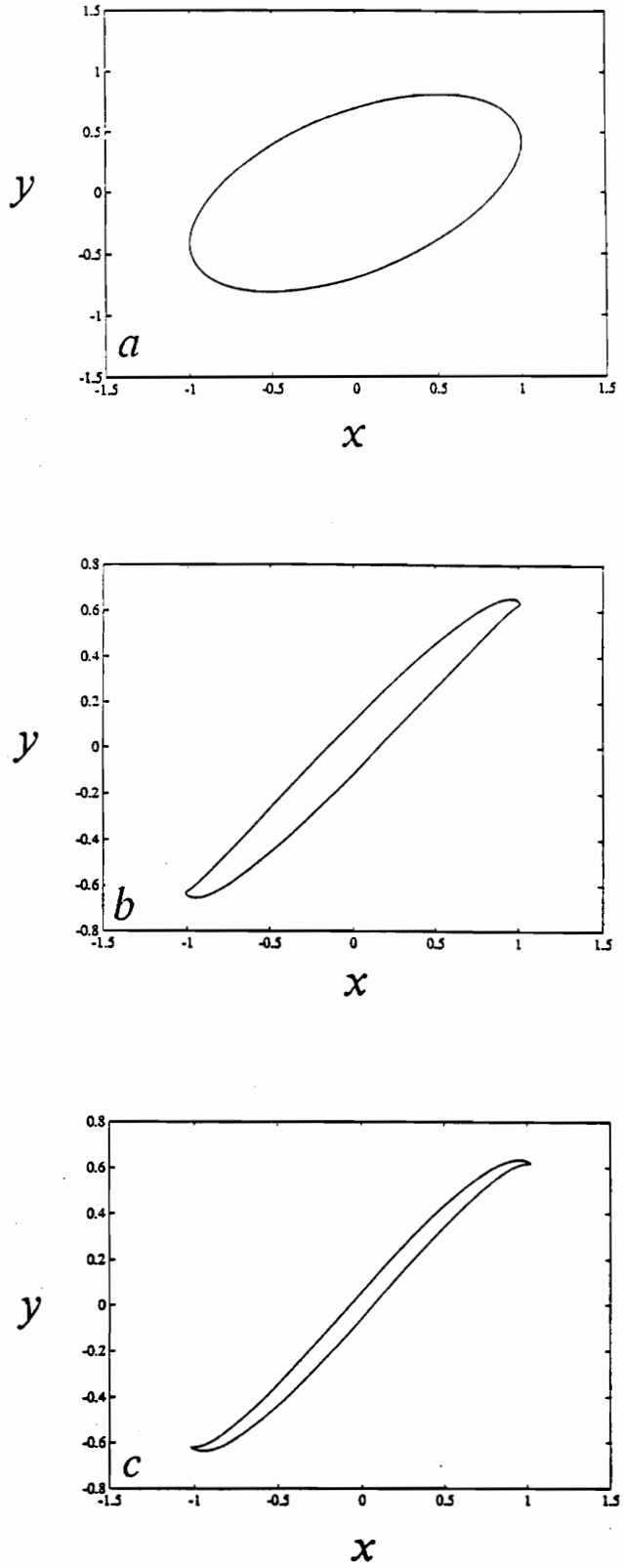

Figure 5 A two-dimensional projection of the phase portrait on the y-x plane for (a) $\beta = 1.200$; (b) $\beta = 3.000$; and (c) $\beta = 4.500$.

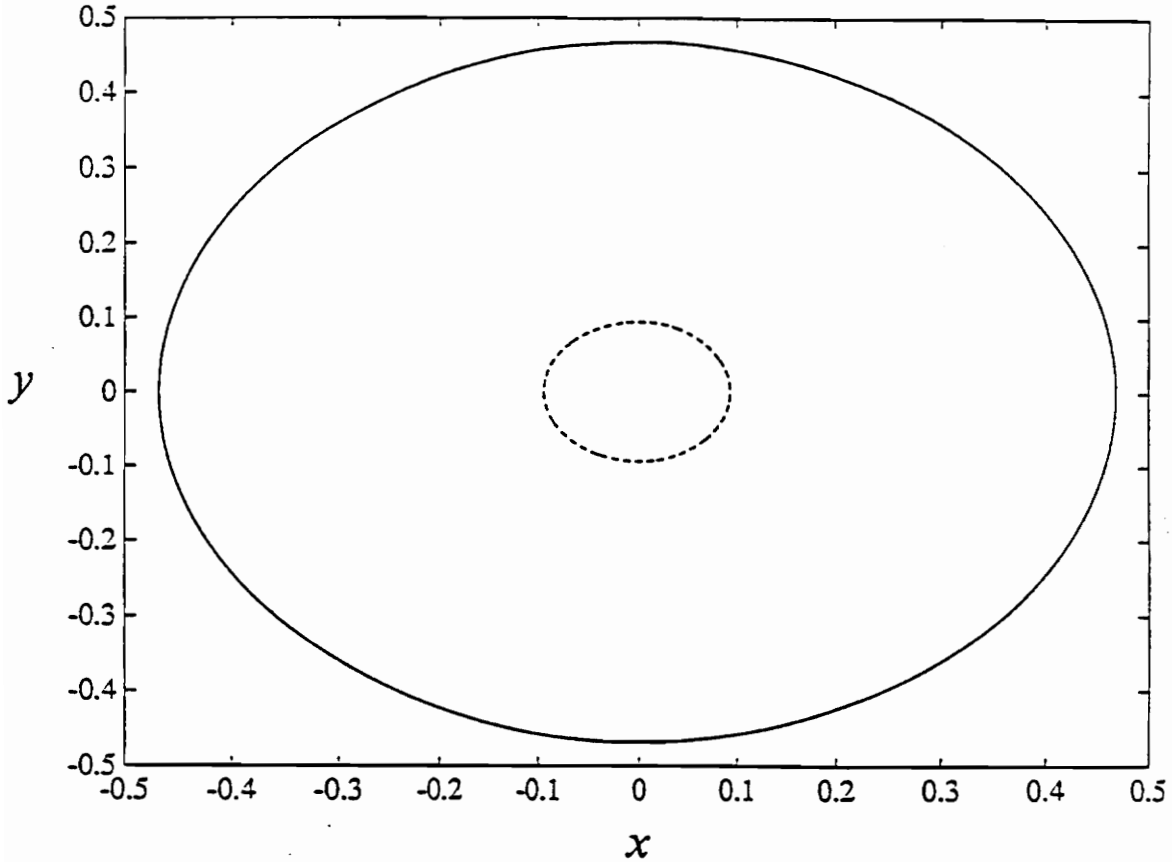

Figure 6 Periodic solutions for a marginally stable tube (i.e., $\beta = 1.000$) for two sets of initial conditions: η_1 (dashed line) and $\eta_2 = 5\eta_1$ (solid line).

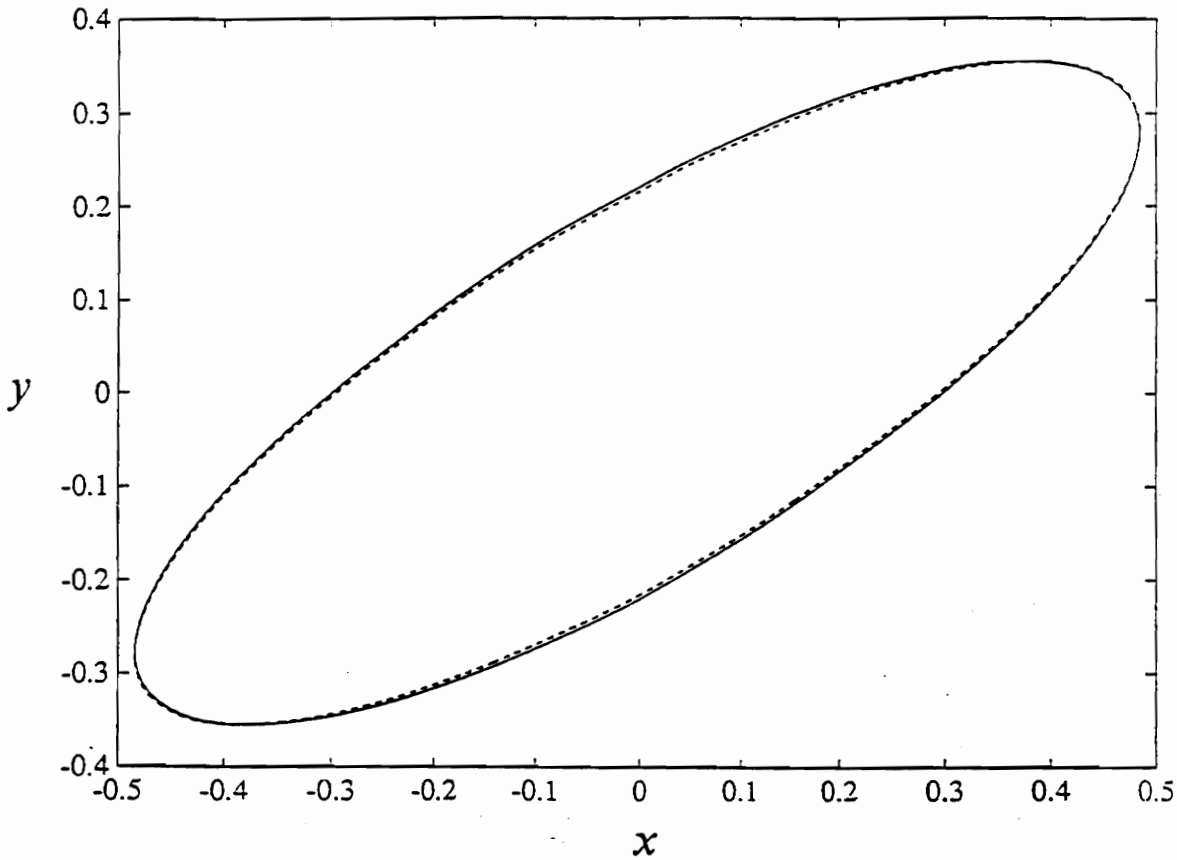

Figure 7 Comparison between the analytical solution (dashed line) and the numerical solution (solid line) y-versus-x plot for a cubic spring model and $\beta = 1.500$.

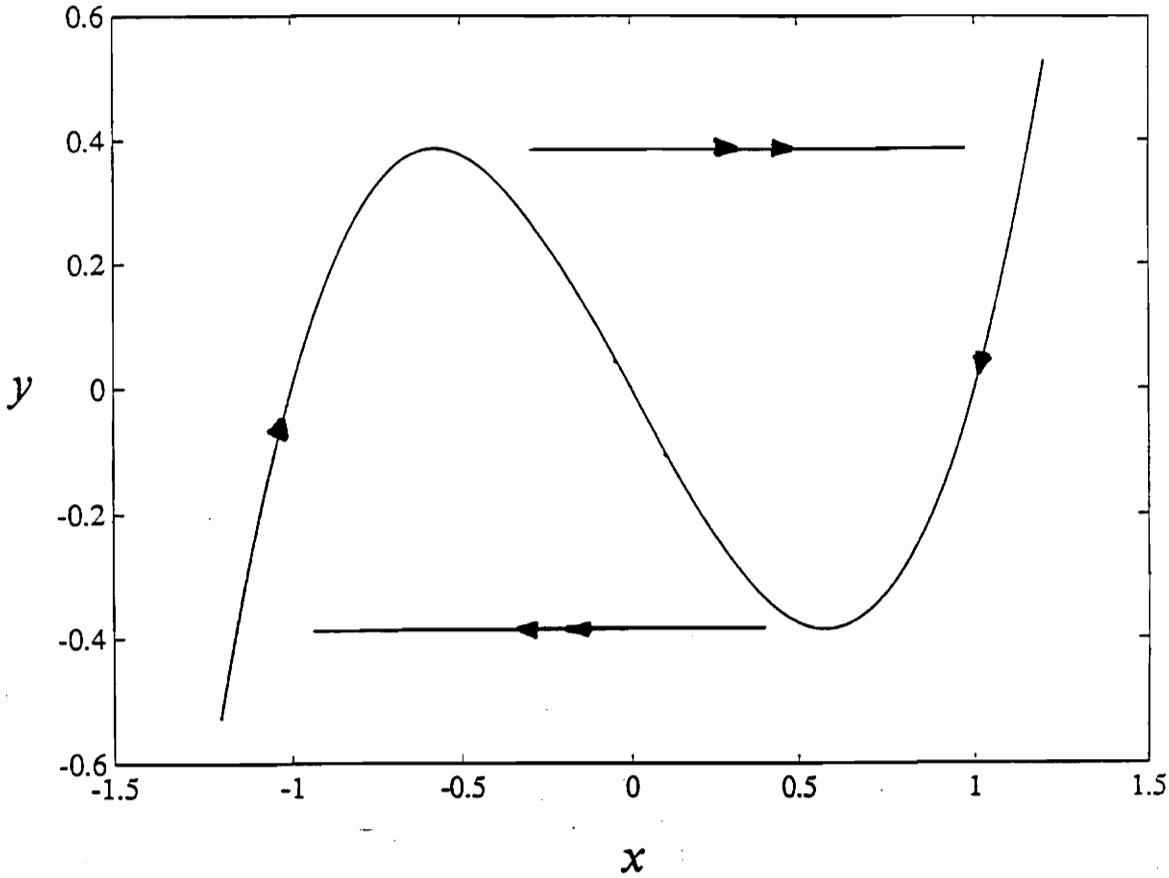

Figure 8 Rayleigh oscillator slow manifold, *y* versus *x*.

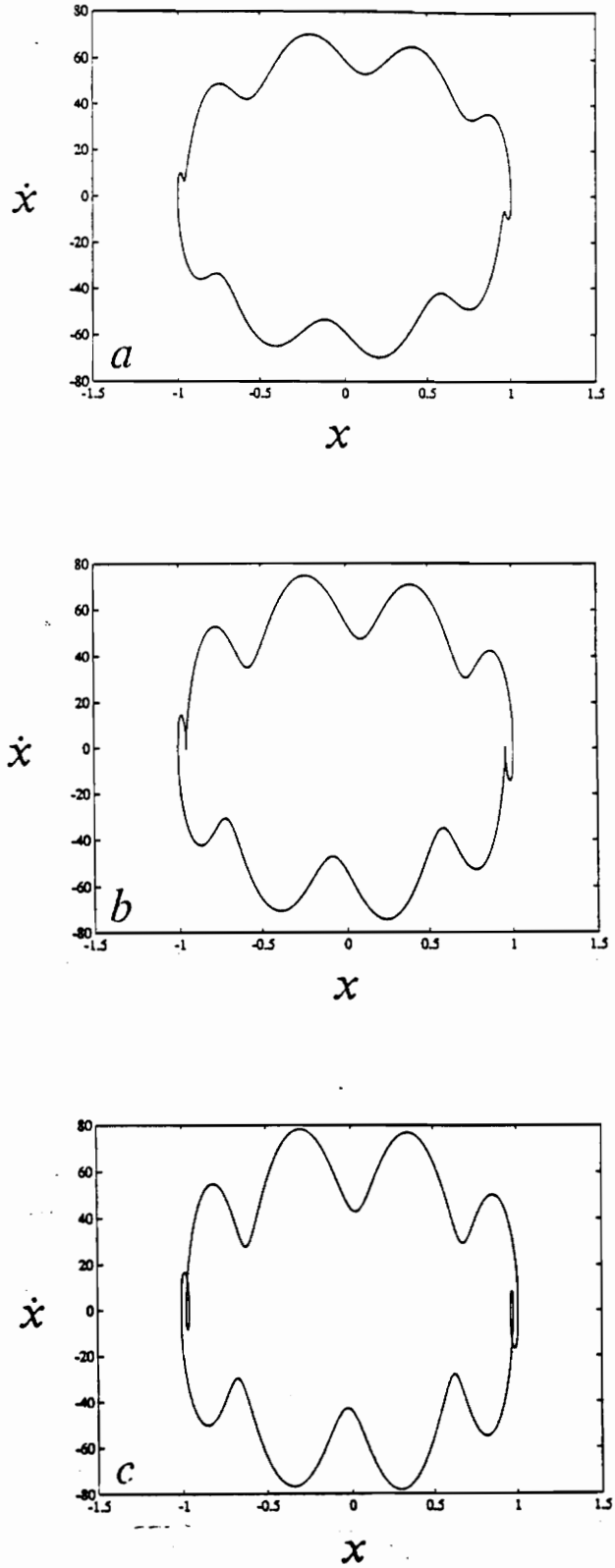

Figure 9 A two-dimensional projection of the phase portrait on the $\dot{x}$-x plane for (a) $\beta = 1.300$; (b) $\beta = 1.600$; and (c) $\beta = 1.750$

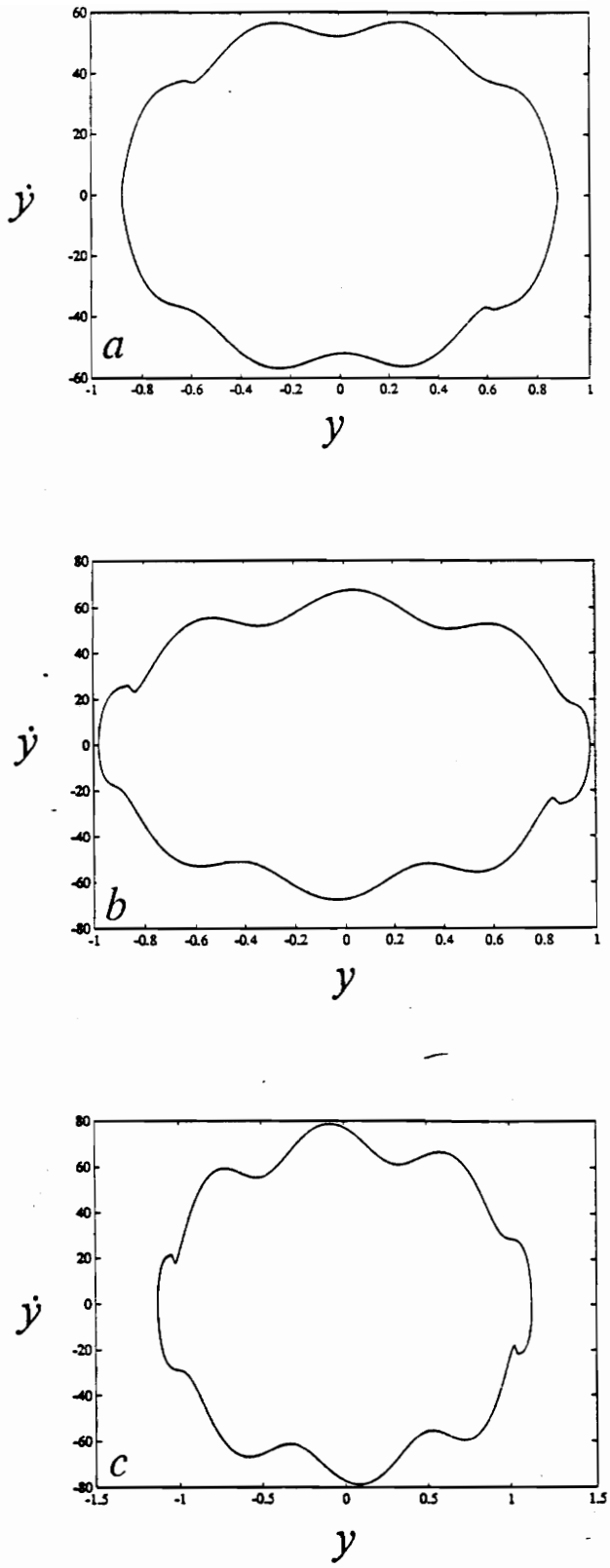

Figure 10 A two-dimensional projection of the phase portrait on the $\dot{y}$-y plane for (a) $\beta = 1.300$; (b) $\beta = 1.600$; and (c) $\beta = 1.750$

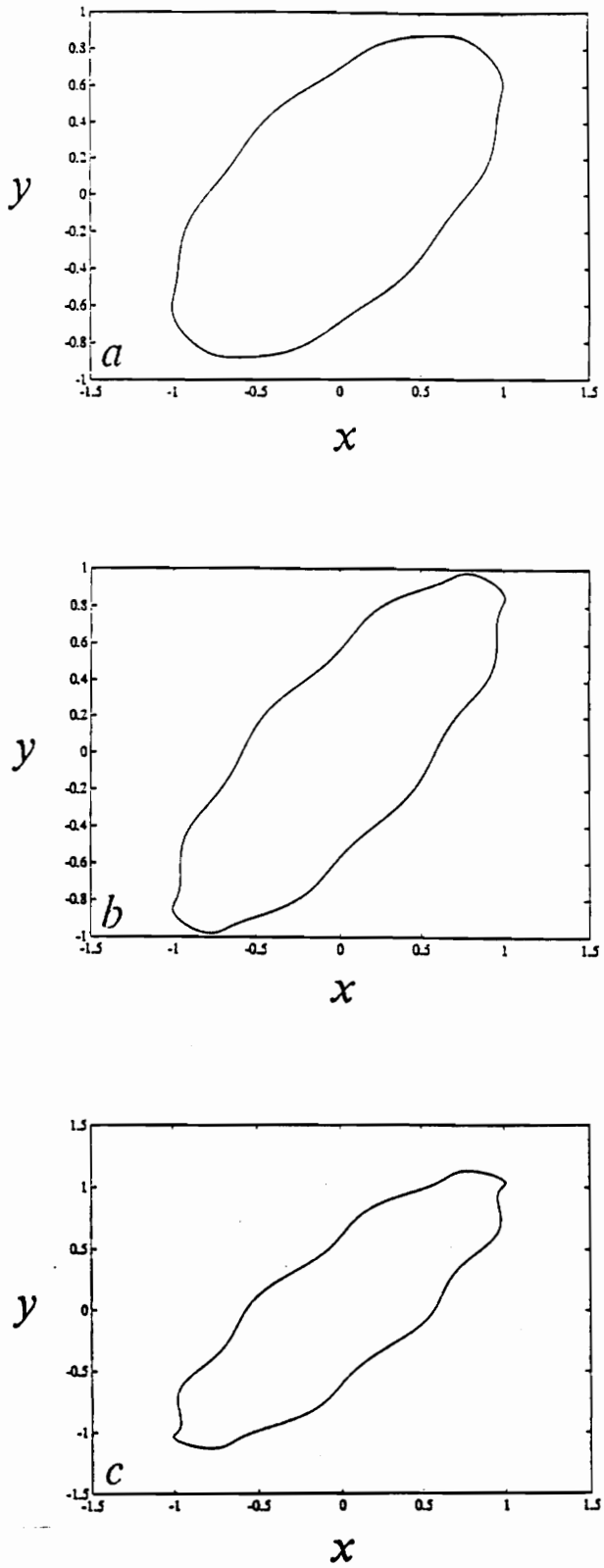

Figure 11 A two-dimensional projection of the phase portrait on the y-x plane for (a) $\beta = 1.300$; (b) $\beta = 1.600$; and (c) $\beta = 1.750$

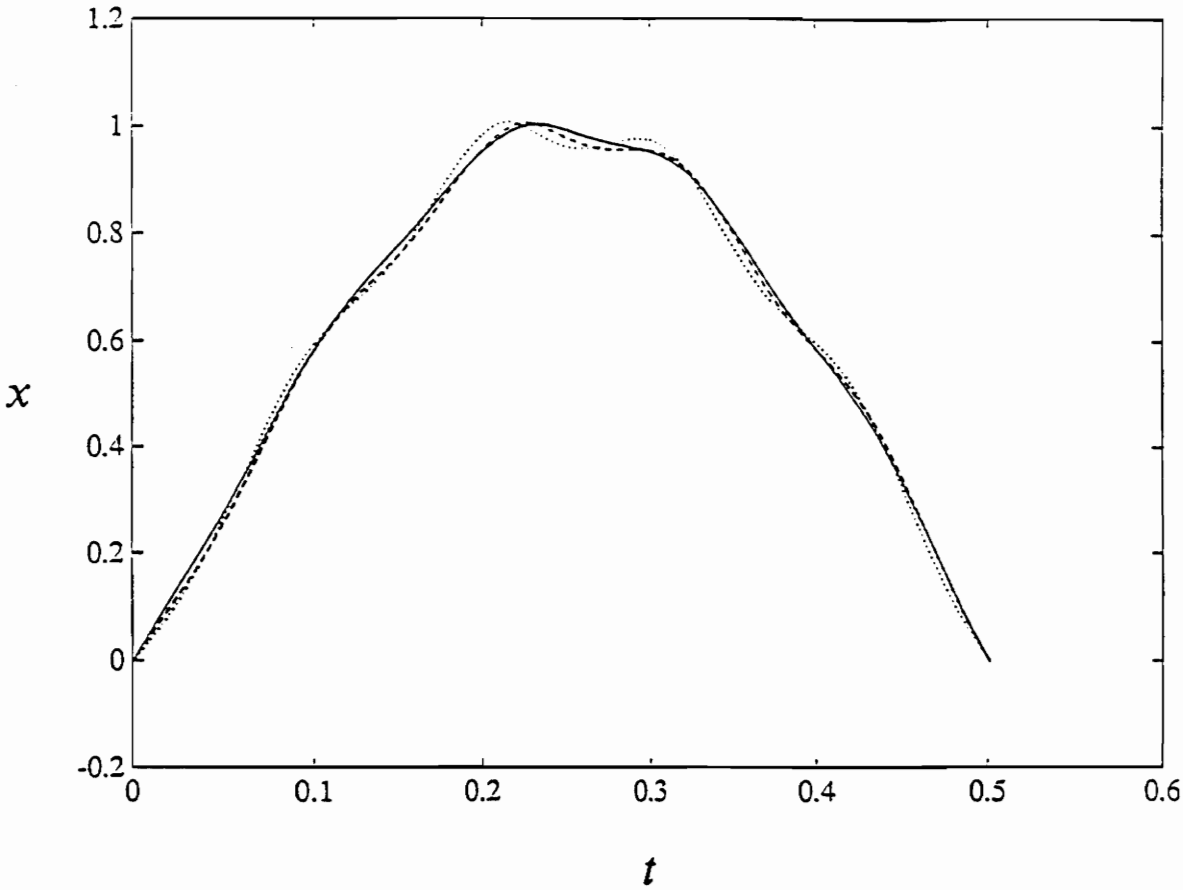

Figure 12 Impact analysis of one half of a period: x versus time for $\beta = 1.300$ (solid line); $\beta = 1.600$ (dashed line); and $\beta = 1.750$ (dotted line).

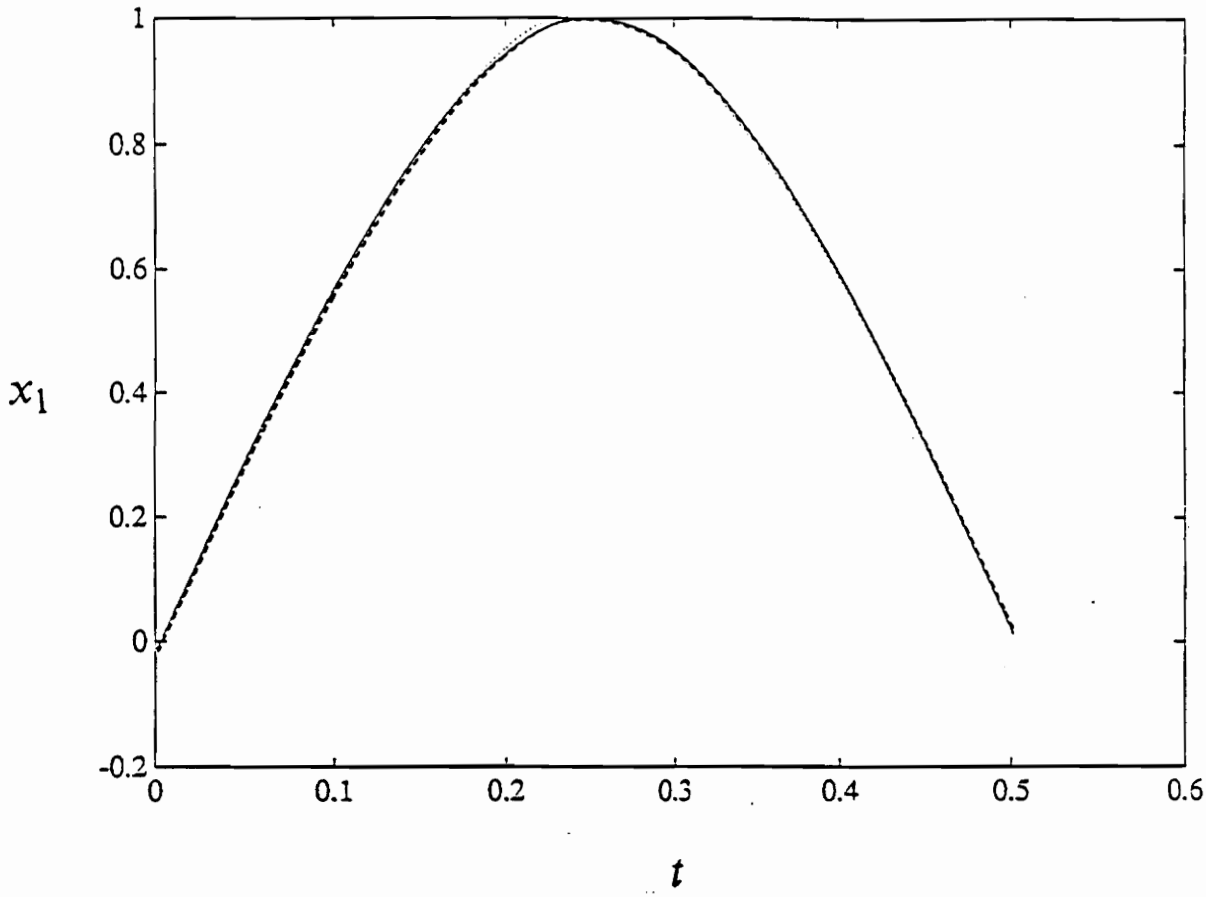

Figure 13 Impact analysis of the first mode response: x_1 versus time for $\beta = 1.300$ (solid line); $\beta = 1.600$ (dashed line); and $\beta = 1.750$ (dotted line).

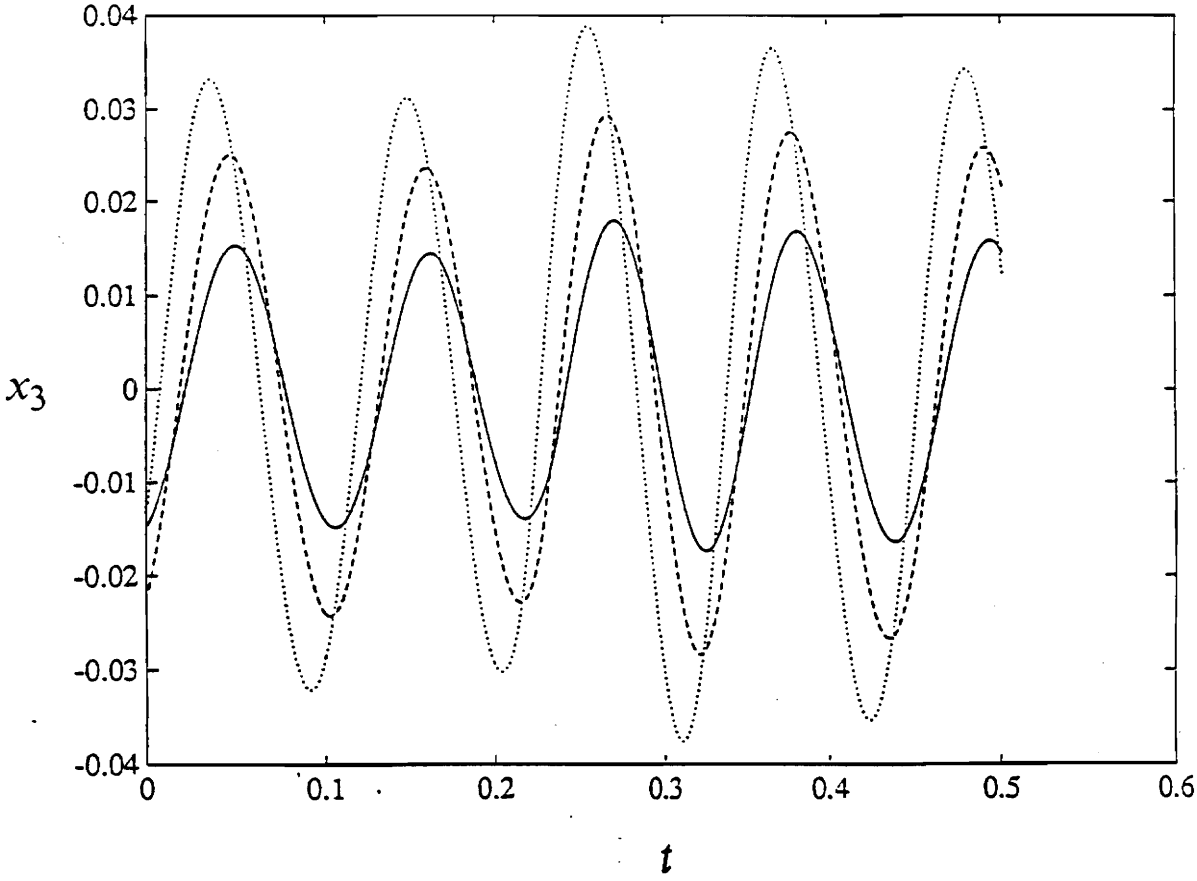

Figure 14 Impact analysis of the third mode response: x_3 versus time for $\beta = 1.300$ (solid line); $\beta = 1.600$ (dashed line); and $\beta = 1.750$ (dotted line).

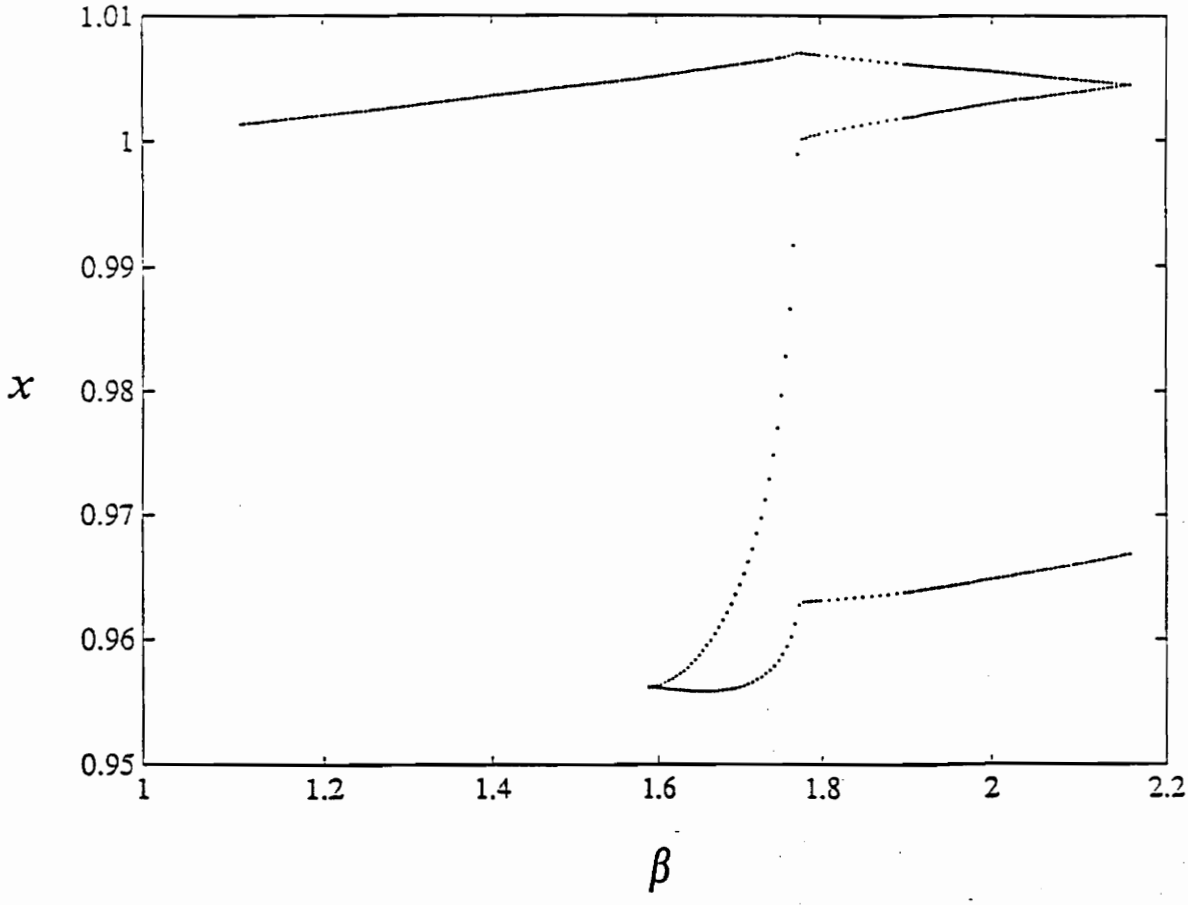

Figure 15 Bifurcation diagram of x versus β obtained by using the shooting method (hyperplane: $\dot{x} = 0$ and $x > 0$).

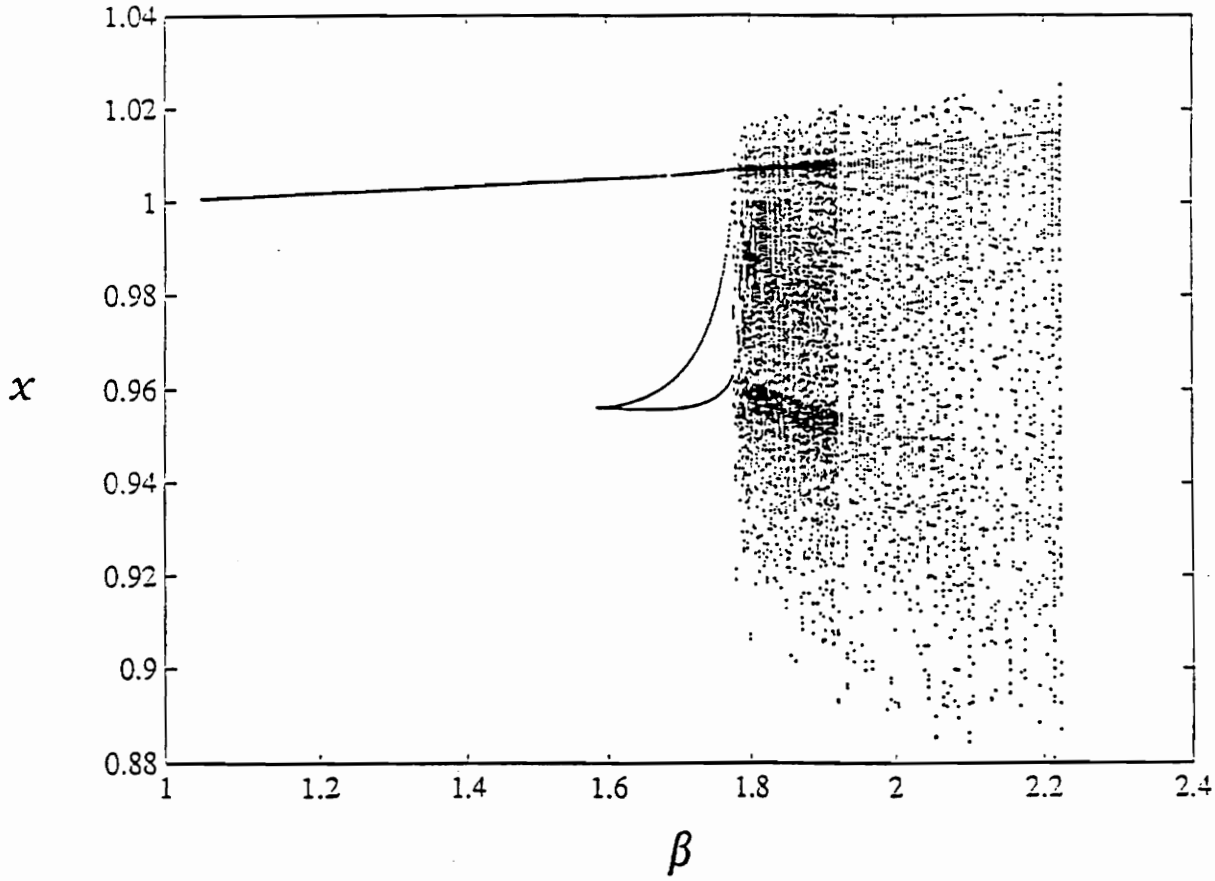

Figure 16 Bifurcation diagram of x versus β obtained by using direct integration (hyperplane: $\dot{x} = 0$ and $x > 0$).

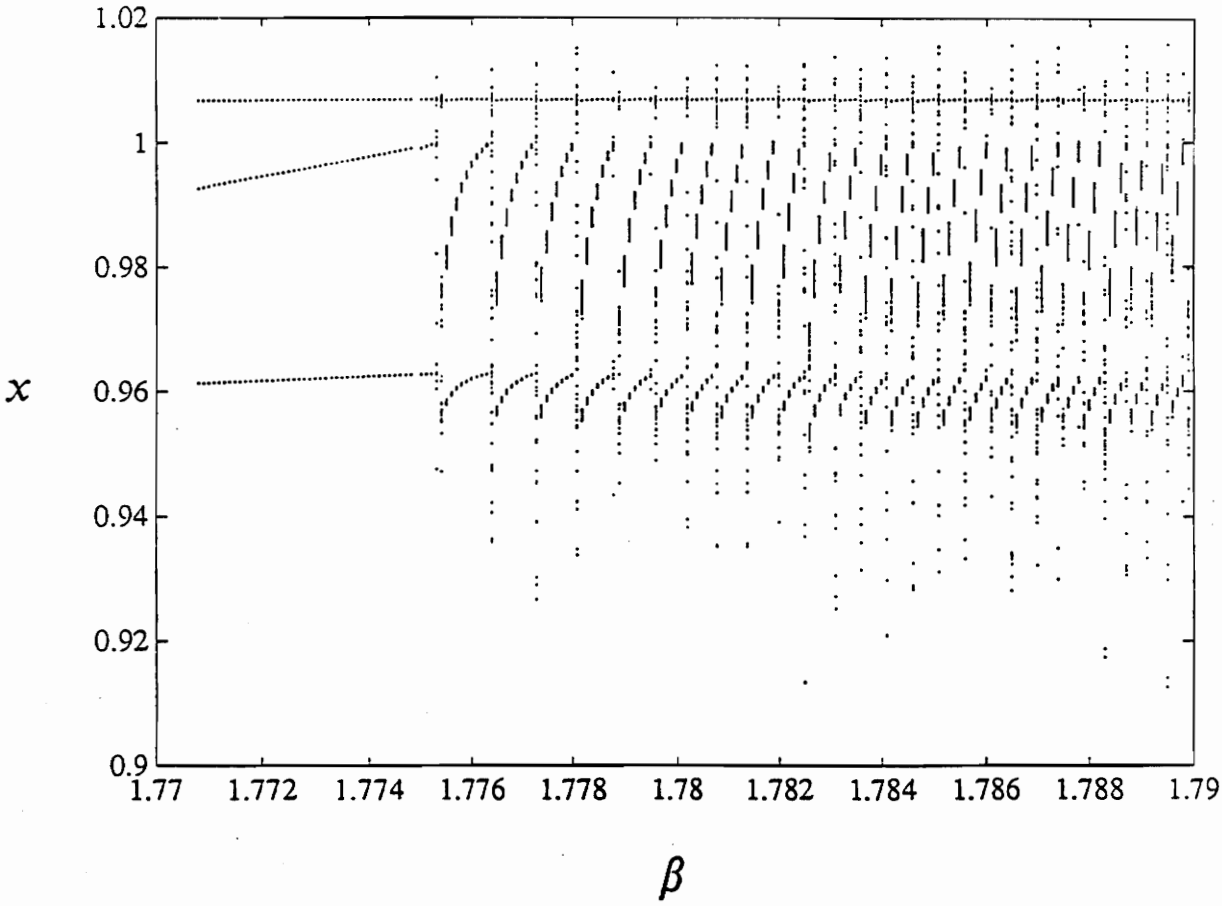

Figure 17 Enlarged bifurcation diagram of x versus β at the bifurcation point, (hyperplane: $\dot{x} = 0$ and $x > 0$).

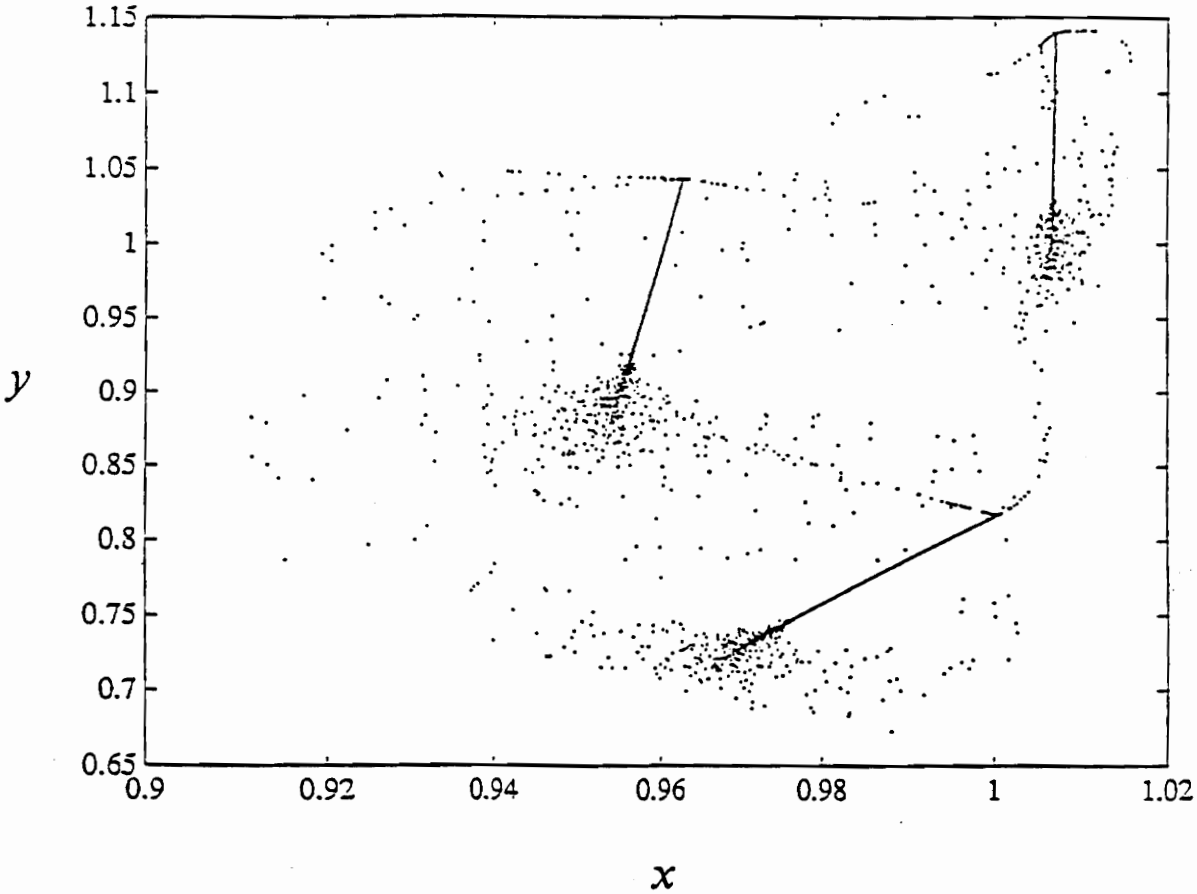

Figure 18 Poincaré section of y versus x for $\beta = 1.779$ (hyperplane $\dot{x} = 0$ and $x > 0$).

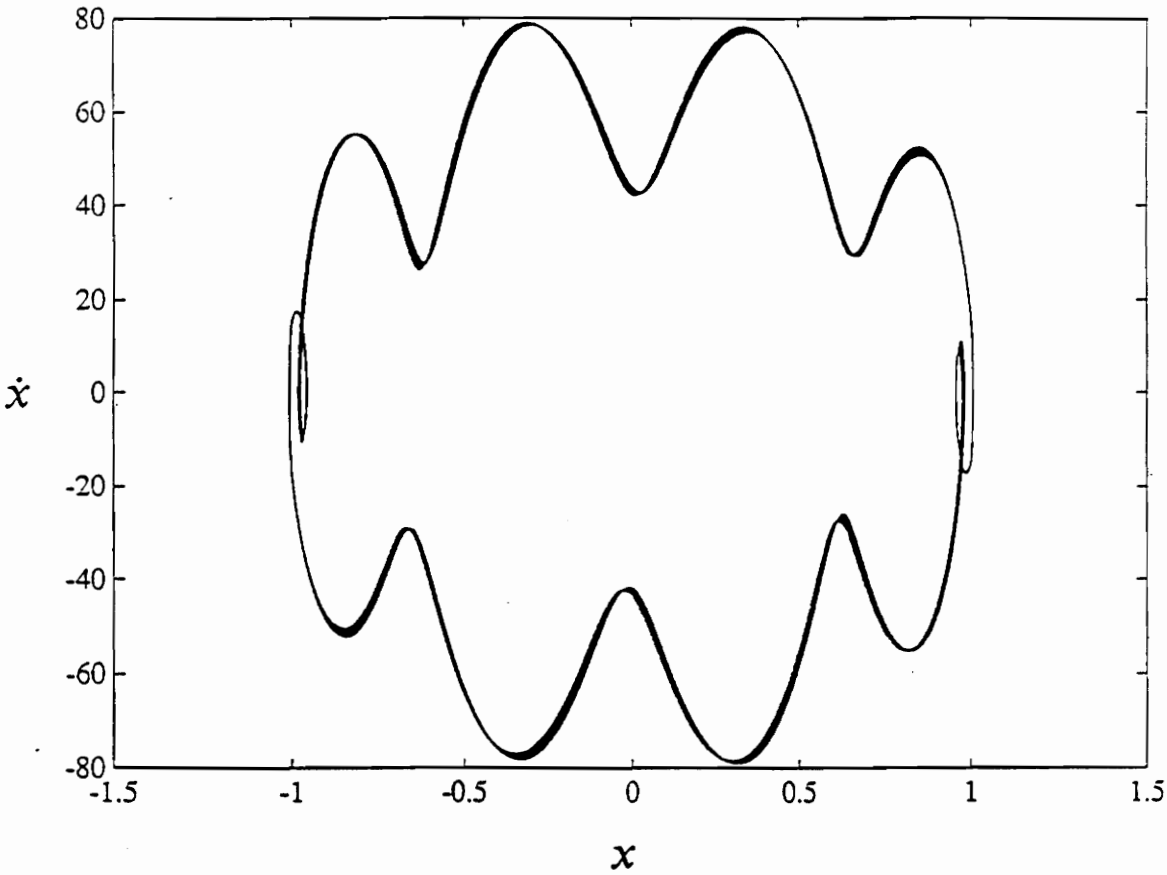

Figure 19 Phase portrait of $\dot{x}$ versus x for $\beta = 1.779$

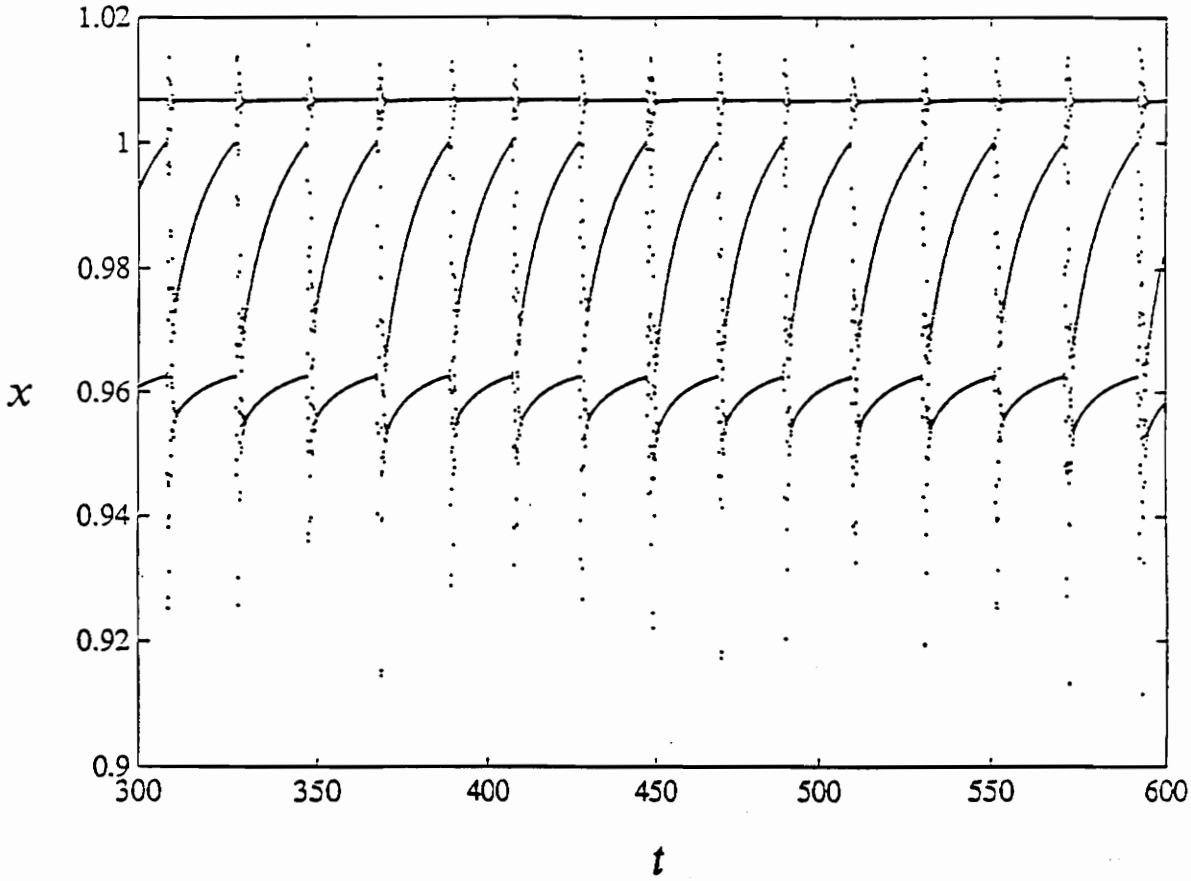

Figure 20 Variation of the x with t for $\beta = 1.779$ (hyperplane: $\dot{x} = 0$ and $x > 0$).

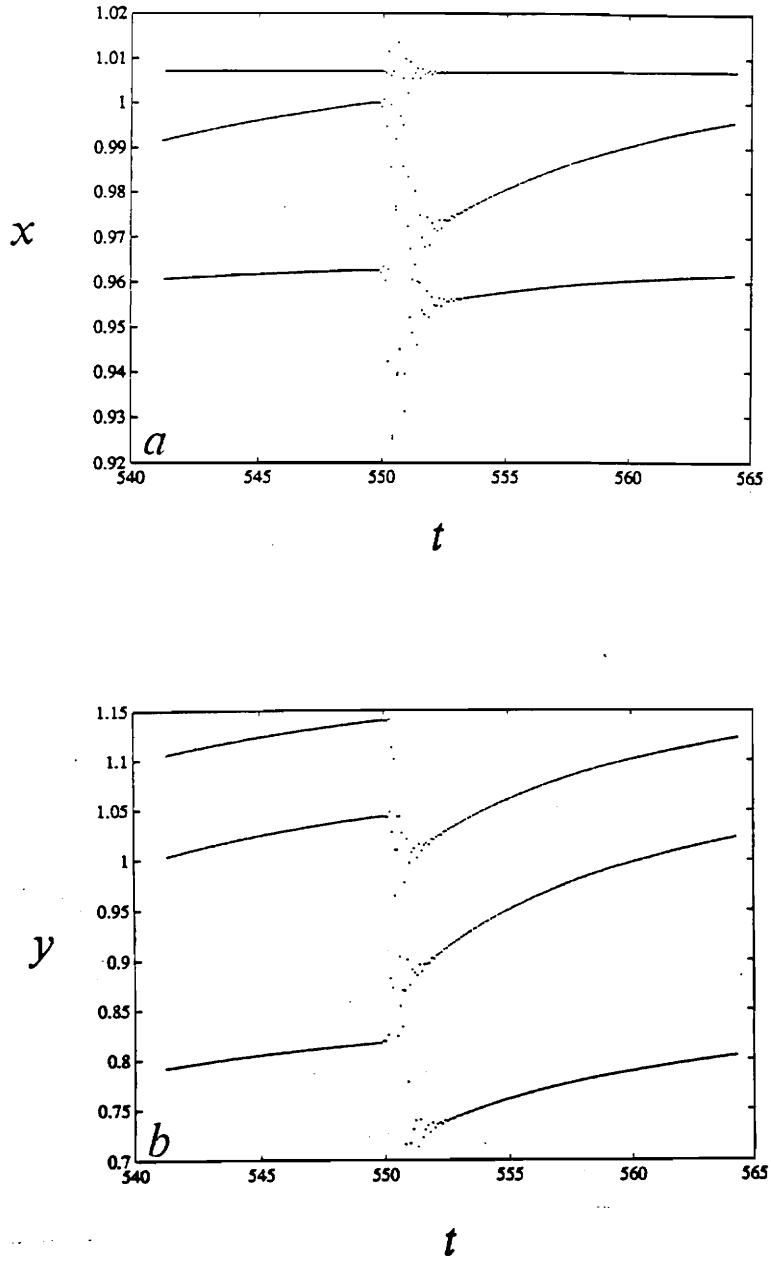

Figure 21 Enlarged portion of the time variation of x and y (a) x versus t and (b) y versus t for $\beta = 1.779$ (hyperplane: $\dot{x} = 0$ and $x > 0$).

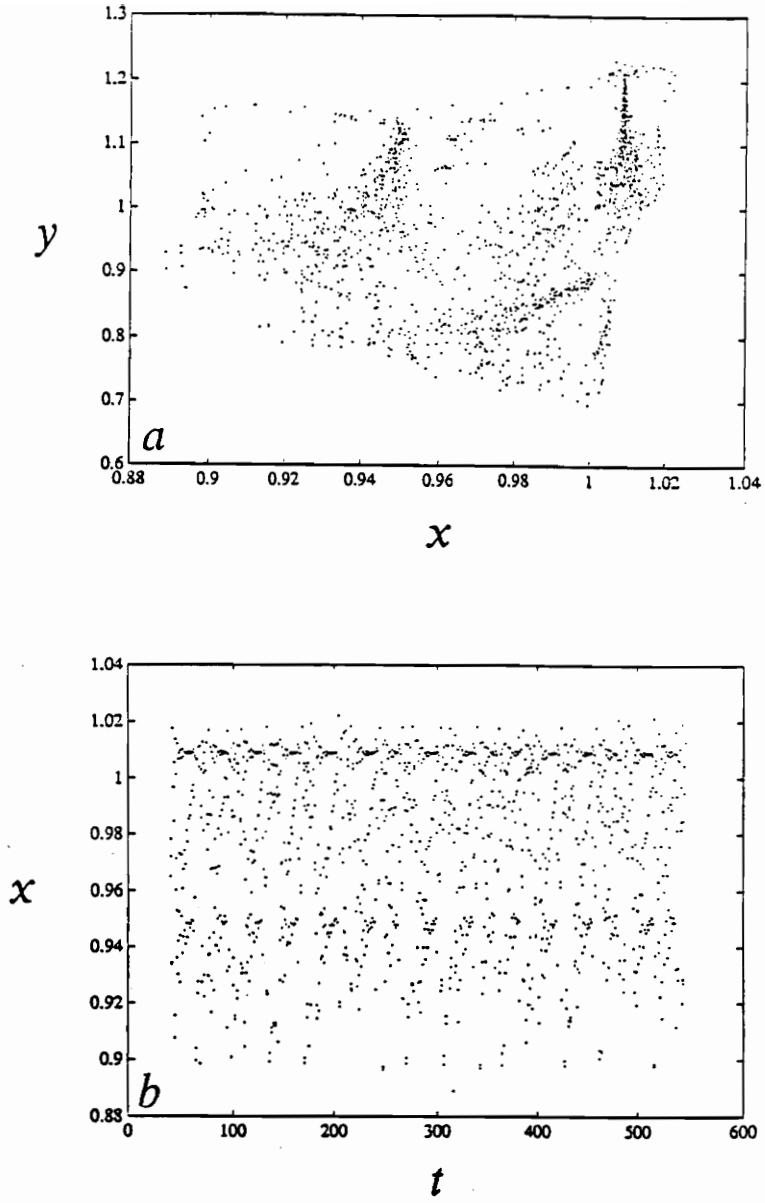

Figure 22 Two-dimensional projection of the Poincaré sections (a) y versus x and (b) x versus t for $\beta = 2.200$ (hyperplane: $\dot{x} = 0$ and $x > 0$).

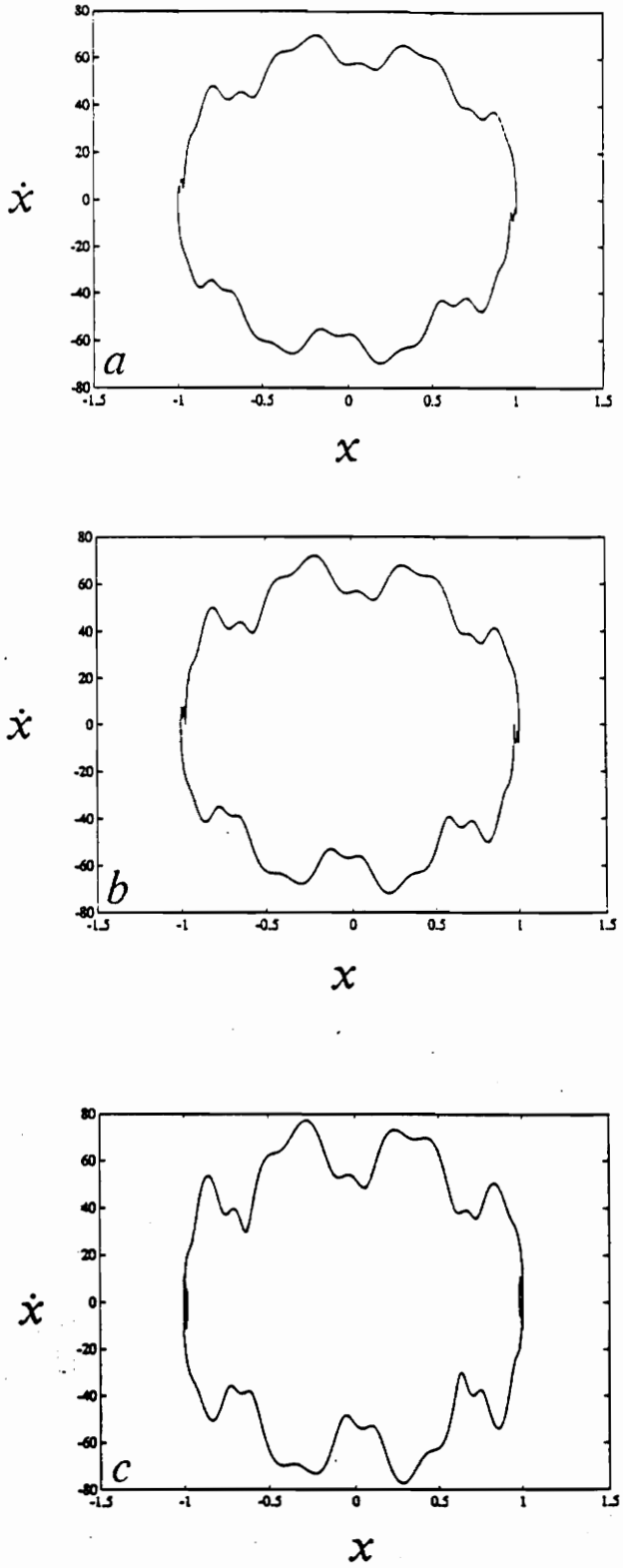

Figure 23 A two-dimensional projection of the phase portrait on the $\dot{x}$-x plane for (a) $\beta = 1.300$; (b) $\beta = 1.600$; and (c) $\beta = 1.750$

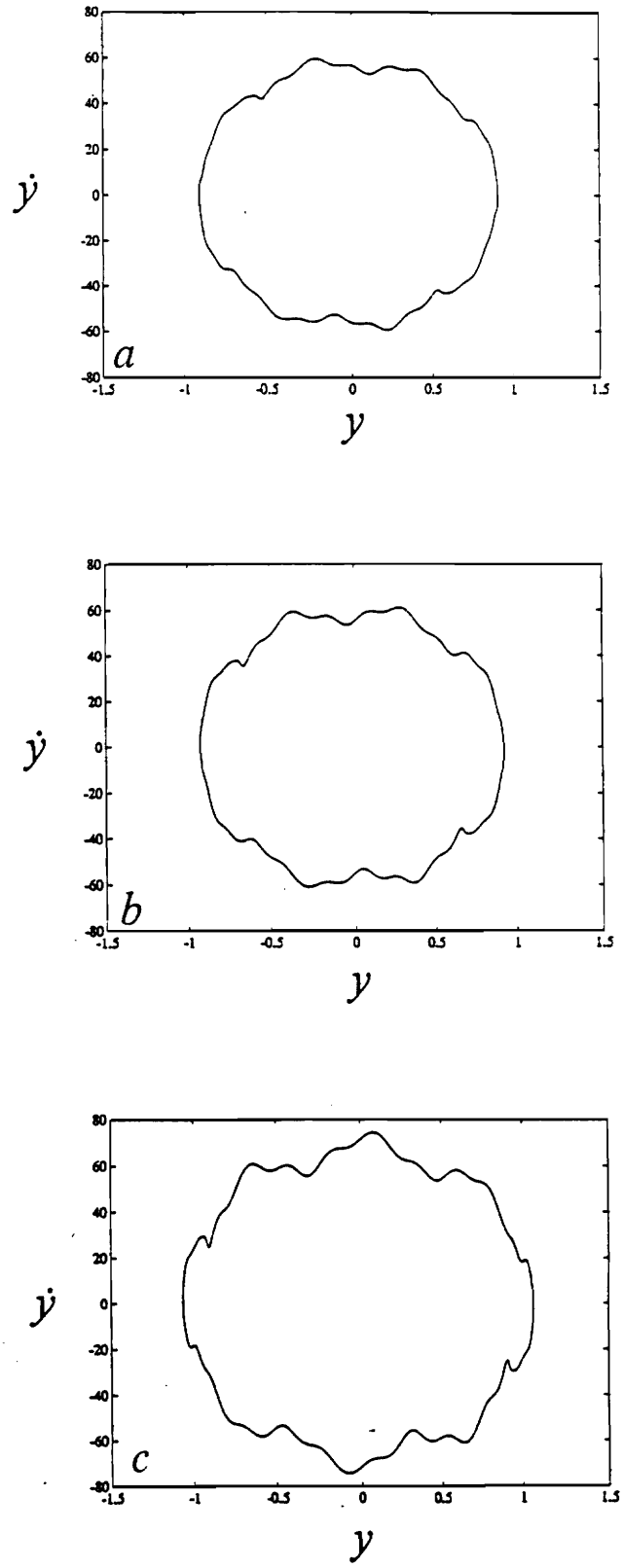

Figure 24 A two-dimensional projection of the phase portrait on the $\dot{y}$-y plane for (a) $\beta = 1.300$; (b) $\beta = 1.600$; and (c) $\beta = 1.750$

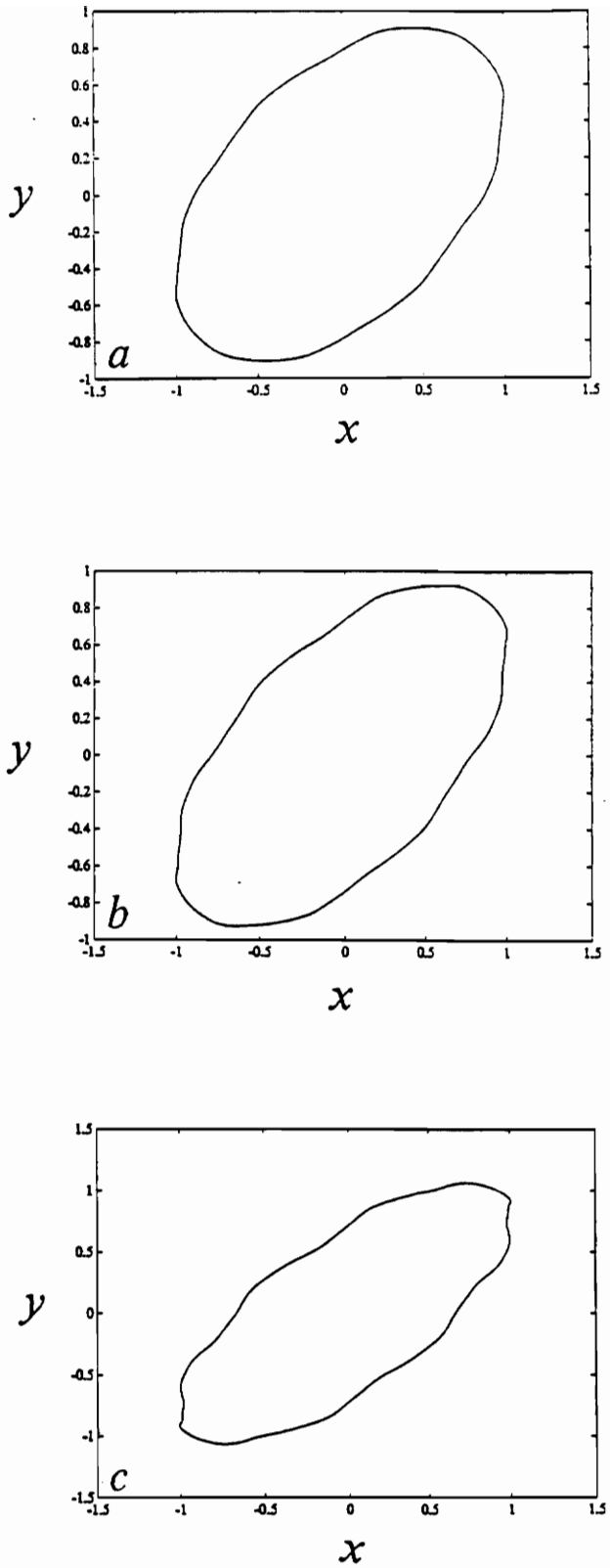

Figure 25 A two-dimensional projection of the phase portrait on the y-x plane for (a) $\beta = 1.300$; (b) $\beta = 1.600$; and (c) $\beta = 1.750$

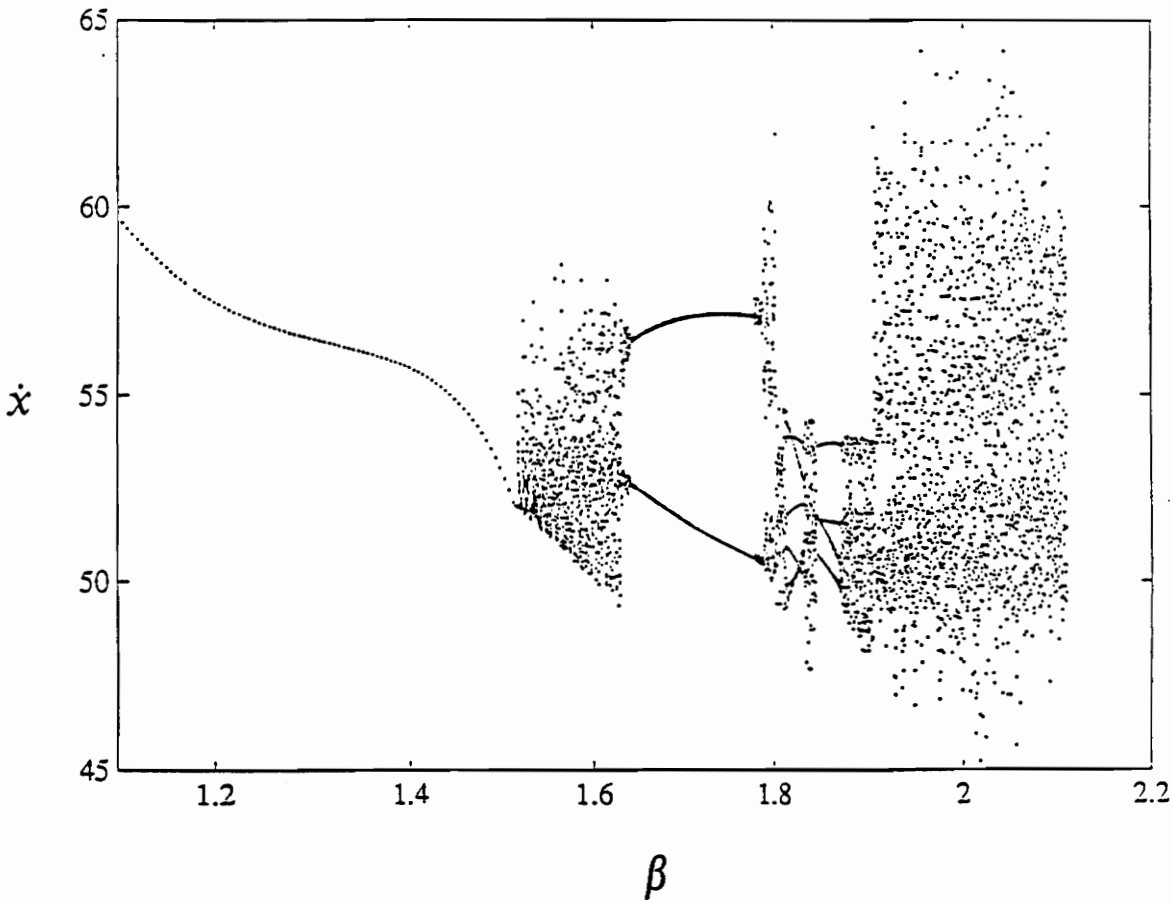

Figure 26 Bifurcation diagram showing the variation of $\dot{x}$ with β (hyperplane: $\dot{x} > 0$ and $x = 0$).

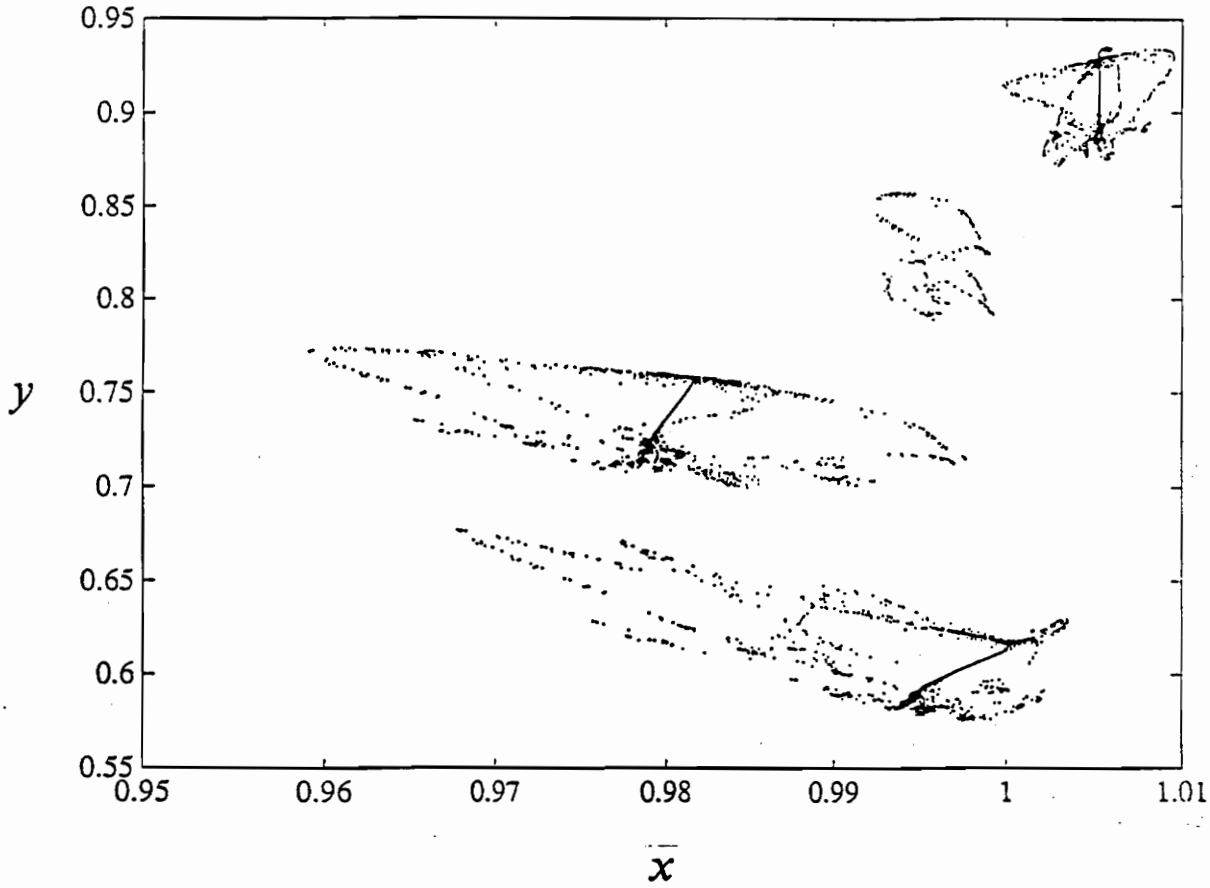

Figure 27 Poincaré section for $\beta = 1.516$ (hyperplane: $\dot{x} = 0$ and $x > 0$).

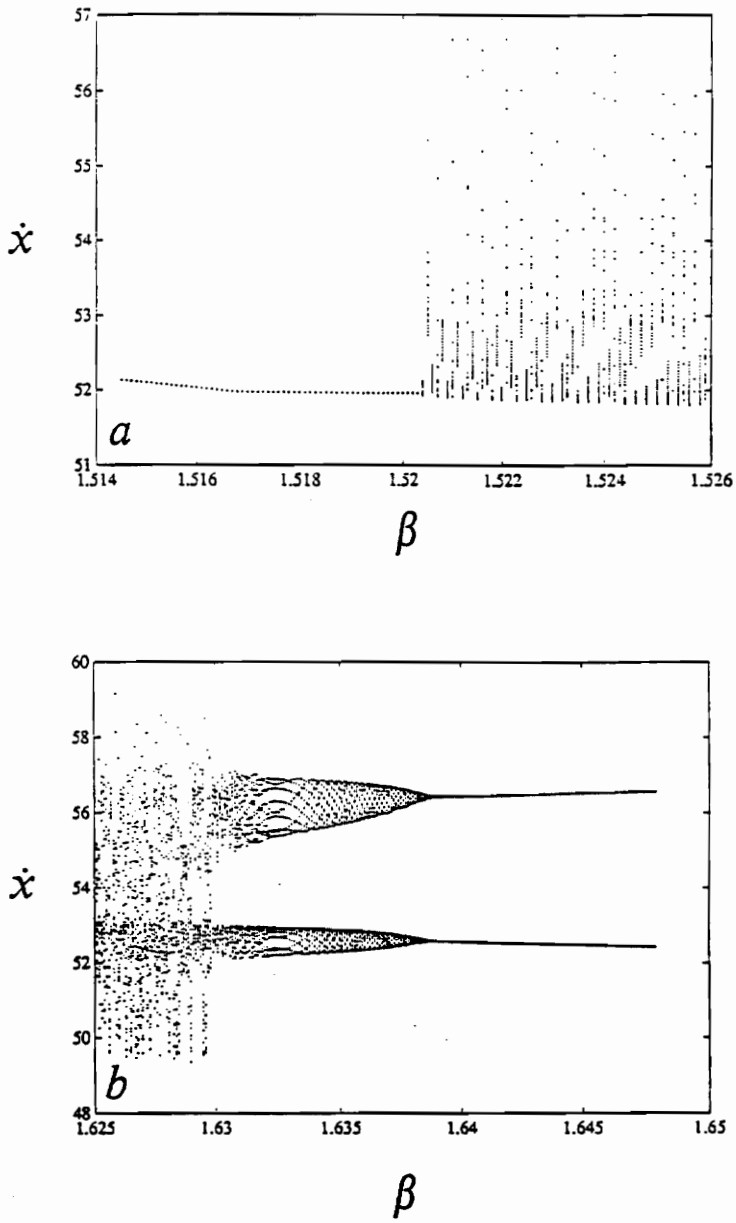

Figure 28 Enlarged bifurcation diagram near (a) $\beta = 1.516$ and (b) $\beta = 1.657$ (hyperplane: $\dot{x} > 0$ and $x = 0$).

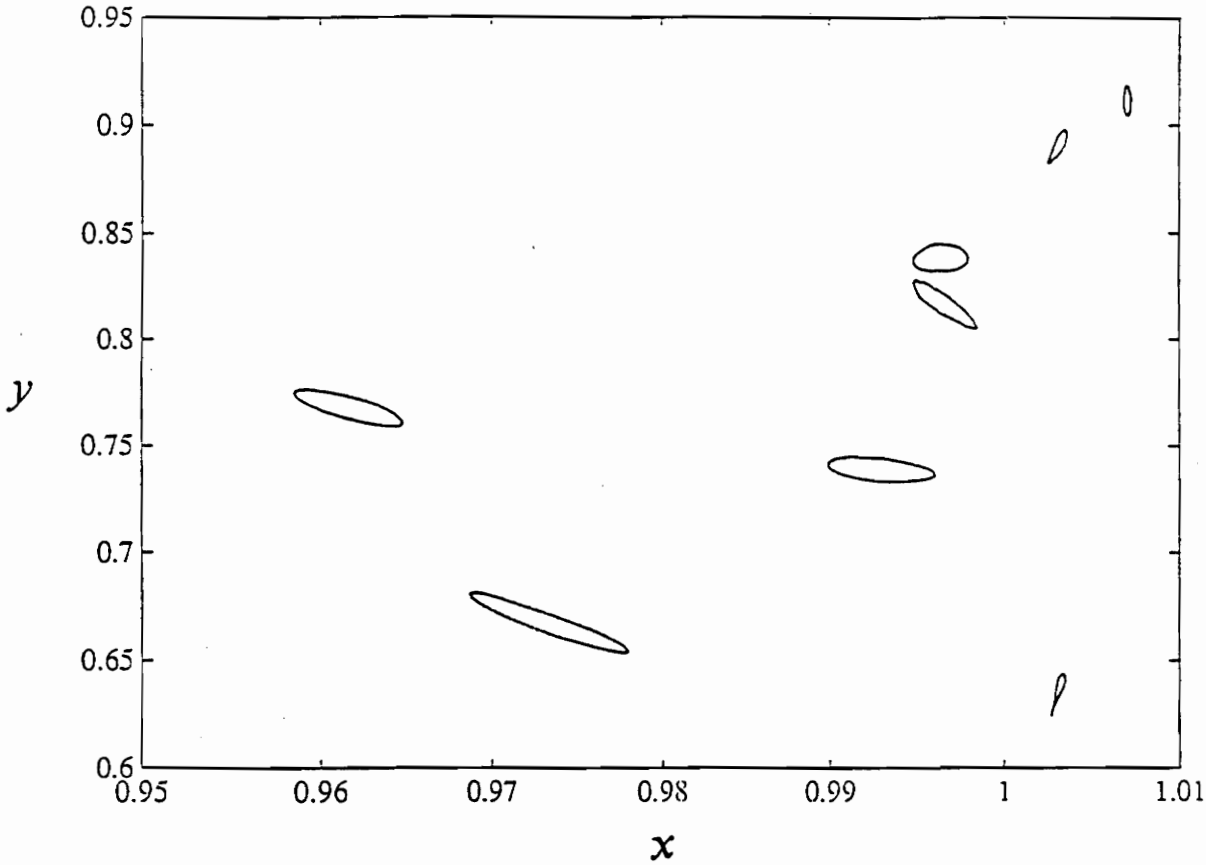

Figure 29 Poincaré section for $\beta = 1.633$ (hyperplane: $\dot{x} = 0$ and $x > 0$).

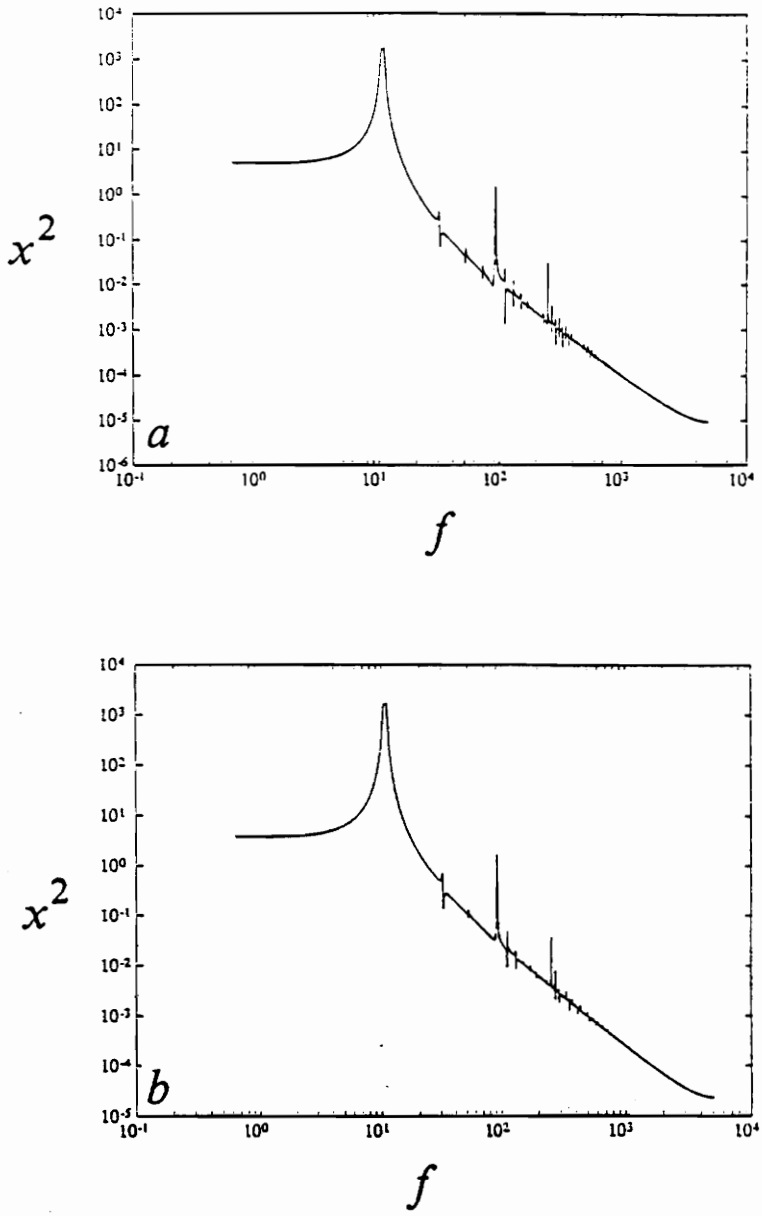

Figure 30 Power spectra of x (a) $\beta = 1.516$ and (b) $\beta = 1.526$

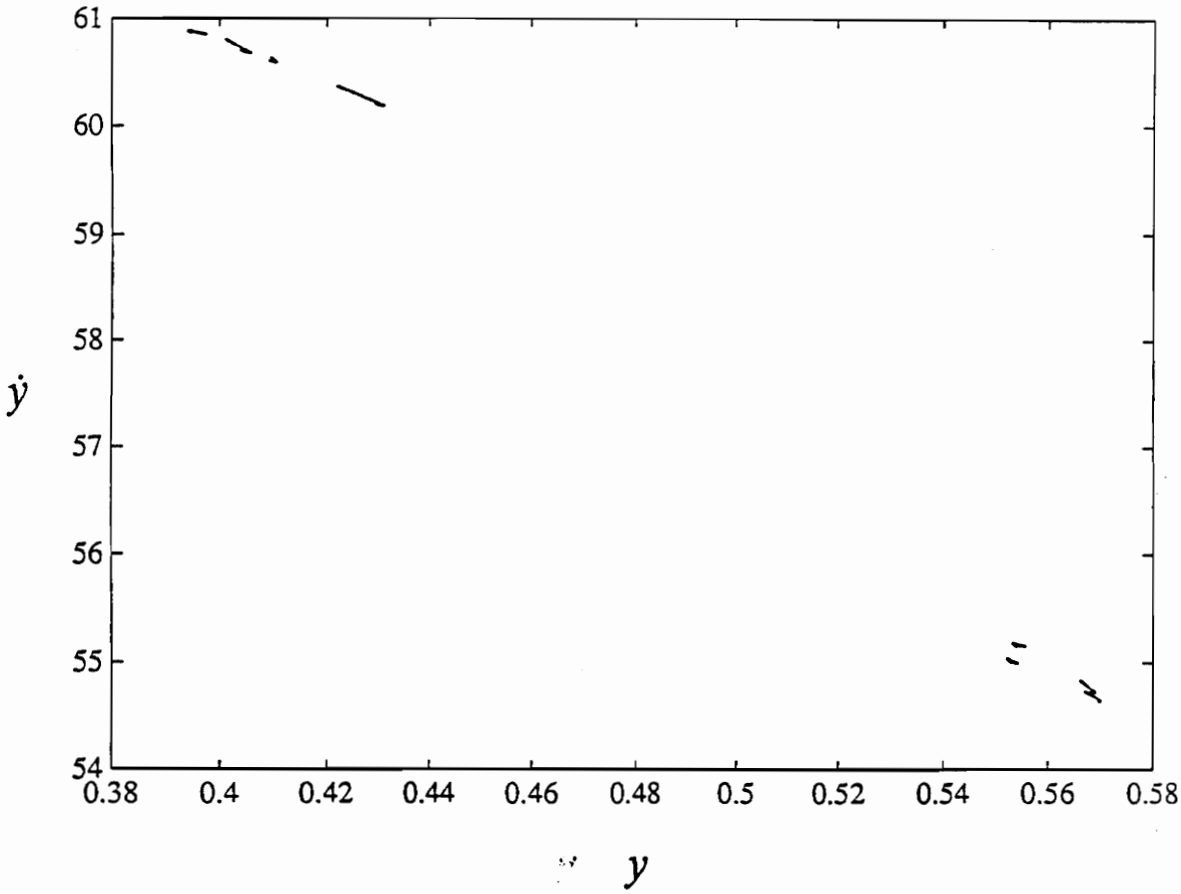

Figure 31 Poincaré section for $\beta = 1.773$ (hyperplane: $\dot{x} > 0$ and $x = 0$).

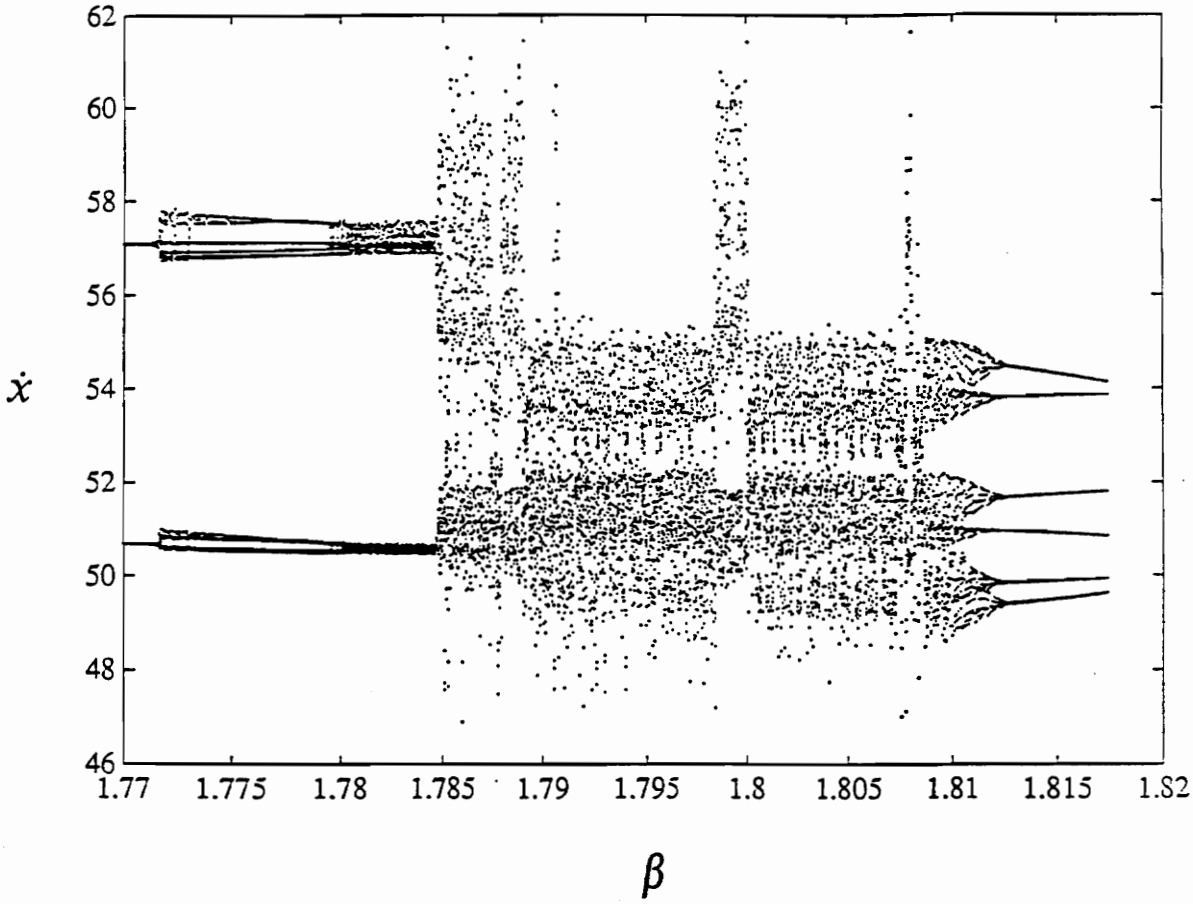

Figure 32 Enlarged bifurcation diagram (hyperplane: $\dot{x} > 0$ and $x = 0$).

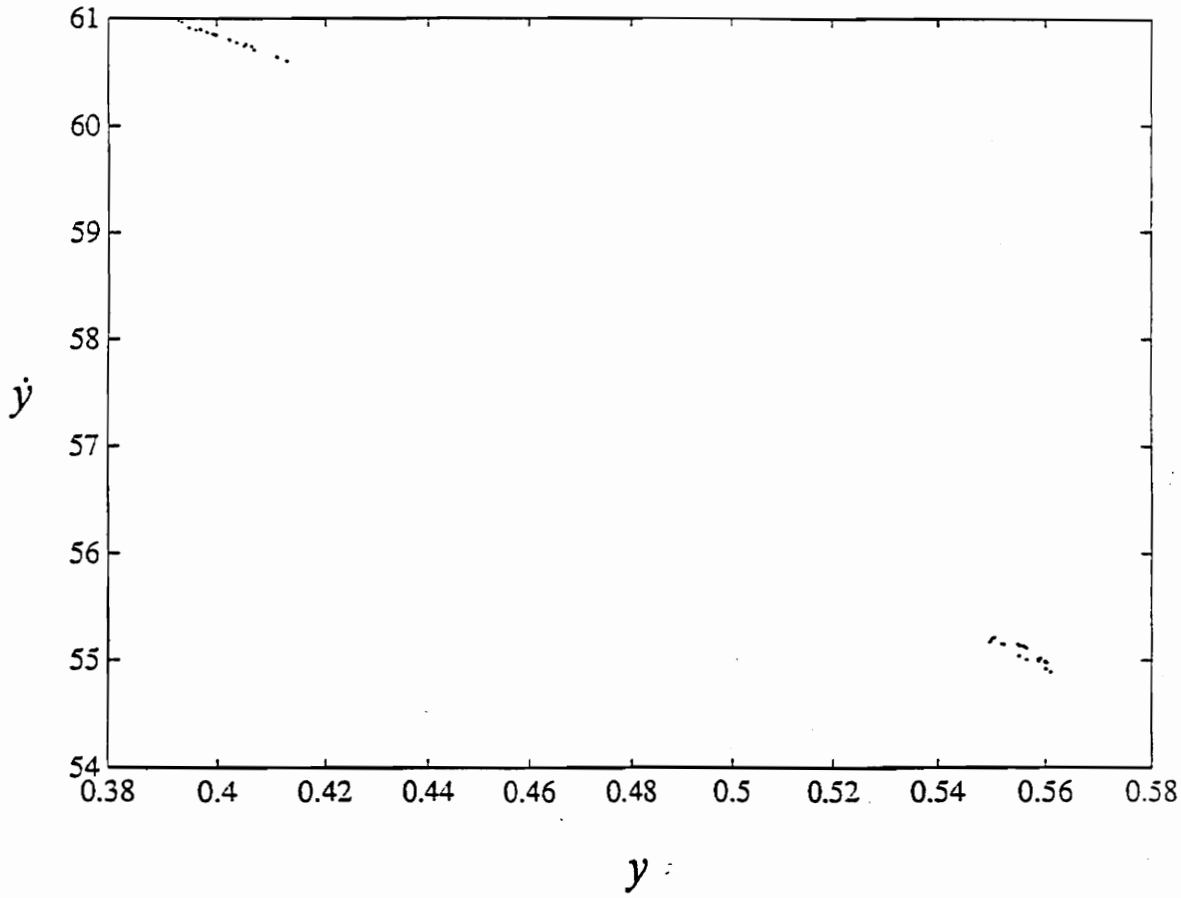

Figure 33 Poincaré section for $\beta = 1.782$ (hyperplane: $\dot{x} > 0$ and $x = 0$).

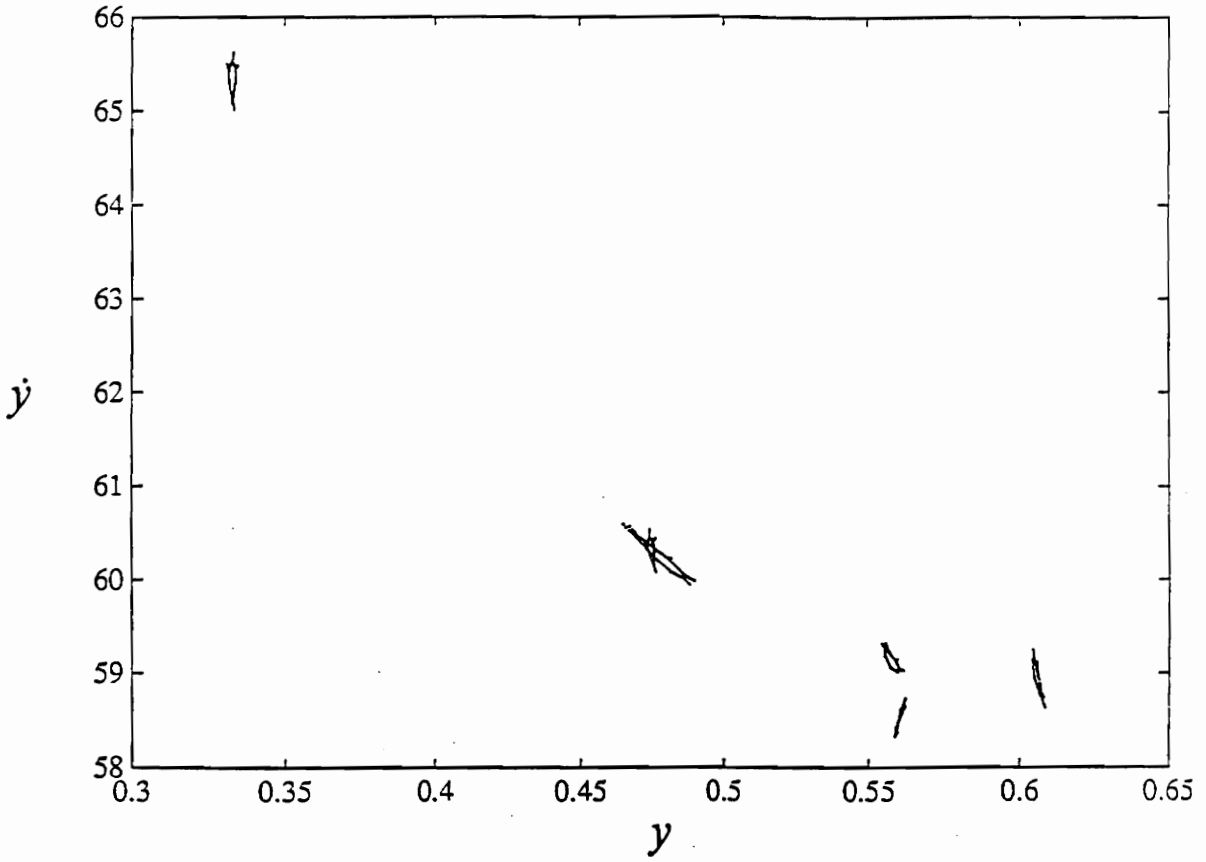

Figure 34 Poincaré section for $\beta = 1.811$ (hyperplane: $\dot{x} > 0$ and $x = 0$).

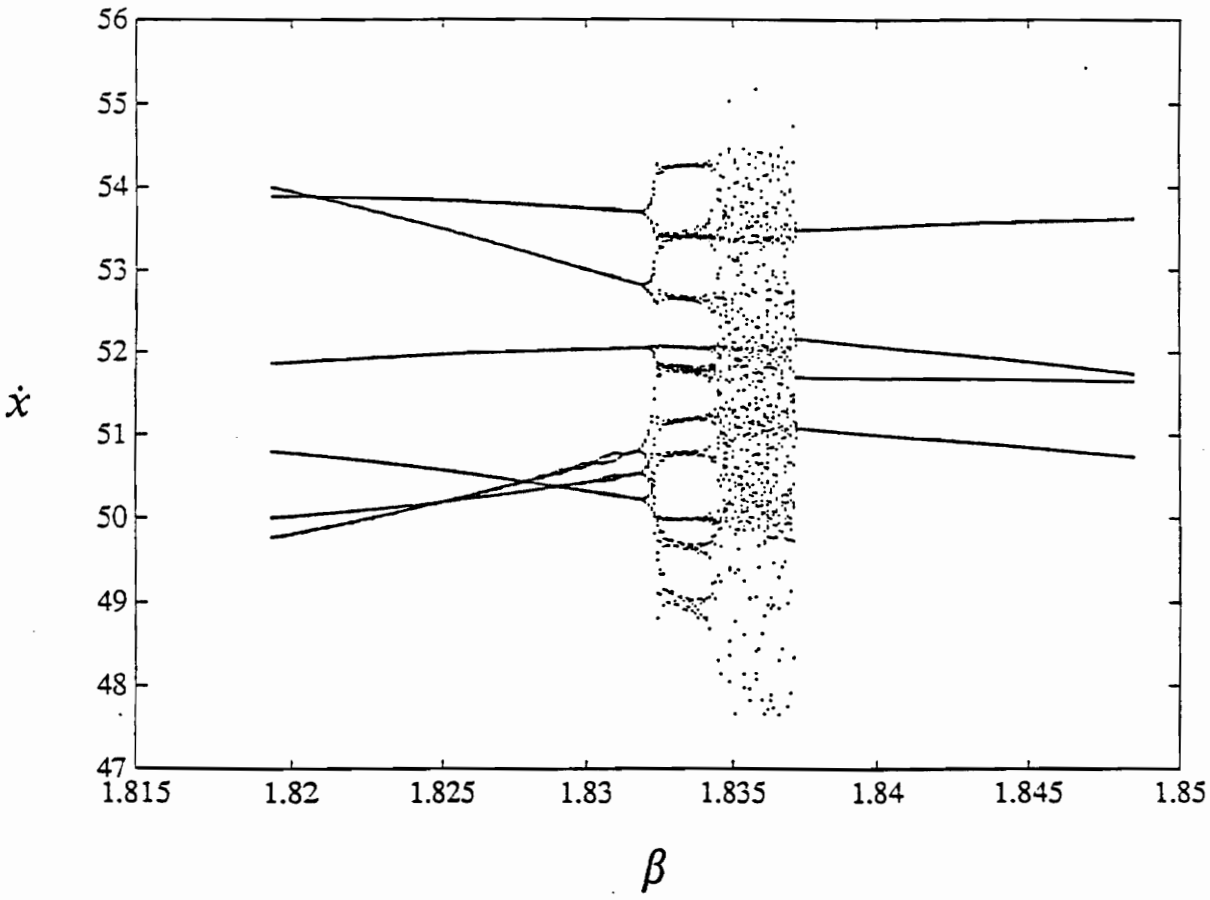

Figure 35 Enlarged bifurcation diagram (hyperplane: $\dot{x} > 0$ and $x = 0$).

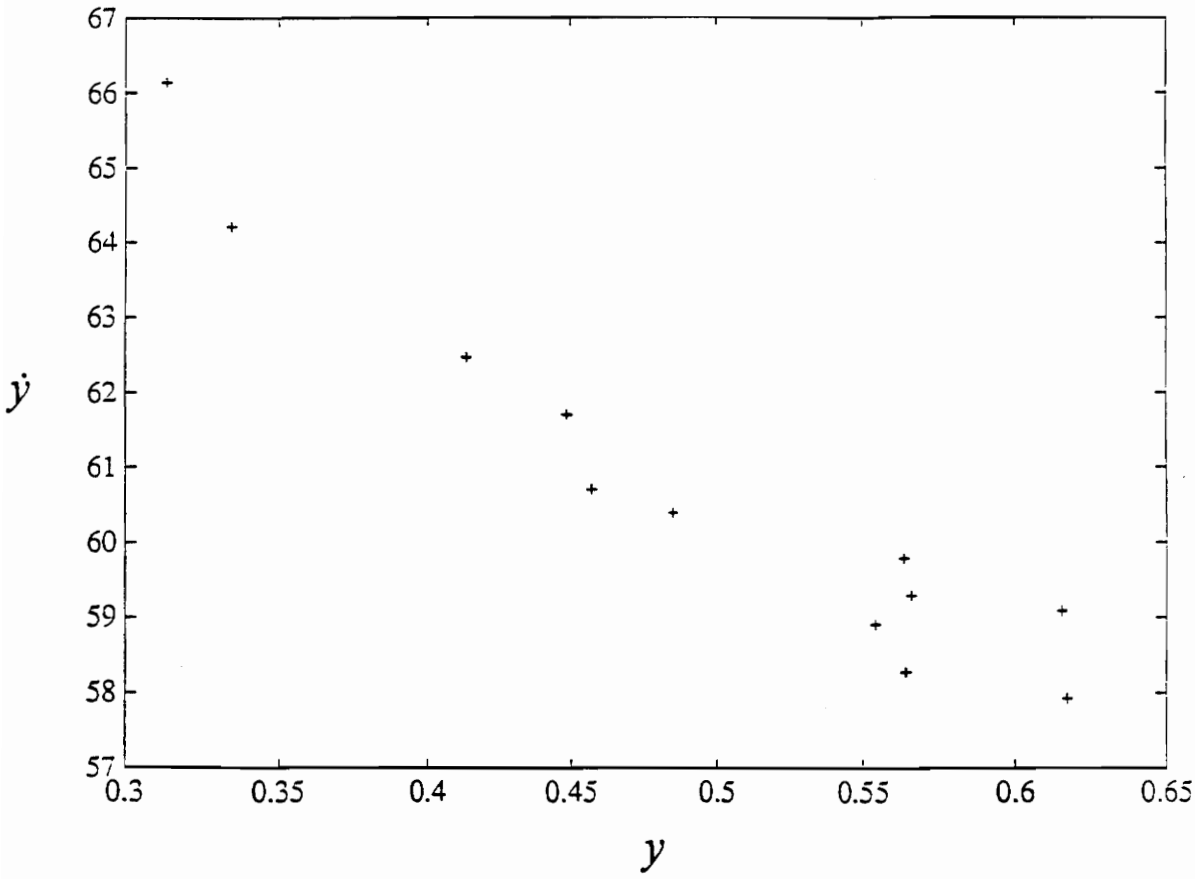

Figure 36 Poincaré section for $\beta = 1.833$ (hyperplane: $\dot{x} > 0$ and $x = 0$).

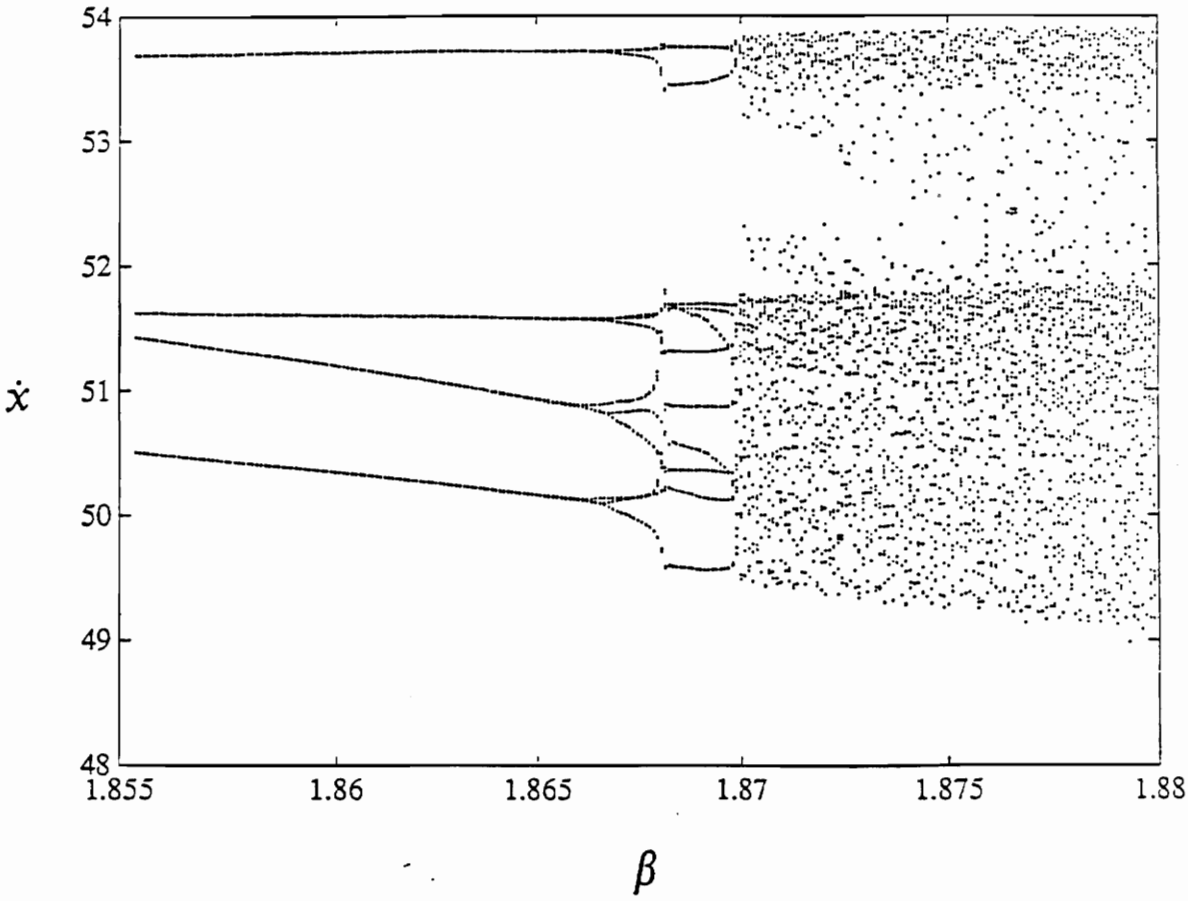

Figure 37 Enlarged bifurcation diagram (hyperplane: $\dot{x} > 0$ and $x = 0$).

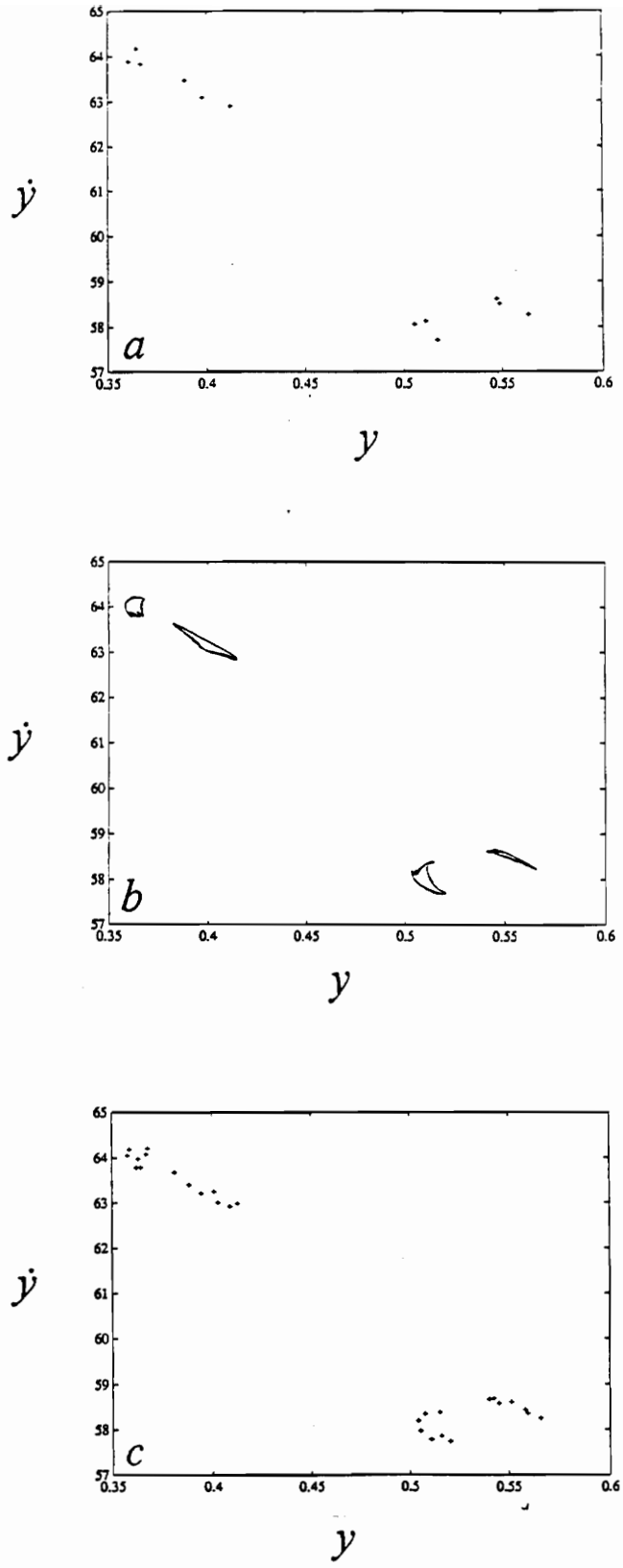

Figure 38 Poincaré section for (a) $\beta = 1.869$; (b) $\beta = 1.870$; and (c) $\beta = 1.871$ (hyperplane: $\dot{x} > 0$ and $x = 0$).

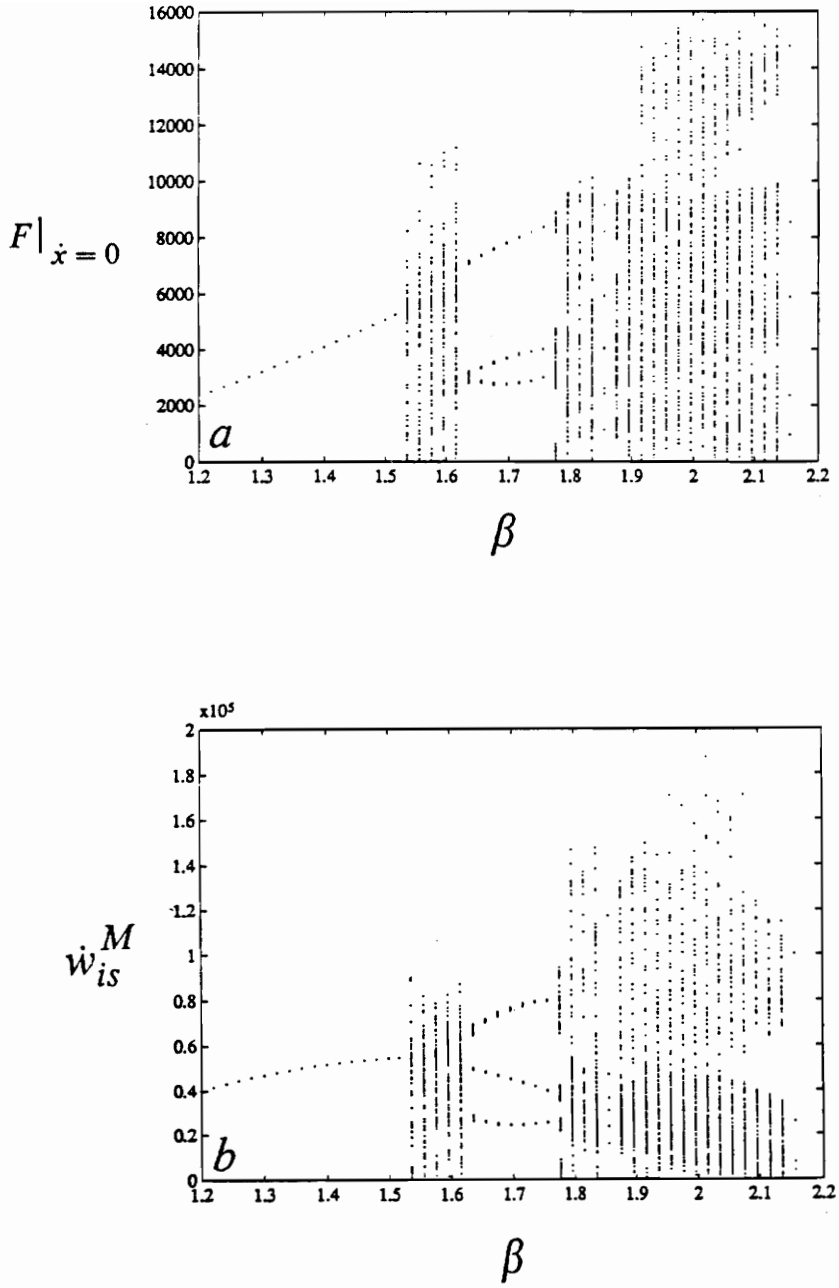

Figure 39 Instantaneous impact force rates (a) and (b) instantaneous wear work rates at maximum penetration for the dimensionless gap $g = 1.0$.

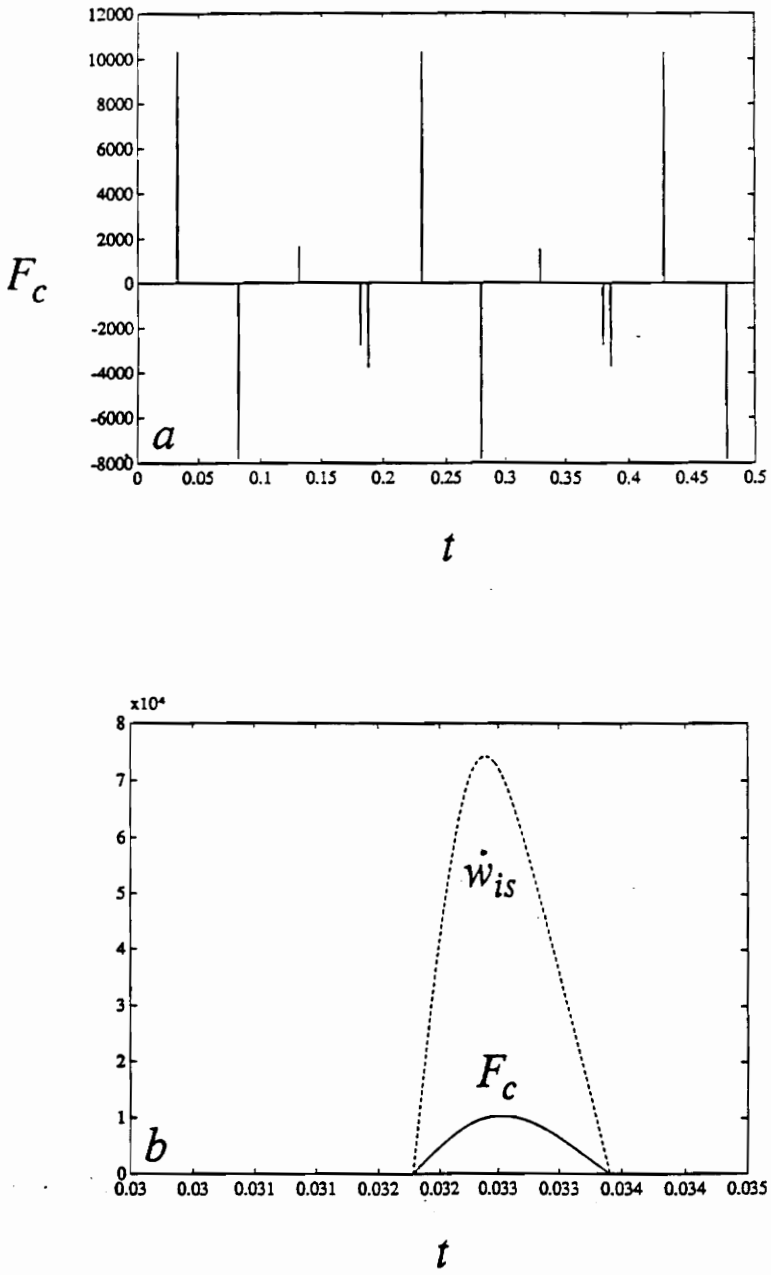

Figure 40 Variation of impact forces for $\beta = 1.700$ (a) and (b) detail of F (solid line) and $\dot{w}_{is}$ (dashed line) for $\beta = 1.700$ for dimensionless gap $g = 1.0$.

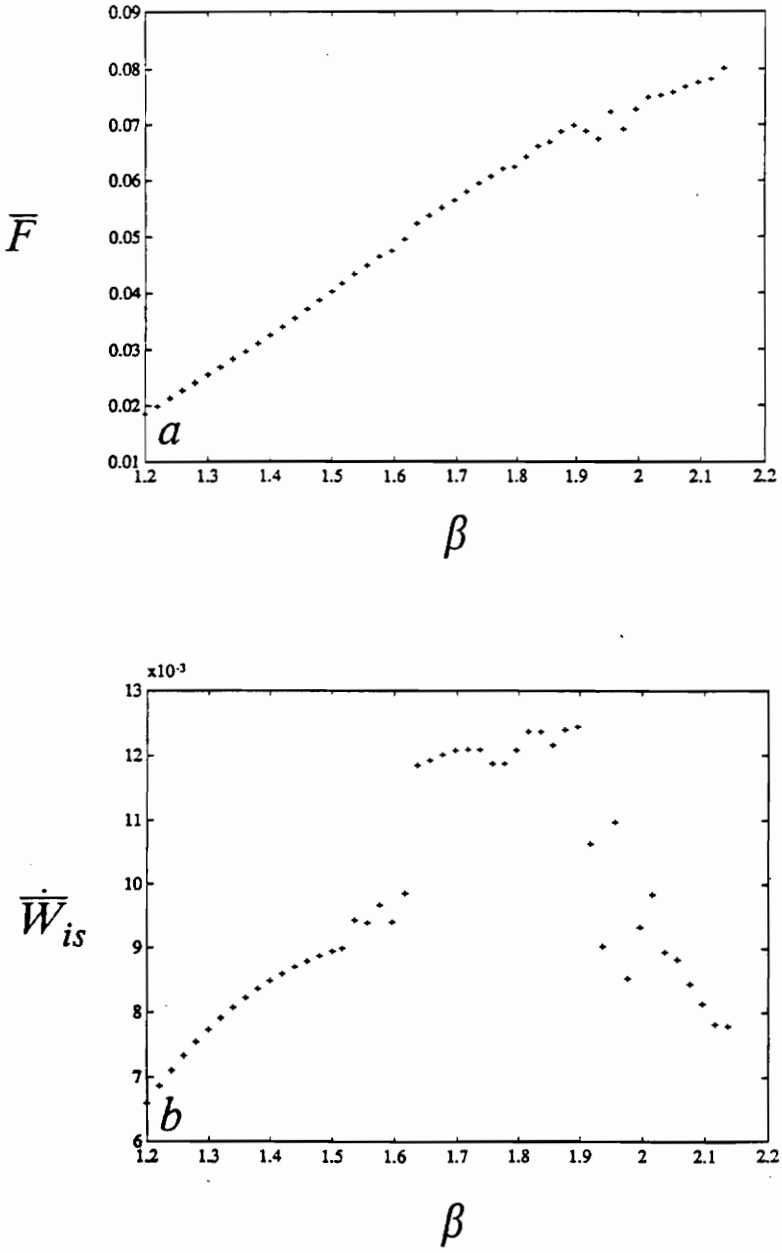

Figure 41 Variation of the mean wear work rates (a) and (b) impact forces obtained using the bidirectional model, for $g = 0.5mm$.

Vita

The author, Marc-Gabriel Yana, was born in France, July 2, 1966. He obtained a Bachelor Degree in Mechanical Engineering from Ecole National Superieurs d'Arts et Metiers in 1990. He joined Framatome Inc. in the Department of Steam Generators where he worked for one year. In 1991, he joined Virginia Polytechnic Institute and State University and will obtain a Master Degree in Engineering Science and Mechanic in 1993. He will resume work at Framatome.